



**NTNU – Trondheim**  
Norwegian University of  
Science and Technology

# Vortex Induced Vibrations of Slender Catenary Structures

**Ingrid Kornberg Simensen**

Civil and Environmental Engineering

Submission date: June 2015

Supervisor: Raed Khalil Lubbad, BAT

Norwegian University of Science and Technology  
Department of Civil and Transport Engineering





|  |   |   |              |
|--|---|---|--------------|
| Report Title: Vortex Induced Vibrations of Slender Catenary Structures | Date: 10.06.15                          |   |              |
|  | Number of pages (incl. appendices): 168 |   |              |
|  | Master Thesis                           | X | Project Work |
| Name: Ingrid Kornberg Simensen   |   |   |              |
| Professor in charge/supervisor: Raed Khalil Lubbad                     |   |   |              |
| Other external professional contacts/supervisors:                      |   |   |              |

|   |
|---|
| <p>Abstract:</p> <p>A wide range of offshore science and engineering applications utilize slender catenary-shaped structural elements in their design. These applications include moorings and steel catenary riser designs. The susceptibility of these slender catenary-shapes to vortex-induced vibrations remains the subject of theoretical, numerical and experimental studies.</p> <p>This thesis studies the measured responses from the 2001 MARINTEK experiment with the purpose of trying to understand the relation between analytical models, numerical models, and experimental measurements.</p> <p>The time domain decomposition (TDD) method is implemented in a Matlab program, considering three velocity cases of cross-flow displacements in the catenary plane. The results show that in each of the cases, one of the frequencies has a higher degree of contribution than other frequencies. However, multiple frequencies are present throughout the measurements. Also, the frequencies corresponding to each mode varies. According to the MAC-criterion, the obtained mode shapes have a high degree of correlation with the numerically calculated mode shapes.</p> <p>For verification of the TDD results, the poly-reference least squares complex frequency method and the data- and covariance-driven stochastic subspace methods of operational modal analysis (OMA) are used for studying the data in the commercial Matlab toolbox MACEC. As for the TDD method, the mode shape estimates have high MAC-values, and the corresponding natural frequencies vary. The damping estimates show a great amount of scatter. Also, there is a varying degree of certainty in the results according to result processing guidelines.</p> <p>The effect of accelerometer masses and first order added mass effects are studied using a numerical model in Matlab. The effects of the masses are concluded to be negligible.</p> <p>A comparison between the operational modal OMA obtained eigenfrequencies and the corresponding numerically calculated modes show a great amount of agreement in how the natural frequencies increase with mode number. However, for this case study, the analytical and numerical calculations appear to underestimate magnitudes of the frequencies. Also, there is an indication that the frequencies corresponding to each mode shape vary, possibly resulting from higher order added mass effects.</p> |
|---|

Keywords:

|                              |
|------------------------------|
| 1. Steel Catenary Risers     |
| 2. Vortex Induced Vibrations |
| 3. System Identification     |





---

## Summary

A wide range of offshore science and engineering applications utilize slender catenary-shaped structural elements in their design. These applications include moorings and steel catenary riser designs. The susceptibility of these slender catenary-shapes to vortex-induced vibrations remains the subject of theoretical, numerical and experimental studies.

This thesis studies measured responses from the 2001 MARINTEK experiment with the purpose of trying to understand the relation between analytical models, numerical models, and experimental measurements.

The time domain decomposition (TDD) method is implemented in a Matlab program, considering three velocity cases of cross-flow displacements in the catenary plane. The results show that in each of the cases, one of the frequencies has a higher degree of contribution than other frequencies. However, multiple frequencies are present throughout the measurements. Also, the frequencies corresponding to each mode varies. According to the MAC-criterion, the obtained mode shapes have a relatively high degree of correlation with the numerically calculated mode shapes.

For verification of the TDD results, the poly-reference least squares complex frequency method and the data- and covariance-driven stochastic subspace methods of operational modal analysis (OMA) are used for studying the data in the commercial Matlab toolbox MACEC. As for the TDD method, the mode shape estimates have high modal assurance criterion (MAC) values, and the corresponding natural frequencies vary. The damping estimates show a great amount of scatter. Also, there is a varying degree of certainty in the results, as some modal frequencies are more difficult to obtain due to signal noise or other sources of error.

Continuing, the effect of accelerometer masses and first order added mass effects are studied using a numerical model in Matlab. There are limitations in the results because of the simplification of the added masses. However, based on the minimal changes in mode shapes, and the eigenvalues changing opposite to what they should in comparison with experimental data, the effects of the masses are concluded to be negligible. This conclusion coincides with original assumptions made for the analytical and numerical models.

A comparison between the OMA obtained eigenfrequencies and the corresponding numerically calculated modes show that there is a great amount of agreement in how the natural frequencies increase with mode number. However, for this case study, the analytical and numerical

---

---

calculations appear to underestimate magnitudes of the frequencies. Also, there is an indication that the frequencies corresponding to each mode shape vary resulting from higher order added mass effects, which are not considered in the numerical or analytical methods.

---

## Sammendrag

Konstruksjoner bestående av elementer som danner en hengende form mellom to innfestningspunkter blir anvendt i mange offshore installasjoner og andre tekniske innretninger. Blant bruksområdene finnes forankringer av flytende konstruksjoner og hengende stigerør i stål. Disse strukturene er utsatt for virvelinduserte vibrasjoner, som fortsatt er et felt som undersøkes både teoretisk, numerisk og med eksperimenter.

Analysene utført i denne hovedoppgaven er basert på eksperimentelle resultater fra et prosjekt som ble utført ved MARINTEK i 2001. Hensikten er å få en bedre forståelse for sammenhengen mellom de analytiske modellene, de numeriske modellene og observasjoner gjort under forsøkene.

En dekomponeringsmetode for tidsdomenet (TDD) er brukt til systemidentifikasjon av måledataen, og er implementert i et Matlab program. Her er tre hastighetstilfeller fra forsøket er brukt, alle med målt bevegelse i konstruksjonsplanet. Resultatene av studiet viser at for alle hastighetstilfellene vibrerer strukturen med én hovedfrekvens. Det finnes likevel flere vibrasjonsfrekvenser i måledataene til enhver tid. I tillegg er det observert at enkelte frekvenser kan endre modeform avhengig av strømningshastigheten strukturen er utsatt for. Mange av modeformene som er funnet ved bruk av TDD metoden har ifølge MAC kriteriet en høy grad av korrelasjon med modeformene beregnet med elementmetoden.

For å kontrollere resultatene som er funnet med TDD metoden, er en minste kvadraters kompleks frekvens metode (p-LSCF), en data drevet stokastiske Subspace-metode (DD-SSI) og en kovarians drevet stokastiske Subspace-metode (Cov-SSI) også brukt i analysene av måledataene i Matlab verktøyet MACEC. Her har også de estimerte modeformene god overenstemmelse med modeformene beregnet med elementmetoden ifølge MAC kriteriet, mens egenfrekvensene også her har en tendens til å endre modeformene de tilhører. Det er stor spredning i dempningsestimaterne. Støy i signalet gjør at flere av de beregnede egenfrekvensene og modeformene har stor usikkerhet.

Første ordens innvirkning av akselerometrenes masse og tilleggs masse er undersøkt i en numerisk modell i Matlab. Resultatene fra denne undersøkelsen er kun anvendelige for enkle sammenligninger ettersom tilleggs massens innflytelse er meget forenklet. De beregnede modeformene viser liten forandring sammenlignet med modeformene som er beregnet uten å ta hensyn til akselerometermassene. Graden av endring øker med økende modenummer. Det

---

viser seg at når akselerometermassene er inkludert i elementmetodeberegningene øker ikke egenfrekvensene like mye med modetall som det egenfrekvensene som er beregnet ved systemidentifikasjon av måledataen gjør.

En sammenligning mellom egenfrekvensene som er funnet ved bruk av TDD, p-LSCF, DD-SSI og Cov-SSI metodene og de som er beregnet ved bruk av elementmetoden uten akselerometrenes masser viser at det er stor grad av overenstemmelse når det gjelder hvordan egenfrekvensene øker med modenummer. Det viser seg likevel at de egenfrekvensene beregnet med elementmetoden er noe lavere enn frekvensene som er beregnet ved systemidentifikasjon, spesielt i de høyeste modetallene. I tillegg finnes det indikasjoner på at frekvensene som korresponderer til hver mode varierer, og dette kan være et resultat av høyere ordens effekter av tilleggsmassene, som ikke er tatt hensyn til i numeriske eller analytiske metoder presentert i denne oppgaven.

---

# Acknowledgements


This Master's thesis was written for the Marine Civil Engineering Group at the Department of Civil and Transport Engineering, NTNU. It represents the full work load of the last spring semester of a five-year Master program in Civil and Environmental Engineering.

I would like to thank my supervisor Associate Professor Raed Khalil Lubbad for all his advice, support and valuable discussions. His instructive supervision and extensive knowledge has been a great motivation and inspiration throughout my work.

Many thanks to Professor John Niedzwecki for his interest and input in my project, and for his co-operation in providing the data used for the thesis case study. I am also thankful for the input and guidance of PhD Candidate Torodd Skjerve Nord, and for Associate Professor Ole Øiseth giving me access to the commercial software MACEC. I would also like to thank Professor Carl Martin Larsen for providing a very useful private note on Vortex Induced Vibrations, which was of great help in providing a fundamental understanding of the topic.

Finally, I would like to thank all of my friends and family for their unconditional love and support throughout my years as a student at NTNU. A special thanks to Ruth Hetland for all fruitful "work meals" and idea exchanges, and Gørild Eide for the clarity and peace of mind I got from all of our walks.

Trondheim, 2015

A handwritten signature in black ink that reads "Ingrid Simonsen". The signature is written in a cursive style with a light grey rectangular background behind it.



---

# Table of Contents

|   |    |
|---|----|
| <b>Chapter 1 Introduction</b> .....                                       | 1  |
| 1.1 Background .....  | 1  |
| 1.2 Motivation and scope of work.....                                     | 3  |
| 1.3 Structure of thesis.....  | 5  |
| 1.4 Readership.....   | 6  |
| <b>Chapter 2 Theory of Vortex Induced Vibrations</b> .....                | 7  |
| 2.1 The process of vortex shedding.....                                   | 7  |
| 2.1.1 Reynolds Number .....   | 8  |
| 2.1.2 Strouhal Number.....  | 9  |
| 2.1.3 Vortices.....   | 10 |
| 2.1.4 In-line and cross-flow motions .....                                | 11 |
| 2.1.5 Reduced Velocity .....  | 11 |
| 2.1.6 Hydrodynamic Loading .....  | 12 |
| 2.1.7 Vortex Suppression.....   | 12 |
| 2.1.8 VIV Analysis .....  | 13 |
| <b>Chapter 3 Structural analysis of slender catenary structures</b> ..... | 15 |
| 3.1 The equation of motion and solution methods.....                      | 15 |
| 3.1.1 Modal analysis using damped modes .....                             | 17 |
| 3.1.2 Calculating Modal Parameters with Damping.....                      | 18 |
| 3.1.3 Modal Analysis in the Frequency Domain .....                        | 21 |
| 3.2 Static analysis of slender catenary structures .....                  | 22 |
| 3.2.1 Inextensible cable .....  | 23 |
| 3.2.2 Extensible cable.....   | 24 |
| 3.2.3 Beam formulations of the catenary shape.....                        | 26 |
| 3.3 Eigenvalue analysis of slender catenary structures .....              | 28 |

---

|   |           |
|---|-----------|
| 3.3.1 Analytical Methods.....                                       | 29        |
| 3.3.2 Finite Element Solutions .....                                | 31        |
| <b>Chapter 4 System Identification Methods .....</b>                | <b>35</b> |
| 4.1 Random Processes.....   | 37        |
| 4.1.1 Power Spectral Density .....                                  | 38        |
| 4.1.2 Convolution .....   | 39        |
| 4.1.3 Covariance .....  | 39        |
| 4.1.4 Correlation .....   | 40        |
| 4.1.5 Application of the Fundamental Theories .....                 | 41        |
| 4.2 Singular Value Decomposition .....                              | 42        |
| 4.3 Operational Modal Analysis Techniques .....                     | 44        |
| 4.3.1 Time Domain Decomposition Method .....                        | 44        |
| 4.3.2 The Macec Methods .....                                       | 47        |
| 4.3.3 Processing of Mode-Shape and Natural Frequency Estimates..... | 52        |
| <b>Chapter 5 Case Study .....</b>                                   | <b>55</b> |
| 5.1 Description of the Experiment .....                             | 55        |
| 5.1.1 The Test Facility .....                                       | 55        |
| 5.1.2 The Experimental Setup .....                                  | 56        |
| 5.1.3 The Catenary Riser Model.....                                 | 57        |
| 5.1.4 The Coordinate Systems.....                                   | 60        |
| 5.1.5 The Test Program .....  | 61        |
| 5.2 Experimental results and discussion .....                       | 61        |
| 5.2.1 Case Study .....  | 64        |
| 5.3 Application of the Time Domain Decomposition method.....        | 66        |
| 5.3.1 Results .....   | 67        |
| 5.4 OMA investigations using MACEC .....                            | 72        |
| 5.4.1 Results .....   | 73        |

---



---

|   |            |
|---|------------|
| 5.5 Numerical investigations of the accelerometers effects on the solution of the eigenvalue problem..... | 82         |
| 5.5.1 DNV DeepC and Riflex for Static Analysis .....  | 82         |
| 5.5.2 Natural Frequency and Mode-Shape Investigation Using Matlab .....                                   | 84         |
| 5.5.3 Results .....   | 85         |
| 5.6 Discussions.....  | 88         |
| 5.6.1 System identification and FEM comparison .....  | 88         |
| 5.6.2 Accelerometer added mass effects .....  | 91         |
| <b>Chapter 6 Concluding remarks .....</b>   | <b>93</b>  |
| <b>Chapter 7 Recommendations for future work .....</b>  | <b>95</b>  |
| <b>Bibliography .....</b>   | <b>97</b>  |
| <b>Appendix A Task Description.....</b>   | <b>101</b> |
| <b>Appendix B Step-by-step MACEC procedure .....</b>  | <b>103</b> |
| <b>Appendix C The TDD Method Results .....</b>  | <b>107</b> |
| C.1 0.12 m/s .....  | 107        |
| C.2 0.24 m/s .....  | 110        |
| C.3 0.34 m/s .....  | 114        |
| <b>Appendix D The MACEC Method Results .....</b>  | <b>117</b> |
| D.1 Covariance driven SSI.....  | 117        |
| D.1.1 0.12 m/s.....   | 117        |
| D.1.2 0.24 m/s.....   | 120        |
| D.1.3 0.34 m/s.....   | 122        |
| D.2 Data-driven SSI.....  | 124        |
| D.2.1 0.12 m/s.....   | 124        |
| D.2.2 0.24 m/s.....   | 127        |
| D.2.3 0.34 m/s.....   | 130        |
| D.3 p-LSCF.....   | 134        |

---

---

|   |            |
|---|------------|
| D.3.1 0.12 m/s.....                           | 134        |
| D.3.2 0.24 m/s.....                           | 137        |
| D.3.3 0.34 m/s.....                           | 140        |
| <b>Appendix E List of Matlab Scripts.....</b> | <b>145</b> |

---

# List of Figures

|   |    |
|---|----|
| Figure 1.1: Example of a catenary shaped structural element .....   | 1  |
| Figure 1.2: (a) Mode shape obtained from TDD of experimental data excited at 1.20 Hz. (b) Mode shape obtained from analytical and numerical solutions corresponding to an eigenfrequency of 1.05-1.08 Hz..... | 3  |
| Figure 2.1: Cross-section subject to fluid flow and fluid separation .....  | 8  |
| Figure 2.2 Vortex patterns as a function of Reynolds number (Blevins 1994) .....  | 9  |
| Figure 2.3: Example trajectory of the mid-point of a structure subject to VIV.....  | 11 |
| Figure 2.4: Suppression devices.(a) and (h) are surface protrusions. (b) and (c) work like shrouds. (d)-(g) are forms of wake devices.(Blevins 1994).....   | 13 |
| Figure 2.5: Space sharing vs time sharing models of VIV analysis .....  | 14 |
| Figure 3.1: A multi-degree of freedom system.....   | 16 |
| Figure 3.2: Conceptual interpretation of Rayleigh damping, as interpreted from (Crowe 2009) .....   | 18 |
| Figure 3.3: The catenary plane, and the catenary cross-section .....  | 23 |
| Figure 3.4: Catenary profiles calculated by inextensible and extensible theory.....   | 26 |
| Figure 3.5: Catenary tension distribution calculated using extensible and inextensible cable theory .....   | 26 |
| Figure 3.6: Comparison of beam and cable formulations of the catenary profile .....   | 27 |
| Figure 3.7: Comparison of beam and cable formulations of the tension distribution .....   | 27 |
| Figure 3.8: The degrees of freedom of a catenary element.....   | 32 |
| Figure 4.1: Assumed system for OMA applications.....  | 36 |
| Figure 4.2: Sinusoid signal vs a random process signal. ....  | 37 |
| Figure 4.3: A Fourier transform of a rectangular window function .....  | 42 |
| Figure 4.4: Example PSD from a sensor of the experimental data presented in Chapter 5.....  | 44 |
| Figure 5.1: Overview of the MARINTEK test facility (Lie 2001). ....   | 56 |
| Figure 5.2: View of catenary setup from above (Lie 2001).....   | 56 |
| Figure 5.3: Vertical setup of catenary (Lie 2001).....  | 56 |
| Figure 5.4: Accelerometers with casing (Lie 2001).....  | 58 |
| Figure 5.5: Coordinate systems used for experimental work and results, modified image from (Lie, 2001).....   | 60 |
| Figure 5.6: Displacement time-series from sensor 5 at 0.12 m/s current velocity.....  | 62 |

---

|   |    |
|---|----|
| Figure 5.7: Displacement time-series from sensor 5 at 0.34 m/s current velocity.....  | 62 |
| Figure 5.8. PSD of displacements measured at accelerometer 5 in the cross-flow direction, with a 0.12 m/s flow velocity.....  | 63 |
| Figure 5.9: PSD of displacements measured at accelerometer 5 in the cross-flow direction, with a 0.34 m/s flow velocity.....  | 63 |
| Figure 5.10: Displacement envelopes of the 0.12 m/s current flow velocity. ....   | 63 |
| Figure 5.11: Displacement envelopes of the 0.34 m/s current flow velocity. ....   | 63 |
| Figure 5.12: AutoMAC comparison of the WKB mode shapes relative to the FEM method mode shapes.....  | 65 |
| Figure 5.13: Flow-chart of implemented TDD method in Matlab.....  | 66 |
| Figure 5.14: (a) The identification window of the implemented TDD codes. (b) The identification window for determining the decrement slope for damping.....   | 67 |
| Figure 5.15: AutoMAC matrix from the comparison of the 0.12 m/s data using the TDD method and the FEM solutions.....  | 68 |
| Figure 5.16: Complexity plots of (a) A very normal mode, the 4 <sup>th</sup> mode found by 0.12 m/s velocity p-LSCF. (b) A relatively complex mode, the 3 <sup>rd</sup> mode found by 0.34 m/s velocity p-LSCF..... | 73 |
| Figure 5.17: Stabilization diagram for the p-LSCF 0.12 m/s case.....  | 74 |
| Figure 5.18: Example stabilization diagram for the Cov-SSI 0.34 m/s case. ....  | 77 |
| Figure 5.19: AutoMAC matrix of the DDSSI 0.24 m/s and FEM solution.....   | 80 |
| Figure 5.20: Complexity plot of the 8th mode using the DD-SSI method and 0.34 m/s current flow. ....  | 81 |
| Figure 5.21: Static configuration using DeepC/RIFLEX.....   | 83 |
| Figure 5.22: Flow-chart of matlab script for investigation of accelerometer effects.....  | 84 |
| Figure 5.23: Static profile of accelerometer mass loaded catenary.....  | 85 |
| Figure 5.24: Tension profile of accelerometer mass loaded catenary.....   | 85 |
| Figure 5.25: Calculated eigenfrequencies of accelerometer loaded catenary.....  | 85 |
| Figure 5.26: A plot of the 3rd mode shape obtained from FEM analysis of the accelerometer loaded masses.....  | 85 |
| Figure 5.27: MAC matrix of eigenfrequencies 1-10 of mass loaded mode shapes vs original FEM mode shapes.....  | 87 |
| Figure 5.28: Experimental and FEM natural frequency results.....  | 88 |
| Figure 5.29: Modal damping estimate comparison.....   | 90 |

---

---

|  |     |
|--|-----|
| Figure 5.30: Time-series of modal participation of the 5 first identified modes usind TDD with the 0.24 m/s measurements ..... | 91  |
| Figure C 1: MAC matrix for TDD method obtained mode shapes, 0.12 m/s current velocity .....                                    | 109 |
| Figure C 2: MAC matrix for TDD method obtained mode shapes, 0.24 m/s current velocity .....                                    | 113 |
| Figure C 3: MAC matrix for TDD method obtained mode shapes, 0.34 m/s current velocity .....                                    | 116 |
| Figure D 1:MAC matrix for Cov-SSI method obtained mode shapes, 0.12 m/s current velocity                                       | 119 |
| Figure D 2: MAC matrix for Cov-SSI method obtained mode shapes, 0.24 m/s current velocity .....                                | 121 |
| Figure D 3: MAC matrix for Cov-SSI method obtained mode shapes, 0.34 m/s current velocity .....                                | 123 |
| Figure D 4: MAC matrix for DD-SSI method obtained mode shapes, 0.12 m/s current velocity .....                                 | 126 |
| Figure D 5: MAC matrix for DD-SSI method obtained mode shapes, 0.24 m/s current velocity .....                                 | 129 |
| Figure D 6: MAC matrix for DD-SSI method obtained mode shapes, 0.34 m/s current velocity .....                                 | 133 |
| Figure D 7: MAC matrix for p-LSCF method obtained mode shapes, 0.12 m/s current velocity .....                                 | 136 |
| Figure D 8: MAC matrix for p-LSCF method obtained mode shapes, 0.24 m/s current velocity .....                                 | 139 |
| Figure D 9: MAC matrix for p-LSCF method obtained mode shapes, 0.34 m/s current velocity .....                                 | 143 |

---



---

# List of Tables

|   |    |
|---|----|
| Table 3.1: Comparison of lumped and consistent mass matrices for the case study catenary                      | 33 |
| Table 5.1: Dimensions of MARINTEK Towing Tank No.3 .....  | 55 |
| Table 5.2: Catenary properties used as input for static configurations and modal calculations (Lie 2001)..... | 57 |
| Table 5.3: Accelerometer locations (Lie 2001). .....  | 58 |
| Table 5.4: Preliminary calculations of natural frequencies and excitation velocities (Lie 2001). .....        | 59 |
| Table 5.5: Towing results selected for the Case Study.....  | 64 |
| Table 5.6: Eigenvalue comparison of FEM solutions relative to the WKB method solutions.                       | 65 |
| Table 5.7: Identified natural frequencies using the TDD method on 0.12 m/s flow velocity results .....        | 69 |
| Table 5.8: Identified natural frequencies using the TDD method on 0.24 m/s flow velocity results .....        | 70 |
| Table 5.9: Identified natural frequencies using the TDD method on 0.34 m/s flow velocity results .....        | 71 |
| Table 5.10: Identified natural frequencies using the p-LSCF method on 0.12 m/s flow velocity results .....    | 75 |
| Table 5.11: Identified natural frequencies using the p-LSCF method on 0.24 m/s flow velocity results .....    | 75 |
| Table 5.12: Identified natural frequencies using the p-LSCF method on 0.34 m/s flow velocity results .....    | 76 |
| Table 5.13: Identified natural frequencies using the Cov-SSI method on 0.12 m/s flow velocity results .....   | 78 |
| Table 5.14: Identified natural frequencies using the Cov-SSI method on 0.24 m/s flow velocity results .....   | 78 |
| Table 5.15: Identified natural frequencies using the Cov-SSI method on 0.34 m/s flow velocity results .....   | 78 |
| Table 5.16: Identified natural frequencies using the DD-SSI method on 0.12 m/s flow velocity results .....    | 79 |
| Table 5.17: Identified natural frequencies using the DD-SSI method on 0.24 m/s flow velocity results .....    | 80 |

---

|  |     |
|--|-----|
| Table 5.18: Identified natural frequencies using the DD-SSI method on 0.34 m/s flow velocity results ..... | 81  |
| Table 5.19: Boundary conditions of the modeled catenary .....  | 82  |
| Table 5.20: Mass and dimensions of 6 accelerometer cases.....  | 83  |
| Table 5.21: Eigenfrequencies of accelerometer loaded catenary relative to original FEM solution.....       | 86  |
|  |     |
| Table C 1: Results from TDD method, 0.12 m/s flow velocity .....   | 107 |
| Table C 2: Results from TDD method, 0.24 m/s flow velocity .....   | 110 |
| Table C 3: Results from TDD method, 0.34 m/s flow velocity .....   | 114 |
| Table D 1: Results from Cov-SSI method, 0.12 m/s flow velocity   | 117 |
| Table D 2: Results from Cov-SSI method, 0.24 m/s flow velocity .....                                       | 120 |
| Table D 3: Results from Cov-SSI method, 0.34 m/s flow velocity .....                                       | 122 |
| Table D 4: Results from DD-SSI method, 0.12 m/s flow velocity .....  | 124 |
| Table D 5: Results from DD-SSI method, 0.24 m/s flow velocity .....  | 127 |
| Table D 6: Results from DD-SSI method, 0.34 m/s flow velocity .....  | 130 |
| Table D 7: Results from p-LSCF method, 0.12 m/s flow velocity .....  | 134 |
| Table D 8: Results from p-LSCF method, 0.24 m/s flow velocity .....  | 137 |
| Table D 9: Results from p-LSCF method, 0.34m/s flow velocity .....   | 140 |



---

## Acronyms and Abbreviations

|              |   |
|--------------|---|
| CF           | Cross-Flow  |
| CFD          | Computational Fluid Dynamics                              |
| CMIF         | Complex Mode Indicator Function                           |
| Cov-SSI      | Covariance-Driven Stochastic Subspace Identification      |
| DD-SSI       | Data-Driven Stochastic Subspace Identification            |
| DFT          | Discrete Fourier Transform                                |
| DNV          | Det Norske Veritas  |
| DOF          | Degree of Freedom   |
| EMA          | Experimental Modal Analysis                               |
| ERADC        | Eigensystem realization algorithm using data correlations |
| FD           | Frequency Domain  |
| FDD          | Frequency Domain Decomposition                            |
| FEM          | Finite Element Method                                     |
| FRF          | Frequency Response Function                               |
| GUI          | Graphical User Interface                                  |
| IL           | In-Line   |
| MAC          | Modal Assurance Criterion                                 |
| MARIN<br>TEK | Marine Technology Research Institute                      |
| MDOF         | Multi Degree of Freedom                                   |
| MFD          | Matrix Fraction Description                               |
| MPC          | Modal Phase Collinearity                                  |
| MPD          | Mean Phase Deviation                                      |
| OMA          | Operational Modal Analysis                                |
| p-LSCF       | Poly-reference Least Squares Complex Frequency            |
| PSD          | Power Spectral Density                                    |
| SCR          | Steel Catenary Riser                                      |
| SDOF         | Single Degree of Freedom                                  |
| STRIDE       | Steel Riser in Deepwater Environments                     |

---

|     |                                    |
|-----|------------------------------------|
| SSI | Stochastic Subspace Identification |
| SVD | Singular Value Decomposition       |
| TD  | Time Domain                        |
| TDD | Time Domain Decomposition          |
| TDP | Touch Down Point                   |
| VIV | Vortex Induced Vibrations          |
| WKB | Wentzel-Kramers-Brillouin          |

## Symbols

The following tables includes a number of general symbol definitions. Some symbols may have different meanings depending on their context in the various chapters, and their local definitions are found in the corresponding text.

|               |                       |
|---------------|-----------------------|
| {}            | Vector                |
| []            | Matrix                |
| $\delta$      | Logarithmic decrement |
| $\Delta$      | Increment             |
| $\varepsilon$ | Strain (Chapter 3)    |
| $\varepsilon$ | Error (Chapter 4)     |
| $\theta$      | Angle/phase           |
| $\lambda$     | Eigenvalue            |
| $\mu$         | Mean                  |
| $\nu$         | Kinematic viscosity   |
| $\xi$         | Damping ratio         |
| $\rho$        | Density               |
| $\phi$        | Mode shape            |
| $\Phi$        | Modal matrix          |
| $\omega$      | Circular frequency    |
| $A$           | Amplitude (Chapter 2) |
| $A$           | Area (Chapter 3)      |
| $c$           | Damping               |

---

|             |  |
|-------------|--|
| $C_A$       | Coefficient of added mass                    |
| $C_D$       | Coefficient of drag                          |
| $C_M$       | Coefficient of mass                          |
| $C_{xy}$    | Cross-covariance function                    |
| $D$         | Diameter                                     |
| $E$         | Young's modulus                              |
| $F$         | Force  |
| $f$         | Frequency                                    |
| $f_s$       | Shedding frequency                           |
| $f_T$       | Sampling frequency                           |
| $G_{xy}$    | One-sided PSD                                |
| $H(\omega)$ | Frequency response function                  |
| $I$         | Moment of inertia                            |
| $k$         | Characteristic size of roughness (Chapter 2) |
| $k$         | Stiffness (Chapter 3)                        |
| $L$         | Length                                       |
| $m$         | Mass   |
| $N$         | Degrees of freedom                           |
| $P$         | Surface pressure                             |
| $p(t)$      | Time-dependent force                         |
| $Q$         | Scaling factor                               |
| $q$         | Time dependent contribution factor           |
| $R_{xy}$    | Cross-correlation function                   |
| $s$         | Lagrangian coordinate                        |
| $S_{xy}$    | Two-sided PSD                                |
| $T$         | Period (Chapter 2)                           |
| $T$         | Tension (Chapter 3)                          |
| $t$         | Time   |
| $U$         | Fluid velocity                               |
| $w$         | Wet weight                                   |
| $X$         | Fourier coefficient                          |

---

---

|            |              |
|------------|--------------|
| $y$        | Displacement |
| $\dot{y}$  | Velocity     |
| $\ddot{y}$ | Acceleration |

## Useful Non-dimensional Parameters

$$Re = \frac{UD}{\nu} \quad \text{Reynold's number}$$

$$St = \frac{f_s D}{U} \quad \text{Strouhal number}$$

$$U_r = \frac{UT}{D} = \frac{U}{fD} \quad \text{Reduced velocity}$$

$$\frac{k}{D} \quad \text{Roughness number}$$

$$\frac{A}{D} \quad \text{Dimensionless amplitude}$$

---

# Chapter 1

## Introduction

### 1.1 Background

The oil and gas industry is one of the largest industries in the world, and was estimated to provide 40.7% of the world's energy demand in 2014 (IEA 2014). Although clean energy solutions are preferable, they are not equipped to serve the world's energy requirement in full in the near future, so we will have to depend on fossil fuels for a while longer. As the lifetime of the oil fields in production today is comparatively short, there is a need to explore reserves in deeper and more complex locations. This puts a larger strain on systems both under installation and operation, and leads to the required development of optimized solutions to increase capacities without an inflation of cost.

One of the reasons why we do not have a clean energy solution providing a larger part of the world's energy demand is that most of them are not feasible in the near future. That is, the time it takes for the extracted energy to pay off the installation cost is still too long. This calls for major optimizations to lower prices. For example, floating wind turbines require better mooring and electricity transport systems, which often take the shape of catenaries, see Figure 1.1.

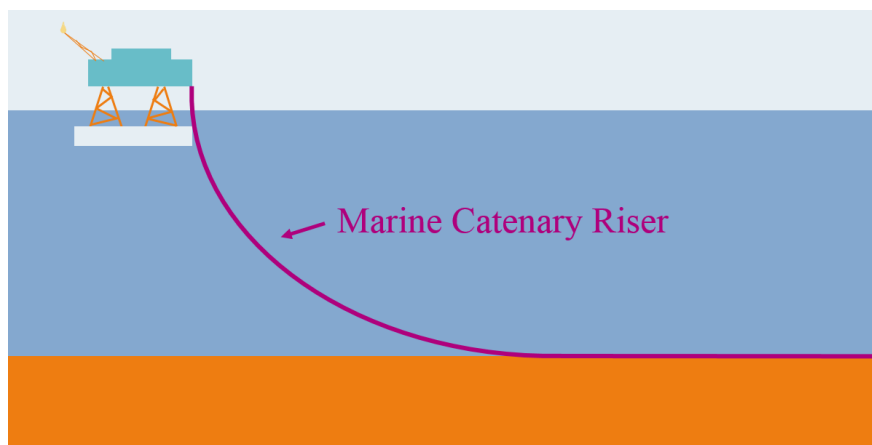


*Figure 1.1: Example of a catenary shaped structural element*

---

Slender catenary-shaped structural elements are found in a wide range of on- and offshore engineering applications, and are preferred due to their cost efficiency. They are found in suspension bridges, transmission lines, in moorings of offshore structures, as well as steel and flexible risers, pipelines under laying and free-spanning pipelines. However, this slender structural shape is not without its disadvantages. Its susceptibility to vortex-induced vibrations (VIV) results in a potential for fatigue damage, which in a worst-case scenario could lead to failure. Therefore, it is important that the vibrations can be well estimated and understood, so that the risk of failure by use of catenary shaped structures can be reduced.

To ensure the safe and optimal design of such structures, dynamic analysis is a must. This requires the prediction of natural frequencies, mode shapes and modal damping before analysis of the structures interaction with loading can be carried out. This can be done using either analytical, numerical or experimental methods.

In 2001 an extensive model test program was carried out in order to better understand the behavior of a steel catenary riser (SCR) subject to VIV at various angles. The experiments were carried out by 2H Offshore Engineering, and subcontracted to MARINTEK. Following the experiments, multiple studies have improved the understanding of the presented data, both through system identification, and by trying to predict the observed responses analytically and numerically.

One of the research groups that has been investigating the data consists of Geir Moe, Torbjørn Teigen, John M. Niedzwecki, Raed Lubbad and Sam Fang. In their work, they have studied displacement envelopes, frequencies, probability of exceedance distributions, effect of time-series truncation and more (Moe et al. 2004; Niedzwecki & Moe 2005; Niedzwecki & Moe 2007). Fang and Niedzwecki have also investigated the data using operational modal analysis techniques (OMA), more specifically the time domain decomposition (TDD) method that will be introduced in Section 4.3.1, and some of their unpublished results have been obtained by personal communication with the authors.

Additionally, inspired by the studies of experimental data, attempts have been made at predicting natural frequencies and mode shapes of catenaries by analytical solutions. These solutions are based on methods first presented in the 1980's, but have been modified to better suit steel catenary risers by modifying assumptions and input (Lubbad & Moe 2008; Lubbad et al. 2011). They have also been compared with numerical solutions such as finite element method analysis, seeking similarities and differences in the various solution methods.

Despite extensive studies showing good results, there is still a gap between the mode shapes and natural frequencies of the analytical and numerical solutions in comparison with experimentally obtained results. For example, there are clear eccentricities in the mode shape shown to the left in Figure 1.2 in comparison with the one to the right. Note that the difference in magnitudes of (a) and (b) in Figure 1.2 are consequences of normalization of the mode shapes, but the anomalies result from other apparent, but unknown effects.

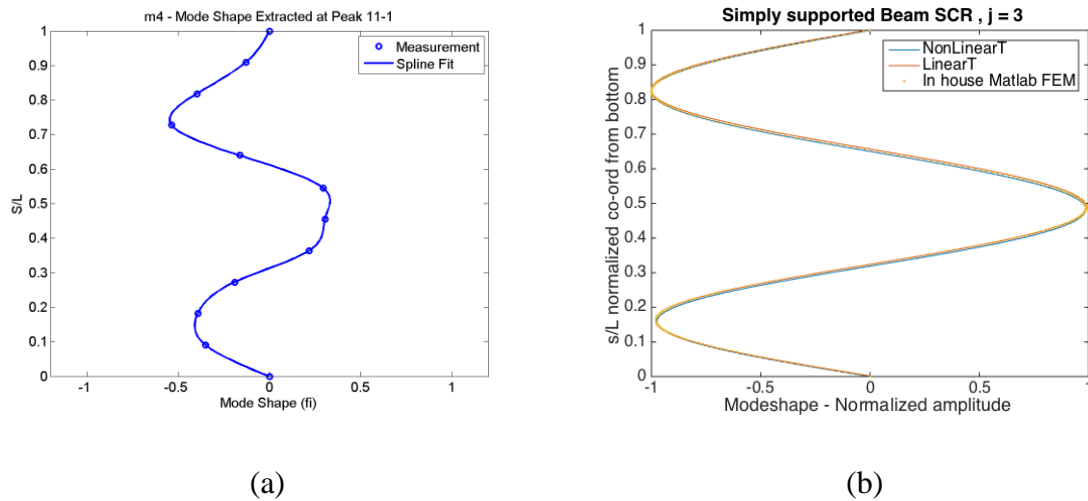


Figure 1.2: (a) Mode shape obtained from TDD of experimental data excited at 1.20 Hz. (b) Mode shape obtained from analytical and numerical solutions corresponding to an eigenfrequency of 1.05-1.08 Hz

## 1.2 Motivation and scope of work

The above mentioned deviations are what inspired the work presented in this thesis. To bridge the gap between the analytical or numerical solutions, and the experimentally obtained results, an investigation is carried out into multiple possible causes of the eccentricities. Possible sources of error are flaws in the system identification methods, or consequences of physical effects that are neglected in the analytically obtained modes. The sources of error will be investigated by a case study of the data from the MARINTEK experiment.

Firstly, the TDD method will be implemented and studied, altering the method of obtaining natural frequencies and damping from what is called the half-power bandwidth method to a correlation method presented in (Brincker et al. 2001).

Secondly, the experimental data will be studied applying other system identification methods in the commercial Matlab toolbox MACEC, presented in Section 5.4, to get an understanding

---

of the applicability of the TDD method results and to investigate whether the other methods can give a better understanding of the data.

Thirdly, the numerical methods of obtaining natural frequencies and mode shapes will be modified to investigate the possible issue of inertia effects due to the masses and volumes of the accelerometers.



---

## 1.3 Structure of thesis

**Chapter 1** aims to give the reader insight into the background and motivation for conducting the work associated with this thesis, along with giving an overview of the thesis structure and potential readership.

**Chapter 2** presents the general theory associated with vortex induced vibrations, including some relevant dimensionless parameters, the concept of shedding frequencies, cross-flow and in-line responses and more.

**Chapter 3** follows from Chapter 2, describing the dynamics of slender structures resulting from vibrations caused by vortices. Modal analysis solutions of un-damped systems are presented for both time and frequency domain, as well as modal analysis solutions of damped structural systems. Continuing, the static solution, i.e. catenary shape, is presented. This is described by multiple solutions to the inertia and damping free equation of motion with various assumptions. Finally, the chapter gives a presentation and discussion of the analytical and numerical solutions to the equation of motion for un-damped and damped catenary shaped structures.

**Chapter 4** focuses on system identification methods, introducing relevant terminology and relations in signal processing. The theory of the implemented TDD method is discussed, as well as the applied methods available in the MACEC toolbox, showing their differences in assumptions and derivations.

**Chapter 5** opens with an introduction to the experiment conducted in 2001 at the MARINTEK venue, including a description of the experiment setup, as well as general results. Subsequently, the chapter presents the case study for this thesis, followed by the various methods and relevant results. Following the results are discussions of observations made when comparing the results with each other and theoretical facts.

**Chapter 6** concludes the thesis, giving an overview of findings.

**Chapter 7** gives recommendations for further work.

---

## 1.4 Readership

The main focus of this thesis is given to slender marine structures with a catenary shape, more specifically SCRs. It highlights main concepts associated with vortex induced vibrations, as well as multiple solution methods to the dynamics of SCRs subject to it. Also, the concepts of system identification are brought forward as a method of studying experimental VIV measurements. The readership of this thesis is, therefore, students seeking insight into fundamental theories of VIV, dynamics and system identification, as well as engineers, lecturers or scientists looking to extend their insight into the concepts, and use the results and recommendations as inspiration for further work.

---

## Chapter 2

# Theory of Vortex Induced Vibrations

This chapter presents general principles necessary for the understanding of vortex induced vibrations and its consequences.

### 2.1 The process of vortex shedding

Vortex-induced vibrations are caused by the shedding of vortices from the structure, and can occur in air as well as in ocean currents. The vortices are caused by the fluid movement around the structure, which again is driven by the conservation of mass, momentum and energy. The Bernoulli equation, i.e. Eqs. 2.1 and 2.2, are used to explain the mechanism of vortex shedding (Faltinsen 1993).

$$P_t + \frac{1}{2}U_t^2 = P_0 + \frac{\rho}{2}U_\infty^2 \quad (2.1)$$

$$U_t = 2U_\infty \sin\theta \quad (2.2)$$

where

- $U_t$  Tangential velocity along the surface
- $U_\infty$  Fluid velocity at a distance from object
- $P_t$  Surface pressure at tangential point  $t$
- $P_0$  Surface pressure at  $\theta = 0$
- $\rho$  Fluid density
- $\theta$  Angular coordinate

As Equations 2.1 and 2.2 imply, the pressure at the volume surface reduces as the tangential velocity increases. When the velocity passes its maximum at  $\theta = \pi/2$ , the pressure will increase towards the volume aft, as the velocity decreases. The fluid will seek towards the aft of the object to regain kinetic energy.

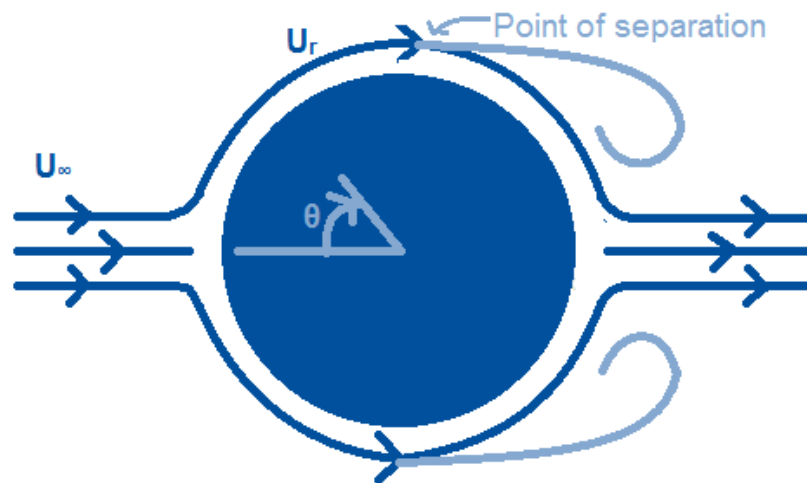


Figure 2.1: Cross-section subject to fluid flow and fluid separation

This idealized potential flow formulation of the Bernoulli equation and the tangential velocity assumes laminar flow around the whole object. This is, however, rarely the case, and the description of the flow behind  $\theta = \pi/2$  becomes dependent on the Reynolds number, explained below. The fluid loses energy to friction force as it flows around the object. If the loss of energy is large enough, the fluid will separate from the surface at what is called the separation point, see Figure 2.1.

### 2.1.1 Reynolds Number

Reynolds number is a dimensionless number that relates the inertial forces of the fluid, represented by the fluid velocity,  $U$ , and the effective diameter,  $D$ , to the kinematic viscosity. The kinematic viscosity,  $\nu$ , defines the fluids shear resistance to density ratio.

$$Re = \frac{UD}{\nu} \quad (2.3)$$

Figure 2.2 shows the vortex patterns for a cylinder of diameter  $D$  as a function of Reynolds number. As can be seen from the figure, for circular cylinders, the idealized equations for potential flow are only valid for Reynolds numbers below about five.

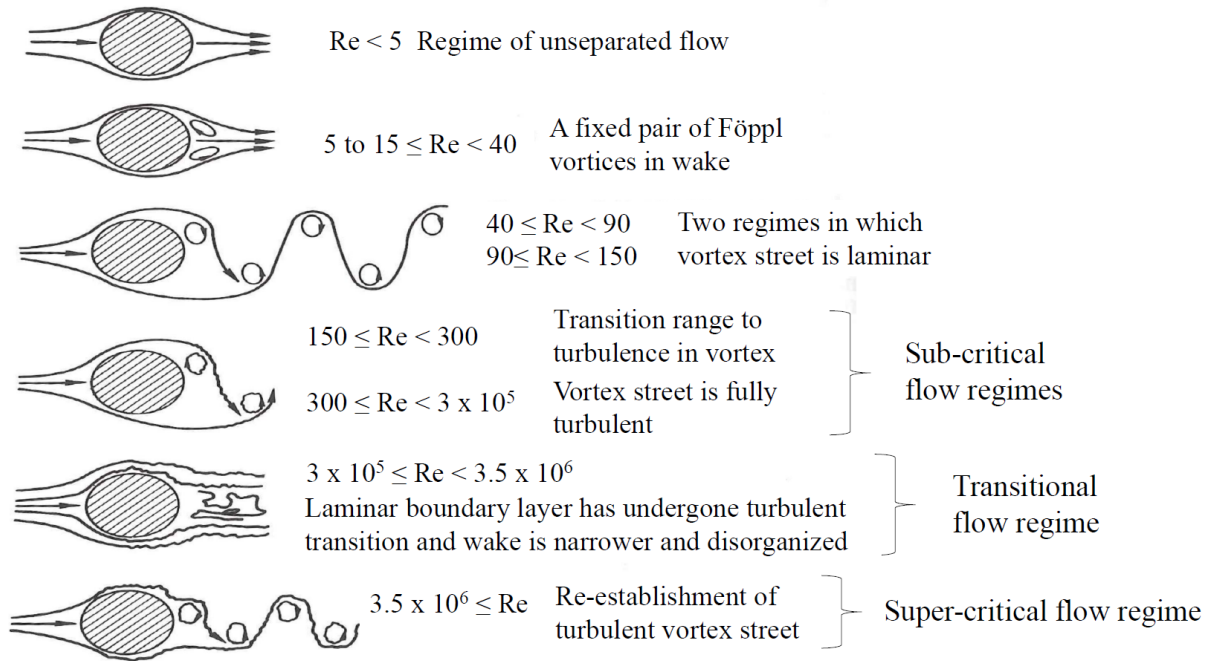


Figure 2.2 Vortex patterns as a function of Reynolds number (Blevins 1994)

The vortices will separate from the structure and produce vortex streets from Reynolds numbers of about 40, but the most interesting Reynolds numbers for studying VIV are found for  $Re > 300$ . Here, the shedding frequency,  $f_s$ , is more likely to reach the natural frequencies of structures, inducing resonance.

### 2.1.2 Strouhal Number

Another useful dimensionless number when studying VIV is the Strouhal number, which is directly related to the Reynolds number, and is defined as

$$S_t = \frac{f_s D}{U} \quad (2.4)$$

The Strouhal number is nearly constant for the sub-critical flow regime (see Figure 2.2) for circular cylinders, with a value of about 0.2, and returns to a near constant state value of 0.24 for the super-critical flow regime (Faltinsen 1993). In the transition flow regime the values of the Strouhal number depends on the surface roughness number, which is defined as

---

$$\frac{k}{D} \quad (2.5)$$

Here,  $k$  is the characteristic size of the roughness.

### 2.1.3 Vortices

The tangential particle velocity at a point along the objects surface is proportional to its radius. As a result, as the fluid separates from the body, the difference in velocity causes shear in the thin fluid layers, resulting in vortices.

At the point in time when a separation first occurs, the shedding of vortices will be symmetric about the structure axis in the flow direction, but as there are instabilities in the vortices, asymmetries will arise. These asymmetries will soon lead to the shedding of vortices alternating between the two sides, creating a vortex street behind the object. As the vortices shed from side to side, pressure variations along the aft of the structure create lift and drag forces, applying thrust forces to the structure. The frequency at which the vortices alternation runs a full circle is known as the shedding frequency, mentioned in the definition of the Strouhal number. When the shedding frequency, reaches a magnitude close to the body's natural frequencies, the object will tend to oscillate. This phenomenon is called lock-in, where the shedding frequency will be locked into the natural oscillating frequency of the structure along its length.

The shedding of vortices and amplitude of oscillation is highly dependent on the shape and surface of the structure cross-section. A circular cylinder is likely to oscillate with an amplitude,  $A$ , close to its diameter,  $D$ , where  $\frac{A}{D} < 1.2$ . In this context,  $\frac{A}{D}$  is also known as the dimensionless amplitude. Moreover, a half cylinder exposed to current hitting the flat side first is likely to become unstable, with amplitudes escalating and ultimately ending in structural failure.

---

### 2.1.4 In-line and cross-flow motions

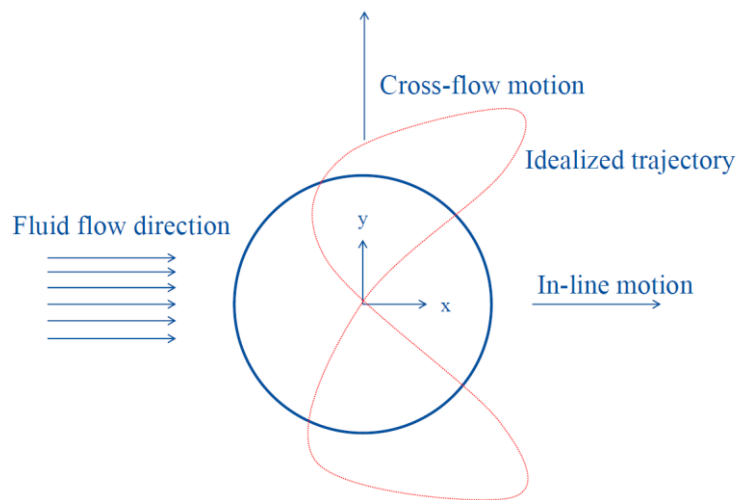


Figure 2.3: Example trajectory of the mid-point of a structure subject to VIV

Directional and perpendicular motions due to VIV are called in-line (IL) and cross-flow (CF) motions respectively. Figure 2.3 shows the idealized trajectory of the cylinder center as a result of VIV, and as previously defined, the shedding frequency is the rate at which the center moves the full trajectory. As can be seen from the figure, the IL motions will occur at twice this frequency, while the CF motion frequency can be associated with the shedding frequency directly.

The figure also displays the difference in magnitude of motions, where the IL motions are usually much smaller than the CF motions. Hence, it is in the CF direction that the cylinder dimensionless amplitude is limited to 1.2.

### 2.1.5 Reduced Velocity

The reduced velocity is often used to describe the path length travelled in the IL direction,  $UT$ , relative to the cylinders diameter. When defining the lock-in velocities for fluid flow, the reduced velocity definition connects the structural natural frequencies directly to the flow velocity.

$$U_r = \frac{UT}{D} = \frac{U}{fD} \quad (2.6)$$

---

### 2.1.6 Hydrodynamic Loading

The steady IL force associated with fluid flow is described by Morison's equation, i.e. Eq.2.7.

$$F_{IL} = C_M \rho \frac{\pi}{4} D^2 \dot{U}_\infty + C_D D \left( \frac{\rho U_\infty^2}{2} \right) \quad (2.7)$$

where

|                  |  |
|------------------|--|
| $F_{IL}$         | In-line thrust force                         |
| $C_M$            | Coefficient of mass                          |
| $C_D$            | Coefficient of drag s                        |
| $\dot{U}_\infty$ | Fluid acceleration at a distance from object |

The formula is similar in both the IL and CF direction. However, the coefficient of drag will be replaced by the coefficient of lift. Vortices add an oscillating part to the fluid flow force in both IL and CF directions. As can be seen in Equation 2.7, the force consists of two separate parts, the force due to the drag, where the drag-coefficient is determined empirically from experiments, and the inertial part. The inertial-coefficient is  $C_M = 1 + C_A$  where  $C_A$  is the added mass coefficient.

It is this added mass coefficients contribution to the loading that is of interest when considering the accelerometer mass' effect on the natural frequencies obtained in the experimental work. Some example added mass coefficients for VIV on free-spanning pipelines in lock-in frequencies are given in Section 4.5 of (DNV 2006). In reality, the added mass depends on the frequency, and will vary along the length of the structure and in time. However, to simplify, the added mass is assumed constant in the work presented in this thesis.

### 2.1.7 Vortex Suppression

In engineering practice, when designing offshore structures, the importance of minimizing the fatigue damage by VIV suppression limits the choice of shapes and materials. The optimal shape is one with reduced form drag, because it is the pressure variation due to drag that is the main cause of separation.

A guide to the VIV mitigation strategies is given in (DNV 2010). It insists that reduction of VIV can be done either by changing structural properties, by changing surface properties, or

---



---

by verifying the structure by model testing. The recommended practice (RP) subdivides the surface modification methods in three categories; surface protrusions, shrouds and wake devices, shown in Figure 2.4. Surface protrusions, such as helical strakes, wires and studs, aim to hinder separation at the structure surface. Shrouds are placed a distance from the structure and aim to divide the flow into many small vortices, while wake devices hinder the building of a vortex street. Following from extensive experimental work on the subject, the RP gives suggestions to modelling considerations when these devices are to be included.

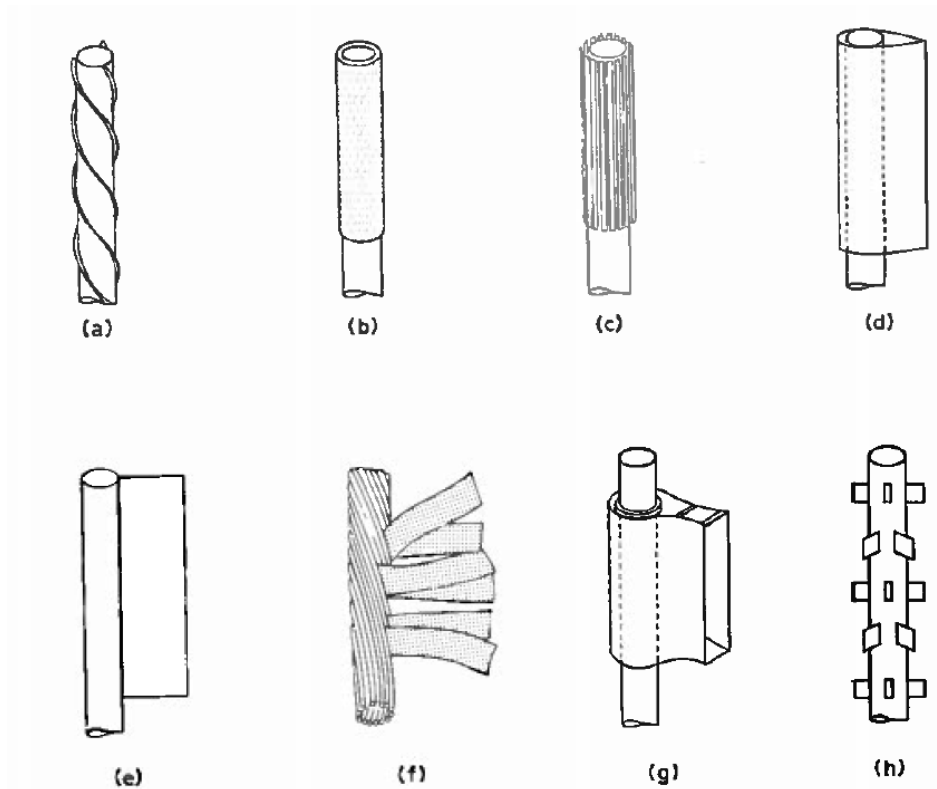


*Figure 2.4: Suppression devices. (a) and (h) are surface protrusions. (b) and (c) work like shrouds. (d)-(g) are forms of wake devices. (Blevins 1994)*

### 2.1.8 VIV Analysis

Blevins discusses methods of VIV analysis in (Blevins 1994). As he points out, the first step is to identify structural modal characteristics, building the foundation for the model. This is usually done using finite element methods (FEM). There are two means of VIV analysis currently in use. Firstly, VIV can be studied by use of finite element solutions to Navier-Stokes equations, by dividing the flow field into a mesh and including a turbulence model. This method is also known as computational fluid dynamics (CFD). Secondly, empirical data

resulting from extensive experimental work can be built into software capable of connecting the structures characteristics to measured responses of similar experiments. An example of this type of software is MARINTEKS's VIVANA.

How modes and mode-shapes participate in vortex induced vibrations along a structure is difficult to predict, and two models are typically used, see Figure 2.5. Firstly, mode shapes are thought to be travelling waves, participating in the whole structure at separate time slots. This model is called the time sharing model, and is shown to the right in Figure 2.5. The second model assumes that multiple frequencies are present at the same time, but that each frequency is participating in a finite area along the structure, and these areas do not overlap. This model is called space sharing, and is shown to the left in the figure below.

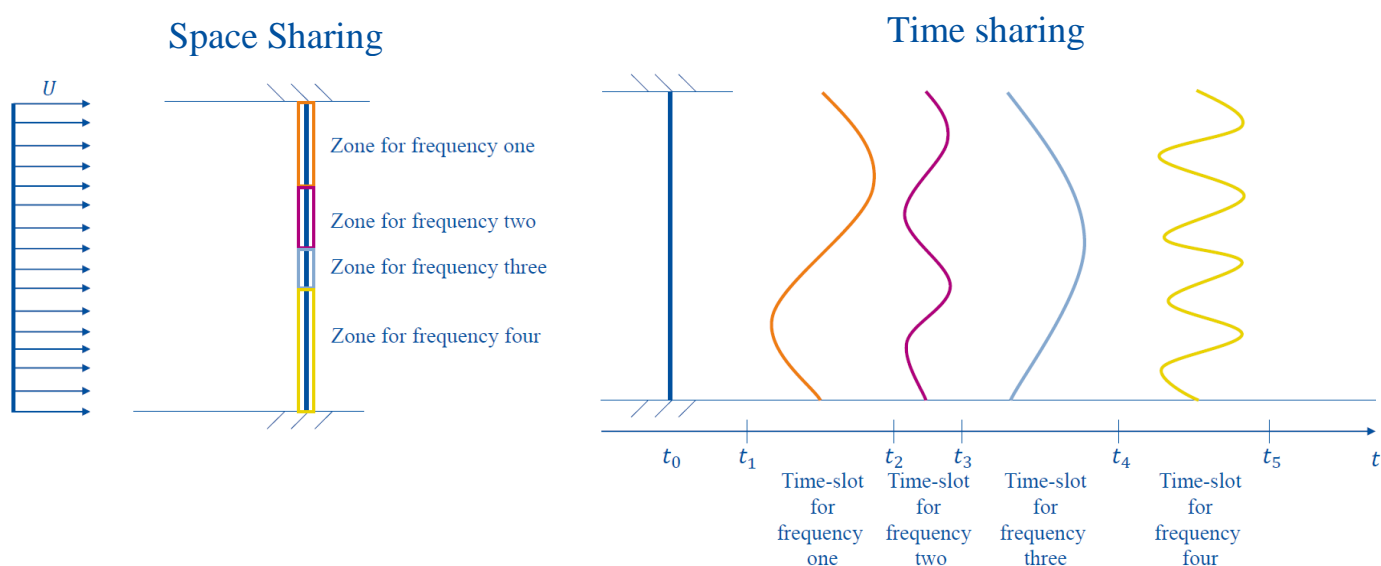


Figure 2.5: Space sharing vs time sharing models of VIV analysis

Continuous improvements in computer's computational capacities are allowing for more complex and accurate VIV analysis tools. However, CFD modelling is still very resource demanding, and the empirical tools are limited to structures consisting of beam elements, so continuous work is needed to improve VIV analysis.

---

## Chapter 3

### Structural analysis of slender catenary structures

The following chapter aims to provide general theory associated with the dynamic analysis of slender catenary structures subject to vortex induced vibrations.

#### 3.1 The equation of motion and solution methods

A structures response to dynamic loading, like vortex-induced vibrations, requires a solution to the equation of motion.

$$m\ddot{y} + c\dot{y} + ky = p(t) \quad (3.1)$$

Describing a structure as a single mass with a single stiffness, moving in a single direction is a major simplification, and the system is therefore better described as a system of equations of motion, as given in Eq.3.2.

$$[M]\{\ddot{y}\} + [C]\{\dot{y}\} + [K]\{y\} = \{p(t)\} \quad (3.2)$$

where  $[M]$ ,  $[C]$  and  $[K]$  are the mass, damping and stiffness matrices respectively, and all of size  $N \times N$ .  $N$  denotes the systems number of degrees of freedom (DOF). Moreover, for Eq. 3.1 to transfer directly to Eq. 3.2, the mass, stiffness and damping would have to be described by infinite degrees of freedom,  $N \rightarrow \infty$ . However, when using methods like the finite element method,  $N$  is finite, and so the accuracy of the calculated responses to loads depends on the chosen number of elements that describe the system.  $\{\ddot{y}\}$ ,  $\{\dot{y}\}$ ,  $\{y\}$  and  $\{p(t)\}$  are the acceleration, velocity, displacement and applied force vectors respectively, and are of size  $N \times 1$ . An idealization of a multi-degree of freedom (MDOF) system is shown in Figure 3.1.

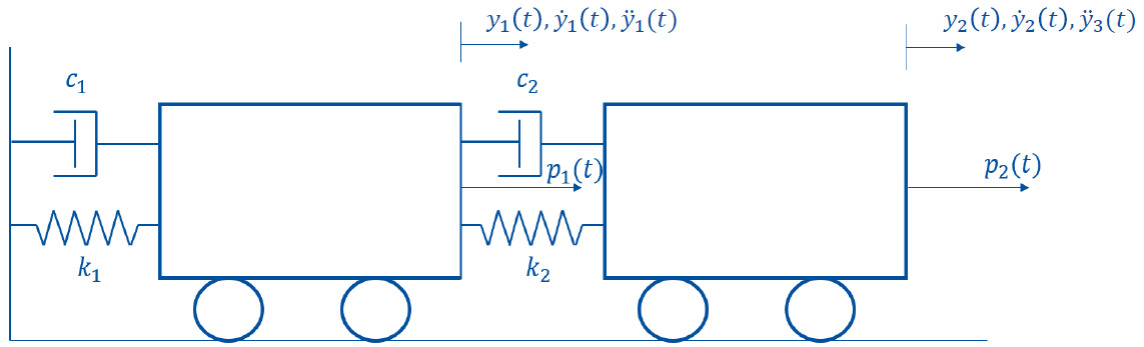


Figure 3.1: A multi-degree of freedom system

Equation 3.2 describes coupled equations of motion, but the simultaneous solution to these equations becomes inefficient as DOF increase. It is therefore more efficient to expand the equation of motion in terms of modal contributions (Chopra 2007). Here, the response is decoupled into a time-dependent part, the contribution factor, and a part describing the shape of the response. The number of different shapes describing the response should also be infinite, but is limited by the number of elements chosen to subdivide the system. Each of these shapes can be viewed as responses of single degree of freedom (SDOF) systems to loading, and the total response is a super-positioning of all of the SDOF responses.

The homogeneous solution to the MDOF system without damping, when  $\{p(t)\} = 0$  and  $[C] = 0$ , has a solution on the form.

$$\{y(t)\} = \{q_n(t)\}\{\phi_n\} = (\{A_n\} \cos \omega_n t + \{B_n\} \sin \omega_n t)\{\phi_n\} \quad (3.3)$$

where  $n$  denotes the DOF,  $q_n$  is the time variation of displacements,  $\phi_n$  is the deflected shape,  $\{A_n\}$  and  $\{B_n\}$  are vectors of constants and  $\omega_n$  is a natural frequency. Substituting Equation 3.3 into Equation 3.2 gives

$$[-\omega_n^2 [M]\{\phi_n\} + [K]\{\phi_n\}]\{q_n(t)\} = 0 \quad (3.4)$$

The only non-trivial solution to Eq. 3.4 is found when

$$\det[[K] - \omega_n^2 [M]] = 0 \quad (3.5)$$

---

This equation is known as the characteristic equation of a system, and solving for  $\omega_n^2$  results in  $N$  real and positive roots, known as the systems eigenvalues. When the natural frequencies,  $\omega_n$ , are known, the corresponding vectors,  $\phi_n$ , known as the mode-shapes, can be found using the equation

$$[[K] - \omega_n^2[M]]\{\phi_n\} = 0 \quad (3.6)$$

The resulting dynamic response, expressed in terms of modal contributions, is given in Equation 3.7.

$$\{y(t)\} = \sum_{r=1}^N \{q_r(t)\}\{\phi_r\} = [\Phi]\{q(t)\} \quad (3.7)$$

The matrix  $\Phi$  is known as the modal matrix, where each column represents the mode-shape corresponding to the eigenvalues of a spectral matrix containing the eigenvalues on the diagonal.  $q_r(t)$  contains scalar multipliers for each DOF of the corresponding  $r^{\text{th}}$  modes with time, and  $q(t)$  is a matrix containing the contributions of all modes.

Substituting for  $y(t)$  in equation 3.2, and multiplying by the transform of the modal matrix results in the equation of motion in terms of modal contributions given by Equation 3.8.

$$[\Phi]^T[M][\Phi]\{\ddot{q}(t)\} + [\Phi]^T[C][\Phi]\{\dot{q}(t)\} + [\Phi]^T[K][\Phi]\{q(t)\} = [\Phi]^T\{p(t)\} \quad (3.8)$$

### 3.1.1 Modal analysis using damped modes

Damping of a system is complicated, not only because it is difficult to predict or know for certain, but also because it complicates the calculations and results of the characteristic equation, given as Equation 3.5 for the un-damped case, and by Equation 3.11 for the damped case. The damping can be categorized by two main groups, classical and non-classical damping. In classical damping, which is usually an idealized form of damping (Chopra 2007), the damping is symmetrically distributed throughout the whole system. For non-classically damped systems, the energy dissipating areas are unevenly distributed, and more difficult to identify.

### 3.1.1.1 Rayleigh Damping

A method of predicting classical damping is with use of Rayleigh damping, Equation 3.9. It assumes that the damping matrix is proportional to both the stiffness and mass matrix, and visualized in Figure 3.2.

$$[C] = a_0[M] + a_1[K] \quad (3.9)$$

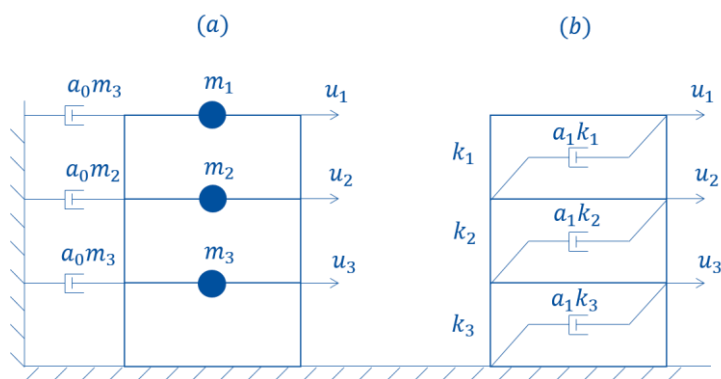


Figure 3.2: Conceptual interpretation of Rayleigh damping, as interpreted from (Crowe 2009)

If the modal damping is known from experimental data, the coefficients  $a_0$  and  $a_1$  can be obtained by Equation 3.10

$$\begin{aligned} a_0 &= 2\xi_n \omega_n \\ a_1 &= \frac{2\xi_n}{\omega_n} \end{aligned} \quad (3.10)$$

where  $\xi_n$  is the damping ratio corresponding to the natural frequency  $\omega_n$ .

### 3.1.2 Calculating Modal Parameters with Damping

$$[[K] + \omega_n[C] + \omega_n^2[M]]\{\phi_n\} = 0 \quad (3.11)$$

As systems that are of interest for VIV are all under-damped, the solutions of Equation 3.11 will all be of complex form, and in complex conjugate pairs. The procedure of obtaining the

---

solutions to 3.11 without the use of major computational effort is done by reducing the second order equation of motion to a system of first order equations (Hoen 2005).

$$\begin{aligned} x &= \begin{bmatrix} y \\ \dot{y} \end{bmatrix} \\ \dot{x} &= \begin{bmatrix} \dot{y} \\ \ddot{y} \end{bmatrix} \end{aligned} \quad (3.12)$$

Where  $x$  is known as a state vector. This results in the equation of motion on the form

$$\begin{aligned} \begin{bmatrix} [I] & [0] \\ [0] & [I] \end{bmatrix} \{\dot{x}\} + \begin{bmatrix} [0] & -[I] \\ [M]^{-1}[K] & [M]^{-1}[C] \end{bmatrix} \{x\} &= \begin{bmatrix} [0] \\ [M]^{-1} \end{bmatrix} \{p\} \\ \{\dot{x}\} &= \underbrace{\begin{bmatrix} [0] & [I] \\ -[M]^{-1}[K] & -[M]^{-1}[C] \end{bmatrix}}_{[A]} \{x\} + \underbrace{\begin{bmatrix} [0] \\ [M]^{-1} \end{bmatrix}}_{[B]} \{p\} \end{aligned} \quad (3.13)$$

Here,  $A$  is a  $2N$  by  $2N$  matrix. Assuming free vibration,  $\{p\} = 0$ , and a solution on the form

$$\{x(t)\} = e^{\lambda t} \{x\} \quad (3.14)$$

where  $\lambda$  are the eigenvalues of the system.

Equation 3.13 can be written as

$$[A]\{x\} = \lambda\{x\} \quad (3.15)$$

And also, because  $\det(A) = \det(A^T)$ .

$$[A]^T\{u\} = \lambda\{u\} \quad (3.16)$$

Solving for  $\lambda$  in both Equation 3.15 and 3.16 results in the same  $2N$  eigenvalues,  $\lambda$ , with  $2N$  corresponding eigenvectors,  $[X] = [x_1, x_2, x_3, \dots, x_{2N}]$  and  $[U] = [\{u_1\}, \{u_2\}, \{u_3\}, \dots, \{u_{2N}\}]$ . These are right and left column eigenvectors respectively, and are related by  $[U]^T = [X]^{-1}$ . The full derivation of this relationship is found in (Hoen 2005).  $\lambda$  consists of  $N$  complex conjugate pairs.

---

Before attempting to plot the mode shapes spatially, it is practical to view the eigenvectors in a complex plane plot. This is useful for determining if the element poles are in a straight line or out of phase with each other, which result in normal or complex modes respectively.

As the response is assumed a linear combination of the  $2N$  solutions of eigenvalues and eigenvectors, following an initial state at  $t = t_0$ , it can be written as Equation 3.17.

$$\{x(t)\} = \sum_{j=1}^N \{x_j\} e^{\lambda_j(t-t_0)} \{u_j\}^T \{x(t_0)\} + \{x_j\}^* e^{\lambda_j^*(t-t_0)} \{u_j\}^{*T} \{x(t_0)\} \quad (3.17)$$

Where  $\lambda_j$  and  $\lambda_j^*$  are complex conjugate pairs. As we are only interested in the displacement solution of  $\{x(t)\}$  in this thesis, we can choose to keep only the first  $N$  elements of  $[X]$  and  $[U]$ , following from 3.12. On polar form the response can be written as

$$y_k(t) = \sum_{j=1}^N 2|u_{j,k}^T x_k(t_0)| |x_{j,k}| e^{-\alpha_j(t-t_0)} \cos(\omega_{j,D}(t-t_0) + \theta_{j,k} + \phi_j(t_0)) \quad (3.18)$$

where

|  |   |
|--|---|
| $\alpha_j = \xi_j \omega_j$              | Damping factor of mode $j$  |
| $ x_{j,k} $                              | Magnitude of state-space eigenvector $j$ , element $k$                          |
| $\omega_{j,D}$                           | Damped circular frequency of mode $j$   |
| $ u_{j,k}^T x_k(t_0) $                   | Initial modal amplitude of mode $j$ corresponding to the initial state $x(t_0)$ |
| $\omega_j$                               | Un-damped circular frequency of mode $j$  |
| $\xi_j$                                  | Damping ratio of mode $j$   |
| $\theta_{j,k}$                           | Modal phase corresponding to element $k$  |
| $\phi_j(t_0) = \arg(u_{j,k}^T x_k(t_0))$ | Initial modal phase corresponding to mode $j$ .                                 |

Where  $\omega_j$  and  $\xi_j$  are given by Equations 3.19 and 3.20 (Lallement & Inman 1995).



---


$$\omega_j = \sqrt{\text{Re}(\lambda_j) + \text{Im}(\lambda_j)} \quad (3.19)$$

$$\xi_j = -\frac{\text{Re}(\lambda_j)}{\sqrt{\text{Re}(\lambda_j) + \text{Im}(\lambda_j)}} \quad (3.20)$$

In the case of proportionally damped systems, the modal phase corresponding to element  $k$  is expected to be zero, meaning that the components of a mode lie on a straight line in the complex plane. As a result, the mode shapes are similar to those found by normal un-damped modal analysis, but the mode shapes occur when exposed to frequencies corresponding to the damped natural frequencies, and the various shapes are phase-shifted relative to each other. This is practical for trying to recreate a response of a system with structural damping, but does not allow for the identification of mode shapes with phase-shifts between elements.

### 3.1.3 Modal Analysis in the Frequency Domain

Equation 3.2 can also be solved for a given harmonic loading,  $\{p_k(t)\} = \{p_{0,k}\} \cdot e^{i\omega_k t}$ , where  $k$  links the amplitude to the frequency  $\omega$ . The response to this load is assumed to be

$$\{y_k(t)\} = \{G_k\} e^{i\omega_k t} \quad (3.21)$$

where  $\{G_k\}$  is a vector of constants. Substituting for  $\{y\}$  in 3.2 with 3.21 results in the following equation

$$\{G_k\} e^{i\omega_k t} (-\omega_k^2 [M] + i\omega_k [C] + [K]) = \{p_k(t)\} \quad (3.22)$$

So as a result, the response to a given harmonic loading  $\{p_k(t)\}$  is

$$\{y_k(t)\} = (-\omega_k^2 [M] + i\omega_k [C] + [K])^{-1} \cdot \{p_k(t)\} = [H(\omega_k)] \cdot \{p_k(t)\} \quad (3.23)$$

Where  $[H(\omega_k)]$  is known as the frequency response to a given frequency  $\omega_k$  (FRF). As this same derivation can be given to any frequency,  $\omega$ , the frequency response function can be generalized as

---


$$[H(\omega)] = (-\omega^2[M] + i\omega[C] + [K])^{-1} \quad (3.24)$$

This is useful when the load and response are transformed to the frequency domain through Fourier transformations, which will be presented in Section 4.1. The resulting link of the load and response in the frequency domain is given by Equation 3.25.

$$[Y(\omega)] = [H(\omega)][P(\omega)] \quad (3.25)$$

### 3.2 Static analysis of slender catenary structures

The catenary is defined as the shape a chain or a cable assumes under its own weight when supported only at its ends, as shown in Figure 3.3. To find the characteristics of a catenary shaped structure in terms of vibration response, it is necessary to model the shape of the catenary in terms of tension, position and angle along its length. This requires solving the equation of motion, Eq. 3.2, for the case of no inertia or damping terms. Multiple theories and assumptions exist for the prediction of catenary configuration. First, one can distinguish between solutions where the catenary is thought to be inelastic and flexible (also known as line or cable theories), and solutions where the bending stiffness is thought to play a large role in the shape (also known as beam formulations). Secondly, it is possible to determine the shape either analytically or numerically using the finite element method (FEM).

In cable formulations of the catenary shape, the cables axial tension is thought to play a major role in the shape that the line takes. As discussed in (Moe & Arntsen 2001), one must also consider whether the cable is extensible or not. None of the presented theories allow for interaction with the seabed in the prediction of shape, so the starting point in terms of  $x$ -direction is taken from the catenaries touch-down-point (TDP), the point at which it first lifts from its foundation.

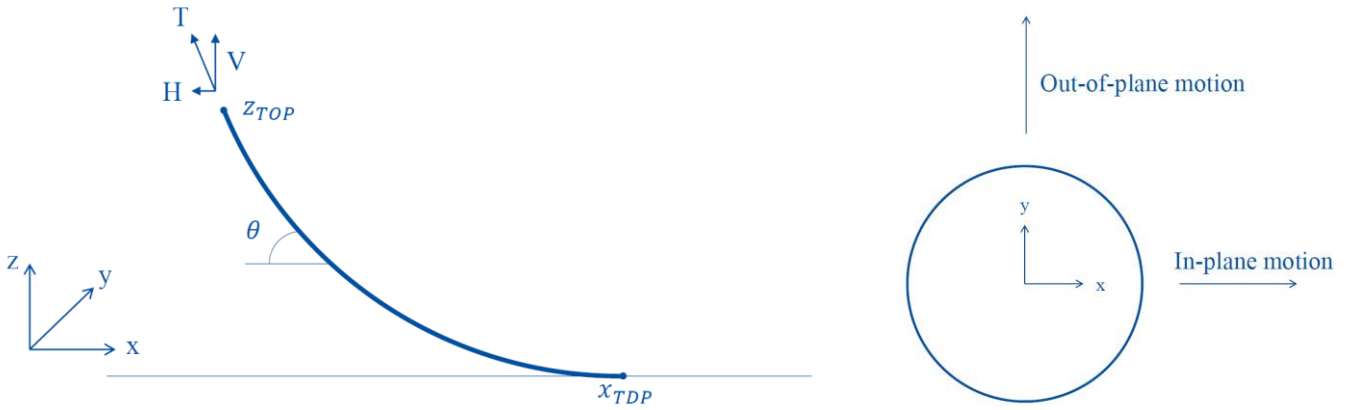


Figure 3.3: The catenary plane, and the catenary cross-section

### 3.2.1 Inextensible cable

The cable self-weight and tension are described in Equation 3.26 and 3.27 respectively. Here, the wet-weight is simply the weight of the riser plus its content, subtracting the buoyancy. The force in the catenary walls resulting from the self-weight, plus the force due to the external pressure, subtracting the force due to the internal pressure, describe the tension.

$$w = \rho_s g A_s + \rho_i g A_i - \rho_e g A_e \quad (3.26)$$

$$T_{eff} = T_{wall} + P_e A_e - P_i A_i = T_e \quad (3.27)$$

where

- $w$  Wet Weight
- $\rho_s$  Structure material density
- $\rho_i$  Internal content density
- $\rho_e$  External fluid density
- $T_{wall}$  Tension in wall due to self-weight
- $P_i$  Internal pressure
- $A$  Area of material cross-section
- $A_i$  Area of internal void
- $A_e$  Total area of cross-section
- $T_{eff}$  Effective tension
- $P_e$  External pressure

When the axial stiffness is assumed large enough that the cable does not elongate due to its own weight, the solution to the catenary shape is in accordance with inextensible theory. Furthermore, the tension along the line can be decomposed into a vertical component  $V$ , and a horizontal component  $H$ , see Figure 3.3. As the catenary is assumed to be loaded only by its own weight, the horizontal component of the tension will be constant. Therefore, the vertical component can be expressed as a function of the horizontal component and the variation of profile along the length,  $\frac{dz}{dx}$ . Introducing a suggested solution of this derivative, Equation 3.28, Equation 3.29 is obtained from integration.

$$\frac{dz}{dx} = \sinh\left(\frac{w\tilde{x}}{H}\right) \quad (3.28)$$

$$z(\tilde{x}) = \frac{H}{w} \left( \cosh\left(\frac{w\tilde{x}}{H}\right) - 1 \right) \quad (3.29)$$

$$\tilde{x} = x - x_{TDP} \quad (3.30)$$

where

- $x$     x-directional coordinate
- $z$     z-directional coordinate
- $H$     Horizontal tension component

The height at which the riser is supported, that is  $z_{top}$ , is usually known. To describe the rest of the catenary using Eq.3.28 and Eq.3.29 requires that an additional parameter is known. This can be either the horizontal component of tension,  $H$ , the top angle,  $\theta = \arctan\left(-\sin\left(w \cdot \frac{x_{TDP}}{H}\right)\right)$ , x-coordinate at the touch-down-point (TDP),  $x_{TDP}$ , or the axial tension specified along the full length.

### 3.2.2 Extensible cable

In catenaries where the density of the material outweighs the material strength, the inclusion of the materials axial stiffness,  $EA$ , is needed. Here,  $E$  is short for the material Young's modulus, and  $A$  is the cross section area. An interpretation of this theory is presented in (Triantafyllou et al. 1985), although the full derivation is not included in the article. However, the basic principle is that the elongation due to tension,  $\varepsilon = T/EA$ , results in an arc length  $L =$

---

$L_0(1 + \varepsilon)$ , where  $L_0$  denotes the un-stretched arc length. Because the tension varies along the line, the arc length will have to be estimated from an integration of the local elongations at discrete points,  $dL = dL_0(1 + \varepsilon)$ . The resulting formulas are given below.

$$T_e(s) = \sqrt{(H^2 + [V - w(L - s)]^2)} \quad (3.31)$$

$$x(s) = \frac{H}{w} \left( \operatorname{arcsinh} \frac{V - w(L - s)}{H} - \operatorname{arcsinh} \frac{V - wL}{H} \right) + \frac{Hs}{EA} \quad (3.32)$$

$$z(s) = \frac{H}{w} \left( \sqrt{1 + \left( \frac{V - w(L - s)}{H} \right)^2} - \sqrt{1 + \left( \frac{V - wL}{H} \right)^2} \right) + \frac{Hs}{EA} \left( \frac{V}{H} s + \frac{w}{2H} (L - s)^2 \right) \quad (3.33)$$

$$\tan(\theta(s)) = \frac{V}{H} - \frac{w}{H} (L - s) \quad (3.34)$$

where

- $s$  Lagrangian coordinate
- $\theta$  Catenary's angle with the horizontal plane
- $x(s)$  x-coordinate at  $s$
- $z(s)$  z-coordinate at  $s$

As a practical example, the theories of inextensible and extensible catenary shapes are applied to the case study catenary, which will be presented in Chapter 5, and the results are presented in Figure 3.4 and 3.5. As can be seen, for this catenary the effective tension relative to the axial stiffness has little or no effect on the resulting configuration, so either theory can be adapted.

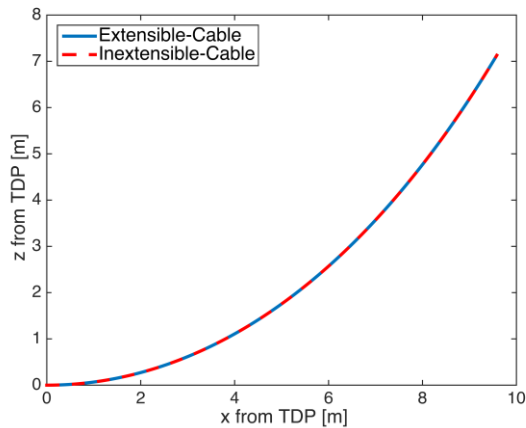


Figure 3.4: Catenary profiles calculated by inextensible and extensible theory

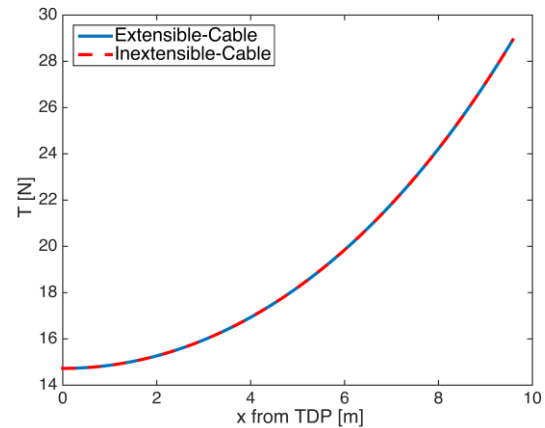


Figure 3.5: Catenary tension distribution calculated using extensible and inextensible cable theory

### 3.2.3 Beam formulations of the catenary shape

The above presented theories both rely on the assumption that the bending stiffness of the catenary has no effect on the configuration of the catenary. Although there are studies in the application of newer mathematical models to predict the catenary shape, (Hsu & Pan 2014), they are still very complex, and to the authors knowledge not widely used and tested. Therefore, the static equilibrium of a catenary including bending stiffness is assumed adequately described using FEM.

Figures 3.6 and 3.7 show how the solutions using cable theory deviate from the FEM modelled shape for the base case given in Chapter 5. Notice that the bending stiffness holds a lot of the weight, lowering the effective tension, which leads to a larger sag of the catenary. Notice also the effect of varying the TDP angle from  $0^\circ$  to  $2^\circ$ , the striped red and blue lines respectively, and how this increases the effective tension along the line.

Lubbad concluded that for the experimental catenary model, the effects of bending stiffness are relatively large, and it is recommended that this static profile should be used when comparing the results of the experimental data with those from the numerical and analytical calculations (Lubbad et al. 2011)

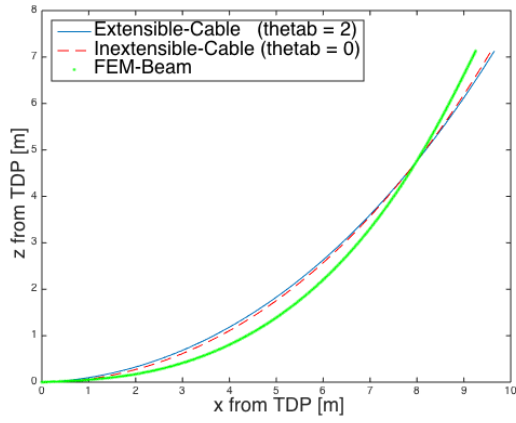


Figure 3.6: Comparison of beam and cable formulations of the catenary profile

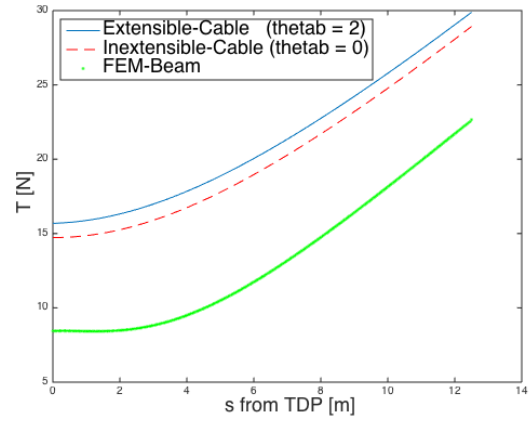


Figure 3.7: Comparison of beam and cable formulations of the tension distribution

### 3.3 Eigenvalue analysis of slender catenary structures

The following will present the various methods applied for solving the equation of motion, Eq. 3.2, for slender catenary structures by means of natural frequencies and mode-shapes. It is important when describing catenary motions to distinguish between in-plane and out-of-plane motions. As pointed out by (Triantafyllou et al. 1985), the directional motions are uncoupled for out-of-plane motions. Therefore, they can be idealized as a taut-string or straight beam with varying tension along the length. The natural frequencies can then be described by Equation 3.35, assuming a near constant tension variation. This near constant tension variation can be obtained using buoyancy devices along the length of the structure.

$$f_i = \frac{i}{2L} \left( \frac{T}{m} \right)^{\frac{1}{2}}, i = 1,2,3, \dots \quad (3.35)$$

where

- $T$  Mean tension
- $m$  Mass per unit length
- $L$  Span between tie downs
- $f_i$  Natural frequency of mode  $i$

Eq. 3.35 is applicable in many cases. However, as the length of catenaries increase, the applicability of these buoyancy solutions may decline. As it is assumed that the axial tension has a large influence on the calculated frequencies, the variation over the riser length should have a profound effect.

The in-plane motions are even more complex, and are dependent on the angle of inclination as well as the tension distribution. The transverse and axial motions are coupled, and it is important to consider both in combination when estimating natural frequencies. Multiple studies have focused on overcoming the difficulties in interaction between varying tension, longitudinal and transverse motion, resulting in multiple derivations with varying assumptions.

Triantafyllou and his team gave an analytical, asymptotic solution to the eigenvalue problem for inclined cables in 1984 (Triantafyllou et al. 1985). In mathematical analysis, asymptotic

---



---

analysis is the practice of estimating limiting behavior. For solving differential equations, this entails finding the singular points of the equation. However, one of the main limitations of the solution presented in 1985 is its shallow-sag formulation. That is, the axial tension at the point on the catenary where the inclination angle is the same as the angle of the total inclination of the cable must be much larger than the cable weight,  $0 < \frac{wL}{T_\theta} \ll 1$ .

In 1983, Kim introduced the application of Wentzel-Kramers-Brillouin (WKB) method to solving the differential equation of long slender beams, assuming that the tension varies slowly along the beam (Kim 1983).

Modified asymptotic solutions were presented in 2008 by Lubbad and Moe (Lubbad & Moe 2008). The differential equation was solved using the “local analysis” method for cables, neglecting bending stiffness, and the WKB method was used for solving the equation when including the bending stiffness term. In the methods presented, the tension variation along the length of the beam was considered linear, which is an assumption fit for estimation of nearly vertical cables or beams.

In 2011, the “local analysis” and WKB techniques were extended to catenary shaped structures by a change in the assumption of tension variation (Lubbad et al. 2011). The tension was approximated by a non-linear function. Section 3.3.1 will present the solutions recommended by this paper. The results from the modifications were compared with a Finite Element Method (FEM) solution to the eigenvalue problem, and the implemented FEM solutions, along with modifications made for this thesis will be discussed in Section 3.3.2.

### 3.3.1 Analytical Methods

#### 3.3.1.1 Asymptotic Method of Cable or String

A catenary’s local displacement as a function of the time  $t$  and vertical distance from the TDP is given by the equation of motion of 3.36.

$$\frac{\partial^2}{\partial z^2} \left( EI \frac{\partial^2 Y(z, t)}{\partial z^2} \right) - \frac{\partial}{\partial z} \left( T \frac{\partial Y(z, t)}{\partial z} \right) + c \frac{\partial Y(z, t)}{\partial t} + m_{tot} \frac{\partial^2 Y(z, t)}{\partial t^2} = f(z, t) \quad (3.36)$$

The indexes used here are similar to those of Section 3.1 and 3.2. When considering Equation 3.36 for a cable or string, the term containing the bending stiffness,  $EI$ , is considered negligible, along with the damping term containing  $c$ . The equation is solved for  $f(z, t) = 0$ . Now assuming a tension variation given as

$$T = H\sqrt{1 + \tan^2 \theta} = H\sqrt{1 + \alpha^2} \quad (3.37)$$

where  $\theta$  is the local angle of the catenary to the horizontal,  $\alpha = \tan \theta$  and  $H$  is still the horizontal tension component. Converting the vertical coordinates  $z$  to the Lagrangian coordinates  $s$ , and with the displacement  $W(s, t)$  along the catenary assumed harmonic, so that  $W(s, t) = w(s) \cos \omega_n t$ . After yet another change of variables, the resulting expected solution is on the form

$$w(\alpha) = e^{S(\alpha)} \quad (3.38)$$

Solving 3.38 with a second order solution, the natural frequencies must be found iteratively using Equation 3.39.

$$\omega_n \left(\frac{L}{\tau}\right) \sqrt{\frac{m}{H}} \cdot \int_0^\tau (1 + \alpha^2)^{-\frac{1}{4}} d\alpha + \frac{1}{\omega_n} \left(\frac{\tau}{L}\right) \frac{1}{8\sqrt{\frac{m}{H}}} \int_0^\tau \frac{(1 + \alpha^2) - 3}{(1 + \alpha^2)^{\frac{7}{4}}} d\alpha = n\pi \quad (3.39)$$

where  $\tau$  is the value of  $\tan \theta$  at  $s = L$  and  $L$ . The corresponding mode-shapes are found by

$$w(\alpha) = (1 + \alpha^2)^{-\frac{1}{4}} \sin \left( \omega_n \sqrt{\frac{m}{H}} \left(\frac{L}{\tau}\right) \int_0^\tau (1 + \alpha^2)^{-\frac{1}{4}} d\alpha + \frac{1}{\omega_n} \left(\frac{\tau}{L}\right) \frac{1}{8\sqrt{\frac{m}{H}}} \int_0^\tau \frac{(1 + \alpha^2) - 3}{(1 + \alpha^2)^{\frac{7}{4}}} d\alpha \right) \quad (3.40)$$

### 3.3.1.2 Asymptotic Solution for a Beam Model

When solving Equation 3.36 without a negligible bending stiffness,  $EI$ , the characteristics of the catenary cannot be resolved by the previously presented local analysis technique.

Therefore, assuming that the tension varies slowly but non-linearly along the catenary, the problem is solved using the WKB method first presented for applications to long, slender beams in (Kim 1983), and later improved by Lubbad and Moe (Lubbad & Moe 2008). The solutions for the natural frequencies as given in (Lubbad et al. 2011) are the roots of Equation 3.41.

$$\frac{\Gamma_n^{1.5}}{b} \left( 2e^{\frac{\xi_n}{2}} - \frac{2}{3}e^{-\frac{3\xi_n}{2}} \right) \bigg|_{\xi_{n_b}}^{\xi_{n_t}} = n\pi \quad (3.41)$$

where

$$a = \frac{HL^2}{EI} \quad b = \frac{(T_t - H)L^2}{EI} \quad \Gamma_n = \frac{\omega_n}{\omega_0} \quad \omega_0 = \sqrt{\frac{EI}{mL^4}}$$

$$\check{s} = \frac{s}{L} \quad \xi_n = \sinh^{-1} \frac{a + b\check{s}}{2\Gamma_n} \quad \xi_{n_b} = \xi_n(\check{s} = 0) \quad \xi_{n_t} = \xi_n(\check{s} = 1)$$

and  $T_t$  is the effective tension in the upper end of the catenary.

The corresponding mode-shapes are calculated by solving Equation 3.42.

$$w_n = \frac{e^{\frac{\xi_n}{4}}}{\sqrt{(\cosh \xi_n)}} \sin \left( \frac{\Gamma_n^{1.5}}{b} \left( 2e^{\frac{\xi_n}{2}} - \frac{2}{3}e^{-\frac{3\xi_n}{2}} \right) \bigg|_{\xi_{n_b}}^{\xi_n} \right) \quad (3.42)$$

### 3.3.2 Finite Element Solutions

When using FEM, the catenary is divided into a net of elements, and the equation of motion given by Eq. 3.36 must be solved for each element separately. Each element is assumed to have three DOF at each node, see Figure 3.8, so that both the CF directional movement and the axial movement is accounted for.

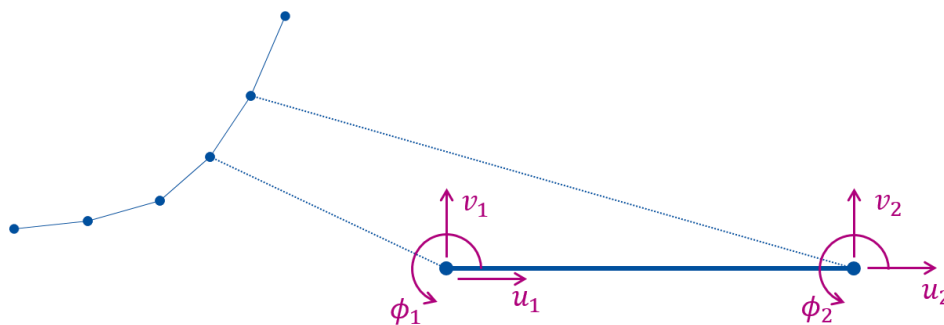


Figure 3.8: The degrees of freedom of a catenary element

### 3.3.2.1 Stiffness Matrix

The assumption of three DOFs at each node results in the local stiffness matrix similar to that for a frame element given on page 26 of (Cook 2002). However, the  $Y_1, Y_2, Y_3$  and  $Y_4$  components are modified to account for the effects of the axial tension as follows

$$K = \begin{bmatrix} X & 0 & 0 & -X & 0 & 0 \\ 0 & Y_1 & Y_2 & 0 & -Y_1 & Y_2 \\ 0 & Y_2 & Y_3 & 0 & -Y_2 & Y_4 \\ -X & 0 & 0 & X & 0 & 0 \\ 0 & -Y_1 & -Y_2 & 0 & Y_1 & -Y_2 \\ 0 & Y_2 & Y_4 & 0 & -Y_2 & Y_3 \end{bmatrix} \begin{bmatrix} u_1 \\ v_1 \\ \phi_1 \\ u_2 \\ v_2 \\ \phi_2 \end{bmatrix} \quad (3.43)$$

$$\begin{aligned} Y_1 &= \frac{12EI}{L^3} + \frac{36T_b}{30L} + \frac{36\Delta T}{60L} & Y_2 &= \frac{6EI}{L^2} + \frac{T_b}{10} + \frac{\Delta T}{10} \\ Y_3 &= \frac{4EI}{L} + \frac{2T_b L}{15} + \frac{\Delta T L}{30} & Y_4 &= \frac{2EI}{L} - \frac{T_b L}{30} - \frac{\Delta T L}{60} \\ X &= \frac{EA}{L} \end{aligned} \quad (3.44)$$

where

$$\begin{aligned} T_b & \quad \text{Tension in lower end of element} \\ \Delta T = T_b - T_t & \quad \text{Tension variation over the element} \end{aligned}$$

### 3.3.2.2 Mass Matrix

The mass matrix used for the original Matlab codes written by Lubbad is a consistent mass matrix for a frame element. Chapter 11.3 of (Cook 2002) explains how this matrix is

determined, and it is based upon the assumption that the shape functions describing the displacements over the elements, which are used when determining the stiffness matrix given in 3.43, are consistent with the variation of the acceleration field over the same element. This mass matrix assumes that the mass is distributed evenly along the element.

However, when applying additional masses at locations throughout the catenary, the mass matrix of the original codes cannot be used, as the total mass can no longer be assumed distributed along the element. Therefore, the simpler mass matrix formulation, the lumped mass matrix, has been implemented, as shown in Eq. 3.45. This formulation assumes that the total mass of the element is divided in two, and placed at the two element nodes. With this interpretation the accelerometer masses can be added at the node corresponding to its location, but divided evenly between the two elements that share this node. The  $\alpha$  of Equation 3.45 is included to account for the associated mass moment of inertia, and should be given a value of  $0 \leq \alpha \leq 1/24$ , following from the formula for rotational inertia. In this thesis, the assumption is made that the rotary inertia has little effect on the calculation of natural frequencies, so  $\alpha \approx 0$ .

$$M = \begin{bmatrix} 1 & 0 & 0 & 0 & 0 & 0 \\ 0 & 1 & 0 & 0 & 0 & 0 \\ 0 & 0 & 2\alpha L^2 & 0 & 0 & 0 \\ 0 & 0 & 0 & 1 & 0 & 0 \\ 0 & 0 & 0 & 0 & 1 & 0 \\ 0 & 0 & 0 & 0 & 0 & 2\alpha L^2 \end{bmatrix} \begin{bmatrix} u_1 \\ v_1 \\ \phi_1 \\ u_2 \\ v_2 \\ \phi_2 \end{bmatrix} \quad (3.45)$$

The lumped mass matrix is a much simpler matrix, and as Cook points out with a number of examples, this mass matrix is expected to have larger errors in comparison with the true natural frequencies of systems. In his examples, it is clear that the expected error is larger for higher modes than in the lower modes. As a practical example, Table 3.1 shows the relative error of the consistent and lumped matrices for the catenary system used for the case study.

*Table 3.1: Comparison of lumped and consistent mass matrices for the case study catenary*

| Eigenfrequency of mode no.  | 1      | 2      | 3      | 4      | 5      | 6      | 7      | 8      | 9      | 10     |
|-----------------------------|--------|--------|--------|--------|--------|--------|--------|--------|--------|--------|
| Consistent mass matrix [Hz] | 0,2256 | 0,5586 | 1,0593 | 1,7435 | 2,6168 | 3,6814 | 4,9382 | 6,3876 | 8,0297 | 9,8647 |
| Lumped mass matrix [Hz]     | 0,2256 | 0,5586 | 1,0593 | 1,7435 | 2,6168 | 3,6814 | 4,9382 | 6,3875 | 8,0296 | 9,8646 |
| Relative error [%]          | 0      | 0,0001 | 0,0001 | 0,0002 | 0,0003 | 0,0004 | 0,0006 | 0,0007 | 0,0009 | 0,0012 |

As can be seen, the difference is of negligible magnitude, but increases slightly with mode number. The relative error could be larger with lumped masses added at multiple locations, as the total effect given by the masses should be larger. However, it is assumed that this difference will still be relatively small. Therefore, the lumped mass matrix is considered sufficient for the comparison of the subsequent added mass comparison.

### 3.3.2.3 The Global Stiffness and Mass Matrices

After the stiffness and mass matrices for each element have been constructed, they must be systemized into a global mass and stiffness matrix for the total system. This is done by first rotating the matrices to the global axis using Equation 3.46, and then adding the matrices using indexes so that the influences of the DOFs that are shared between elements are summed in the global matrix.

$$r = \begin{bmatrix} \cos \theta & \sin \theta & 0 & 0 & 0 & 0 \\ -\sin \theta & \cos \theta & 0 & 0 & 0 & 0 \\ 0 & 0 & 1 & 0 & 0 & 0 \\ 0 & 0 & 0 & \cos \theta & \sin \theta & 0 \\ 0 & 0 & 0 & -\sin \theta & \cos \theta & 0 \\ 0 & 0 & 0 & 0 & 0 & 1 \end{bmatrix} \quad (3.46)$$

### 3.3.2.4 Complex modes

Structures subject to dynamic loading do not necessarily experience large amounts of damping effects, but are rarely without damping at all. For this reason, when attempting to recreate a measured response using numerical or analytical methods, it may be of importance to incorporate some form of damping. As mentioned in Section 3.1.1, a simple method of incorporating the damping effects in the in-house Matlab formulated FEM codes is by use of the theory of Rayleigh damping. The initial  $a_0$  and  $a_1$  values can be based on findings from analysis of the experimental work, using Eq. 3.10. It is important to remember that these calculations do not allow for identification of mode shapes with phases between elements, but could identify the expected damping of each of the modes when recreating the responses.

---

## Chapter 4

# System Identification Methods

System identification methods, which are used for experimental modal analysis (EMA) and OMA, aim to predict the structural properties of a system by studying the output of experimental measurement. The practice of EMA and OMA is based on the assumption that the dynamic behavior of any system can be expressed in terms of modal characteristics, as explained in Section 3.1. In engineering disciplines, modal testing became more widely used during the 1980's (Ewins 2000). Since then, the colossal evolution in computer computational capacities, and the introduction of the FEM, have led to even more robust and reliable tools capable of validating numerical analysis of structures (Rainieri et al. 2014).

The distinction between OMA and EMA lies in the requirements of the input data. While EMA requires that the input load must be known or at least estimated, the OMA techniques require response measurements only. Assumptions made when using OMA are:

- **Linearity:** There is a constant link between an input and the corresponding output.
- **Stationarity:** The systems modal characteristics do not change in time.
- **Observability:** Sensors are located so that the modes of interest are possible to extract from the data. It is important to avoid placing sensors at nodal points, and to have an adequate number of sensors.

As the input loading is not known, the assumption is made that the combined system, that is the excitation system and the structure of interest, are loaded with white noise, see Figure 4.1. White noise is a zero mean random signal with a constant power spectrum. However, if enough data is available, one can distinguish between the properties of the excitation system and the structure system because the structures responses are expected to be narrow band and constant with time, while the excitation system has a broadband response and can be time-invariant.

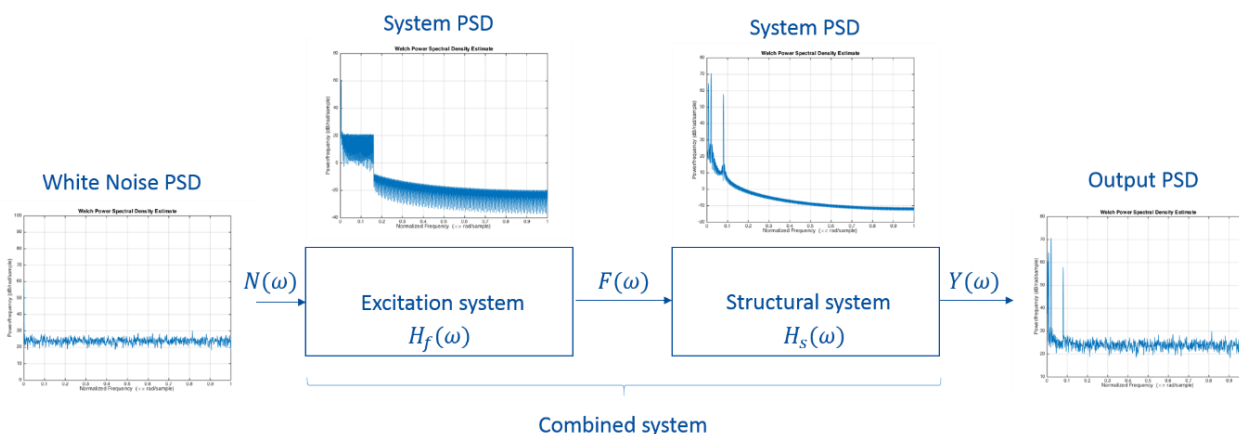


Figure 4.1: Assumed system for OMA applications

OMA is ideal, as the identified modal parameters are found from actual behavior when the system is exposed to actual conditions, and not to idealized artificial vibrations. Other reasons for choosing to apply OMA is that it does not interfere with operational use of a structure, and the input loads do not need to be known.

The methods of gathering measurement data for EMA and OMA are advancing. Structures or models can be equipped with classical measurement systems like accelerometers, extensometers, and strain or tilt gauges, but can now also be investigated with ultrasonic sensors (Carullo & Parvis 2001), laser vibrometers (Giuliani et al. 2003) and fiber optics (Casas et al. 2003). This leads to the attractive fact that the modal analysis can be carried out cheap and fast, and more reliable. There is, however, a limitation in the sensitivity in the required data, which could limit the application of OMA. Also, the assumption of broadband loading does not hold for all cases.

To understand the concepts of system identification, an introduction to the fundamentals of random processes and corresponding mathematical models is needed, and so is presented in the following text. The OMA methods available in the commercial software MACEC (Reynders et al. 2014) will also be introduced, as well as the TDD method (Kim et al. 2005) formerly implemented on a similar catenary analysis (Fang 2014). Basics and concepts presented may only touch the surface of the topics, so the interested reader is referred to (Newland 2005) and (Rainieri et al. 2014) for more in-depth explanations.



---

## 4.1 Random Processes

An output measurement from a structure subject to environmental loading will often look like the time-series to the right in Figure 4.2. As is shown, the signal fluctuates profoundly in time and it is difficult to see any regularities in the data.

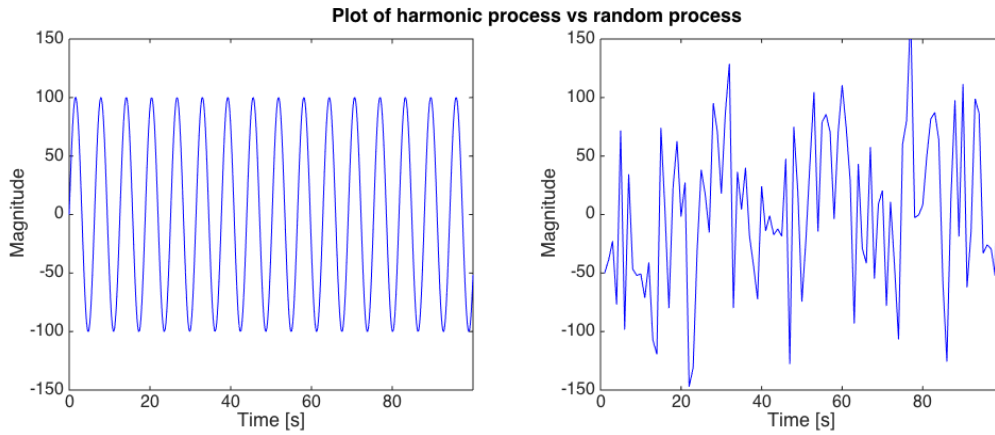


Figure 4.2: Sinusoid signal vs a random process signal.

A solution to describing the fluctuations is the use of Fourier transformations, Eq.4.1 and Eq.4.2. They transform a signal in the time domain (TD) to a signal in the frequency domain (FD), by decomposing the signal as a sum of sinusoids with frequency  $f$ , as shown to the left in Figure 4.2.

$$X(f) = \int_{-\infty}^{\infty} x(t)e^{-i2\pi ft} dt \quad (4.1)$$

$$X_k = \sum_{n=0}^{N-1} x_k e^{-\frac{i2\pi kn}{N}}, \quad k = 0, 1, 2, \dots, N-1 \quad (4.2)$$

$$x(t) = \int_{-\infty}^{\infty} X(f)e^{-i2\pi ft} df \quad (4.3)$$

where

|        |                               |
|--------|-------------------------------|
| $f$    | Frequency                     |
| $x(t)$ | Measured signal               |
| $t$    | Time                          |
| $X(f)$ | Fourier coefficients          |
| $X_k$  | Discrete Fourier coefficients |

---

$N$        $T/\Delta t$

The Fourier coefficient magnitude  $|X_k|$  relates to the magnitude of the sinusoid of frequency  $f_k$ , and the signal phase is described by  $\theta_k$ , Eq.4.4.

$$\theta_k = \arctan\left(\frac{\text{Im}(X_k)}{\text{Re}(X_k)}\right) \quad (4.4)$$

#### 4.1.1 Power Spectral Density

The power spectral density (PSD), is used to describe how the present frequencies are distributed in terms of powers, or magnitudes. As the Fourier transform of Eq.4.1 is integrated from  $-\infty$  to  $\infty$ , the power spectral density will cover both the positive and corresponding negative frequencies. However, the spectral densities are mirrored about the y-axis, and so for practical applications, it is more common to consider only the positive frequencies, given by  $G_{xy}(f)$ .

$$G_{xy}(f) = 2 \cdot S_{xy}(f) = \lim_{T \rightarrow \infty} E\left[\frac{1}{T} X_k^*(f, T) Y_k(f, T)\right] \quad (4.5)$$

where

$S_{xy}(f)$  Two-sided PSD

$G_{xy}(f)$  One-sided PSD

$X_k^*(f, T)$  Complex conjugate of  $X_k$

Here, the  $x$  and  $y$  of  $S_{xy}(f)$  and  $G_{xy}(f)$  denote that the spectrum for the relationship between variables  $x$  and  $y$ , also called the cross-spectrum, while a subscript containing only one variable, or two of the same, represents the auto-spectrum. Generally, these spectrums are complex, where the real part is often called the co-spectrum, and the imaginary part is called the quad-spectrum.

$$S_{xy}(f) = Co_{xy}(f) - iQu_{xy}(f) \quad (4.6)$$

---

### 4.1.2 Convolution

To express how much one function,  $a$ , overlaps another function,  $b$ , as it is shifted over it, one can use a convolution integral, Eq.4.7. A convolution integral can be difficult to solve numerically. However, convolutions in TD correspond to multiplication in FD, so it may be practical to consider signals in FD by Fourier transformations before calculating convolutions, Eq.4.8. Also, the same goes for convolution in FD, which corresponds to multiplication in TD. This is as a result of the relationship between Equations 4.1 and 4.3.

$$c(t) = \int_{-\infty}^{\infty} a(\tau) \cdot b(t - \tau) d\tau = (a(t) * b(t)) \quad (4.7)$$

$$C(f) = A(f) \cdot B(f) \quad (4.8)$$

### 4.1.3 Covariance

The consequence of equation 4.7 and 4.8 is widely used in signal processing, as it allows us to interpret the relationships between signals with ease in both domains. In describing a structures dynamics, an important factor is how far a load or response, or a relationship between two signals, is from being constant in time. This can be described using the covariance, which measures how much two measurement time-series change together, subtracting the mean or constant offset. The equation for covariance is shown in 4.9.

$$C_{xy} = E[(x_k - \mu_x)(y_k - \mu_y)] = \iint_{-\infty}^{\infty} (x_k - \mu_x)(y_k - \mu_y) p(x, y) dx dy \quad (4.9)$$

where

$p(x, y)$  Joint probability density

$x_k$  Random variable  $x$

$\mu_x$  Mean of  $x$

$y_k$  Random variable  $y$

$\mu_y$  Mean of  $y$

In OMA, one of the main assumptions is that the signals are stationary. Stationary signals come from processes where the mean and variance do not change in time, so consequently the joint probability distribution is constant, even when the signal is shifted in time. Equation 4.10 follows from this relationship, and shows that the covariance is only dependent on the lag of one variable in relation to the other in time.

$$C_{xy}(\tau) = E[(x_k(t) - \mu_x)(y_k(t + \tau) - \mu_y)] \quad (4.10)$$

where

|        |          |
|--------|----------|
| $t$    | Time     |
| $\tau$ | Time lag |

#### 4.1.4 Correlation

Covariance is a good way of describing how two signals move together. One can determine whether one increases at the same time as the other increases, positive covariance, or that one increases while the other decreases, negative covariance. However, it does not say to what degree the signals change with one another. This degree of variance is achieved by using the correlation function, Equation 4.11.

$$R_{xy}(\tau) = E[x_k(t)y_k(t + \tau)] \quad (4.11)$$

As for PSDs, the  $x$  and  $y$  represent covariance and correlation between two variables, the cross-covariance, and two identical variables represent auto-covariance or auto-correlation functions.

When the means of the variables are zero, or set to zero by subtracting the actual values, the correlation function and the PSD are related by

$$S_{xy}(f) = \int_{-\infty}^{\infty} R_{xy}(\tau)e^{-i2\pi f\tau} d\tau \quad (4.12)$$

Equation 4.12 shows that they are Fourier transform pairs. This relationship is practical for identifying the phase between two signals, which represents the concurrence of the signals. This phase is found by using the parts of the PSD as shown in Eq.4.6, and applying Eq.4.13.

---

$$\phi_{xy} = \arctan\left(\frac{Qu_{xy}(f)}{Co_{xy}(f)}\right) \quad (4.13)$$

When  $\phi_{xy} = 0$ , the displacements are in the same direction. If on the other hand  $\phi_{xy} = \pi$ , the signals are perfectly phased in the opposite direction to one-another. When the signals are not in phase at frequencies corresponding to a predicted natural frequency, it is likely that the reason is presence of damping in the structure.

## 4.1.5 Application of the Fundamental Theories

### 4.1.5.1 Aliasing

An important repercussion of applying the Discrete Fourier Transforms (DFT), Eq.4.2, is that the number of sinusoid frequencies describing the signal is limited by half of the sampling frequency,  $f_T = \frac{1}{\Delta t}$ . The limiting frequency is called the Nyquist frequency,  $f_N$ . This leads to the possibility of aliasing. If data points in a signal can correspond to multiple sinusoids of different frequencies, it is important to have a high enough sampling frequency so that all of the frequencies in the signal will be present in its power spectrum. If  $f_T$  is too low, the magnitudes of the lower frequencies will erroneously show as larger in relation to other frequencies present in the signal.

### 4.1.5.2 Filtering

Even though it is important to have a high sampling frequency, so that the magnitudes of the frequencies in the spectrum are accurately characterized, this does not mean that all frequencies present in the data are of importance. Therefore, it is often of interest to remove excessive frequencies using so called band-pass filtering before analysis. This is done by applying a window function in the frequency domain, which means multiplying all frequencies of interest by one, and setting the redundant frequencies to zero. This concept is often used in the SDOF system identification methods, where the goal is to isolate frequencies that correspond to the natural frequency and mode-shape of the system as a whole.

---

### 4.1.5.3 Windowing

Filtering can also be applied in TD. Here it is often called windowing, and sets measurements at time instances that are not of interest to zero. This can, however, not be done without caution. The reason for this lies in the fundamentals of the transformation from time to frequency domain. Windowing can be understood as multiplying the signal with a function that is only defined as one in the time window of interest, and zero elsewhere. Following from the relationships of Eq.4.3, 4.7 and 4.8, the operation can be viewed as convolution in the FD. The window function is a finite function of ones, and the Fourier transform will experience what is called leakage, as it will not be represented accurately by one single frequency, see Figure 4.3. Multiple frequencies will be present, and the convolution will result in the magnitude of frequencies to be spread over the frequency range. This problem can be resolved by using window functions, like for example the Hanning window, which approximately represent only one frequency in FD. It is, however, important to rescale the transformation to avoid loss in magnitude in the represented frequencies.

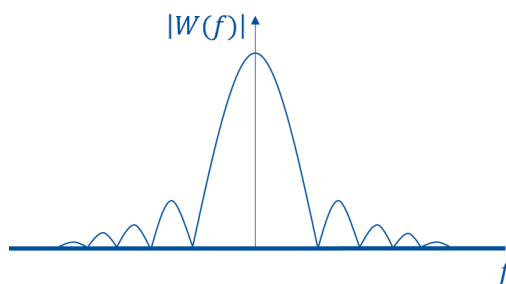


Figure 4.3: A Fourier transform of a rectangular window function

## 4.2 Singular Value Decomposition

A mathematical algorithm used in many of the OMA analysis methods is single value decomposition (SVD). It redefines a matrix as a combination of three matrices

$$\mathbf{A} = \mathbf{U}\mathbf{S}\mathbf{V}^* \quad (4.14)$$

Where the matrix  $\mathbf{S}$  is a diagonal matrix containing the non-zero real or complex singular values, or eigenvalues, of the matrix  $\mathbf{A}$ .  $\mathbf{A}$  is a  $m \times n$  real or complex matrix, and so  $\mathbf{U}$  will be

---

a  $m \times m$  real or complex matrix, and  $V^*$  will be a  $n \times n$  matrix containing the conjugate transpose or transpose of  $V$ . The  $m$  columns of  $U$  will contain the left-singular vectors of  $A$  corresponding to the  $m^{\text{th}}$  diagonal value of  $S$ , while similarly the  $n$  columns of  $V$  contain the right-singular vectors of  $A$ . The algorithm of singular value decomposition can be found in Chapter 8 of (Golub & Van Loan 1996).

---

## 4.3 Operational Modal Analysis Techniques

### 4.3.1 Time Domain Decomposition Method

The TDD method is a simple system identification technique that relies on reducing the system to a SDOF system before identifying the natural frequencies, damping and participation factors. The reduction of the system is done by filtering the data around peaks in the spectral densities of the output. As a result, the method requires that the modes are excited to an extent so that they can be identified as peaks in the PSD. But if the modes are adequately identifiable, the method has the advantage of requiring less computational effort than similar methods like the frequency domain decomposition method (FDD) (Kim et al. 2005).

#### 4.3.1.1 The Process

The first step in the TDD method is to identify the peaks of the PSD signal. The PSD can be found using direct Fourier transforms of the correlation functions, or by Welch procedure, resulting in smoothed densities. The Welch procedure is less computationally demanding (Rainieri et al. 2014). The example PSD shown in Figure 4.4 is averaged in segments of 500 elements, overlapping by 50.

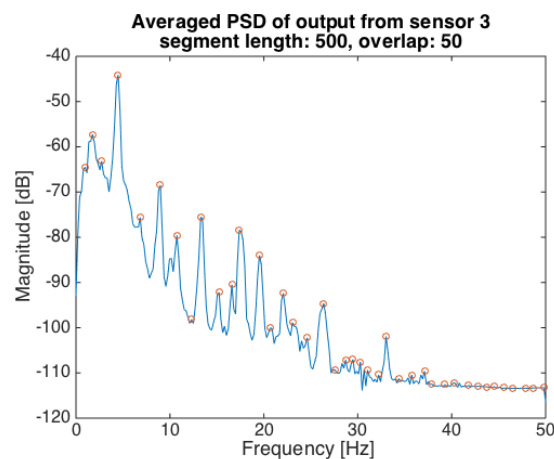


Figure 4.4: Example PSD from a sensor of the experimental data presented in Chapter 5.

After identifying the frequencies of the peaks, band-pass filters have to be designed to filter out all other frequencies that are not part of the peaks. The article that first proposed this method uses a third order Butterworth filter for this process (Kim et al. 2005), and the fit of this filter is vital for the accuracy of the results.



---

Using the assumption that the total displacement can be decomposed into modal participations, as in Equation 3.7 of Section 3.1, the filtered signal can be written as

$$\{y_i(k)\} = \{c_i(k)\}\{\phi_i\} + \{\varepsilon_f(k)\} \quad (4.15)$$

where  $k$  denotes the discrete time instance,  $y_i$  is the filtered response of peak  $i$ ,  $c_i$  is the modal participation,  $\phi_i$  is the mode shape corresponding to mode  $i$ .  $\varepsilon_f$  is the error of this mode resulting from noise or the accuracy of the band-pass filtering, and which can also be decomposed into a sum of shapes and contributions in time,  $\psi_j$  and  $d_j$  respectively.

When the filtered time-series is ready, the cross-correlation matrix of the signals from all of the sensors is calculated, resulting in what the literature calls the energy matrix. Here,  $Y_i$  is the  $N \times p$  matrix of  $p$  discrete time instances and  $N$  sensors.

$$[E] = [Y_i][Y_i]^T = \begin{bmatrix} R_{1,1} & \cdots & R_{1,N} \\ \vdots & \ddots & \vdots \\ R_{N,1} & \cdots & R_{N,N} \end{bmatrix} \quad (4.16)$$

Applying the assumptions of Equation 4.15 to the energy matrix, results in Equation 4.17.

$$\begin{aligned} [E] &= \{\phi_i\}\{c_i\}^T\{c_i\}\{\phi_i\}^T + \{\phi_i\}\{c_i\}^T \sum_{j=1}^{p-1} \{d_j\}\{\psi_j\}^T \\ &+ \sum_{j=1}^{p-1} \{\psi_j\}\{d_j\}^T\{c_i\}\{\phi_i\}^T + \sum_{j=1}^{p-1} \sum_{k=1}^{p-1} \{\psi_j\}\{d_j\}^T\{d_k\}\{\psi_k\}^T \quad (4.17) \\ [E] &= \{\phi_i\}q_i\{\phi_i\}^T + \sum_{j=1}^{p-1} \{\psi_j\}\sigma_j\{\psi_j\}^T \end{aligned}$$

Here,  $q_i$  and  $\sigma_j$  denote the scalar representing the physical energy at the modes. Now, using 4.17,  $E$  can be written as

$$[E] = [A][\Omega][A]^T \quad (4.18)$$

Solving Equation 4.18 for  $[A]$  and  $[\Omega]$  requires applying an SVD process, as presented in Section 4.2. The resulting matrix  $[A]$  will contain the mode-shape of the mode in the first

---

column, and the mode-shapes of the noise in the other columns.  $\Omega$  contains the energy of the  $i^{th}$  identified mode,  $q_i$ , in the first number on the diagonal, and the remaining numbers on the diagonal represent the energy of the noise,  $\sigma_j$ . If the identified peak represents an actual mode,  $q_i \gg \sigma_1 > \sigma_2 > \dots > \sigma_{p-1}$ , and in noise free data, all the sigma values should be zero.

The next step in the process of TDD is to identify the natural frequencies and damping based on the identified mode shapes, and the modal contributions, which can be calculated based on Equation 4.15 using Equation 4.19.

$$\{c_i\}^T = \frac{1}{\{\phi_i\}^T \{\phi_i\}} \{\phi_i\}^T [Y_i] \quad (4.19)$$

This modal participation is now assumed noise free, as Equation 4.19 extracts the time-series of the identified mode shape only. Kim and his team recommend that the damping and natural frequencies are extracted from the spectrum of the participation using either peak-picking or the half-bandwidth method, or by use of ERADC (Kim et al.). In (Fang 2013) the author has chosen to use the half-power bandwidth method. However, this method has shown to have large errors (Rainieri et al. 2014), so the method proposed for this thesis is based on the framework presented in (Brincker et al. 2001).

Utilizing the fact that

$$[R_{yy}(\tau)] = [\Phi][R_{pp}(\tau)][\Phi]^T \quad (4.20)$$

where  $R_{yy}(\tau)$  is the auto-correlation of the out-put time-series and  $R_{pp}(\tau)$  is the auto-correlation of the modal participation. The auto-correlation function of the modal participation time-series, which is also called the free decay time domain function, is found first for all time lags. The damped natural frequencies can then be found by extracting the period of the zero-up-crossings of this function. Then, the peaks of the function are identified, and the damping is found by the logarithmic decrement of the peaks. By writing the decrement on the form shown in Equation 4.21, the decrement can be found by identifying the slope of a linear regression of the first points of the function.

$$k\delta_k = \ln\left(\frac{r_0}{r_k}\right) \quad (4.21)$$

$$\xi = \frac{\delta}{\sqrt{\delta^2 + 4\pi^2}} \quad (4.22)$$

where

|            |                                |
|------------|--------------------------------|
| $\delta_k$ | The logarithmic decrement      |
| $k$        | Peak number                    |
| $r_0$      | Magnitude of the first peak    |
| $r_k$      | Magnitude of the $k^{th}$ peak |
| $\xi$      | Damping ratio                  |

### 4.3.2 The Macec Methods

#### 4.3.2.1 The Poly-Reference Least Squares Complex Frequency Method

As a consequence of some limitations found in the original Least Squares Complex Frequency method (LSCF) in prediction of closely spaced modes and other conversion problems, the Poly-reference Least Squares Complex Frequency method (p-LSCF) was presented in 2003 by (Guillaume et al. 2003). This method is a frequency domain method, see Section 3.1.3, utilizing the fact that the Fourier transform of a time-series has poles in all four quadrants of the complex plane, so that the FRF can be written as

$$\begin{aligned} [H(\omega)] &= \sum_{r=1}^{N_m} \frac{[R_r]}{i\omega - \lambda_r} + \frac{[R_r^*]}{i\omega - \lambda_r^*} \\ &= \sum_{r=1}^{N_m} \frac{Q_r \{\phi_r\} \{\phi_r\}^T}{i\omega - \lambda_r} + \frac{Q_r^* \{\phi_r\}^* \{\phi_r\}^{*T}}{i\omega - \lambda_r^*} \end{aligned} \quad (4.23)$$

where

|  |   |
|--|---|
| $N_m$                                  | The number of modes   |
| $\{\phi_r\}$                           | The mode-shape corresponding to mode r  |
| $[R_r]$                                | The residue matrix  |
| $Q_r$                                  | Holds information about the modal scaling factor  |
| $\lambda_r = \sigma_r + i\omega_{d,r}$ | The pole of the $r^{th}$ mode holding information about the damped frequency and ratio of damping |

Continuing, the FRF is also written on a Matrix Fraction Description (MFD), which is a ratio of two matrix polynomials, the numerator polynomial and the common-denominator polynomial.

$$[H(\omega)] = \frac{[B(\omega)]}{A(\omega)} = \frac{\sum_{j=0}^n [\beta_j(\omega)] \Omega^j(\omega)}{\sum_{j=0}^n \alpha_j \Omega^j(\omega)} \quad (4.24)$$

where

|  |  |
|--|--|
| $[\beta_j(\omega)]$                              | Unknown matrix of complex parameters to be estimated |
| $\alpha_j$                                       | Unknown complex parameters to be estimated           |
| $\Omega_f^j = e^{(i\omega_f \Delta t)j} = z_f^j$ | Complex polynomial basis function                    |
| $n = 2N_m/N_c$                                   | Order of the polynomial                              |
| $N_c$  | Number of sensors                                    |

Then, by considering that

$$[S_{yy}(\omega)] = [H(\omega)]^* [S_{FF}(\omega)] [H(\omega)]^T \quad (4.25)$$

the positive PSD for any out-put sensors, o, can be written as

$$[G_{YY}(\omega_f)] = \frac{\sum_{j=0}^n [B_{o,j}] \Omega_f^j}{\sum_{j=0}^n [A_j] \Omega_f^j} = [B_o(\Omega_f, [\theta])] [A(\Omega_f, [\theta])]^{-1} \quad (4.26)$$

where

|                    |  |
|--------------------|--|
| $[B_{o,j}], [A_j]$ | Unknown complex parameters to be estimated                           |
| $[\theta]$         | A vector of all the unknown complex parameters of $[B_{o,j}], [A_j]$ |
| $\Omega_f^j$       | Generalized transform variable                                       |

The least squares formulation is a result of minimizing the error  $[E_o(\omega_f, \theta)]$  of the predicted cross-power spectrums of Equation 4.26 to the measured power spectrums

$$[E_o(\omega_f, \theta)] = [B_o(\Omega_f, [\theta])] - [\hat{G}_o(\omega_f)] [A(\Omega_f, [\theta])] \quad (4.27)$$

---

where

$[\hat{G}_o(\omega_f)]$  Measured Power Spectrum

This is done by minimizing the cost-function of Equation 4.28.

$$\ell([\theta]) = \sum_{o=1}^{N_c} \sum_{f=1}^{N_f} tr([E_o(\omega_f, \theta)]^H [E_o(\omega_f, \theta)]) \quad (4.28)$$

where

$tr(\cdot) = E[(\cdot)]$  Trace, the sum of diagonal components of  $(\cdot)$

$\ell([\theta])$  Cost function of variables  $[\theta]$

Minimizing 4.28 requires expressing  $\ell([\theta])$  in terms of a Jacobian matrix J so that

$$[J]\{\theta\} \approx 0 \quad (4.29)$$

This process is further explained in (Guillaume et al. 2003). The solutions of polynomials are sorted in what are called stabilization diagrams, with examples given in Chapter 5, where only the imaginary solutions are considered stable. One of the main reasons why the p-LSCF has become very popular is that the stabilization diagrams have very distinct stable poles, and the method is therefore considered valuable for automation purposes.

After the unknown parameters,  $\theta$ , are estimated, the natural frequencies are found by transforming the  $z_f^j$  solutions back to TD by

$$z_r = e^{\lambda_r \Delta t} \rightarrow \lambda_r = \frac{\ln(z_r)}{\Delta t} \quad (4.30)$$

$$f_r = \frac{|\lambda_r|}{2\pi} \quad (4.31)$$

$$\xi_r = \frac{Re(\lambda_r)}{|\lambda_r|} \quad (4.32)$$

---

4.3.2.2 Stochastic Subspace Identification

The Stochastic Subspace Identification methods (SSI) are considered parametric TD methods. They aim to identify the stochastic state-space model from out-put data only. The state-space relation is a result of the reduction of order of the equation of motion using state vectors

$$\{s(t)\} = \begin{bmatrix} \{\dot{y}(t)\} \\ \{y(t)\} \end{bmatrix} \quad (4.33)$$

Resulting in a state-equation on the form

$$\{\dot{s}(t)\} = \underbrace{\begin{bmatrix} -[M]^{-1}[C] & -[M]^{-1}[K] \\ [I] & [0] \end{bmatrix}}_{[A_c]} \{s(t)\} + \underbrace{\begin{bmatrix} [M]^{-1}\{\bar{B}\} \\ 0 \end{bmatrix}}_{[B_c]} \{f(t)\} \quad (4.34)$$

where  $\{\bar{B}\}$  is a vector containing the force locations.

The resulting observation equation is written as

$$\begin{aligned} \{y(t)\} &= [C_c]\{s(t)\} + [D_c]\{f(t)\} \\ [C_c] &= [[C_v] - [C_a][M]^{-1}[C] \quad [C_d] - [C_a][M]^{-1}[K]] \\ [D_c] &= [C_a][M]^{-1}\{\bar{B}\} \end{aligned} \quad (4.35)$$

where

$C_a, C_v, C_d$  Output location matrices for accelerometers, velocimeters and displacement transducers respectively

Since the input is not known in stochastic subspace methods, the discrete versions of Equations 4.33 and 4.34 reduce to the Equations of 4.36.

$$\begin{aligned} \{s_{k+1}\} &= [A]\{s_k\} + \{w_k\} \\ \{y_k\} &= [C]\{s_k\} + \{v_k\} \end{aligned} \quad (4.36)$$

---

where  $\{w_k\}$  and  $\{v_k\}$  are vectors containing noise, which is assumed to be a zero-mean Gaussian, stationary white noise process. The covariance of the noise for two arbitrary time instances  $p$  and  $q$  is given by

$$E \left[ \begin{Bmatrix} \{w_p\} \\ \{v_p\} \end{Bmatrix} \begin{Bmatrix} \{w_q\}^T \\ \{v_q\}^T \end{Bmatrix} \right] = \begin{cases} \begin{bmatrix} [Q^{ww}] & [S^{wv}] \\ [S^{wv}]^T & [R^{vv}] \end{bmatrix}, & p = q \\ [0], & p \neq q \end{cases} \quad (4.37)$$

And

$$\begin{aligned} [A] &= e^{[A_c]\Delta t} \\ [C] &= [C_c] \end{aligned} \quad (4.38)$$

Determining  $[Q^{ww}]$ ,  $[S^{wv}]$  and  $[R^{vv}]$  is part of the system identification process of SSI, and this premise of white noise loading is the fundamental part of the proof of the method. A number of manipulations of the state-equations lead to the fundamental relations for Equation 4.39.

$$\begin{aligned} [\Sigma] &= [A][\Sigma][A]^T + [Q^{ww}] = E[\{s_k\}\{s_k\}^T] \\ [R_0] &= [C][\Sigma][C]^T + [R^{vv}] \\ [G] &= [A][\Sigma][C]^T + [S^{wv}] = E[\{s_{k+1}\}\{y_k\}^T] \\ [R_i] &= [C][A]^{i-1}[G] \end{aligned} \quad (4.39)$$

Here,  $[G]$  is known as the one-step ahead covariance matrix. This is practical, as the output covariance matrix,  $[R_i]$ , is found directly from the output data. So, the one-step ahead vector can be found by decomposing  $[R_i]$ , making the prediction of the state-space matrix possible. Therefore, an optimal predictor can be found by minimizing the error between the predicted and actual measured response, assuming that the predicted response is in the form

$$\{y_k\} = [C]\{s_k\} \quad (4.40)$$

This is done by the introduction of Kalman-filters and the Ricatti equation, which are explained in Section 4.2.2 of (Rainieri et al. 2014). When the error is minimized, the equations are solved

---

for  $[A]$ , and as for the p-LSCF method, the natural frequencies and damping ratios are found by use of Equations 4.30 and 4.31.

Two predictor formulations are based on solving for the state-equations presented above, the covariance-driven SSI (Cov-SSI) and the data-driven SSI (DD-SSI) methods. The derivations of these two methods can be found in the referenced literature.

### 4.3.3 Processing of Mode-Shape and Natural Frequency Estimates

After the modes and mode-shapes have been estimated by means of the methods presented above, they have to be compared in some sort of way. As the exact solutions are not known, the comparison will not be in terms of accuracy, but rather by terms of precision. A critical factor in the effectiveness of the comparisons of results is the correct pairing of modes. This is mainly done manually by observations of the mode shapes. A major concern with manual pairing of modes by mode shape observations is the possible presence of spatial aliasing due to insufficient sensor positioning (Ewins 2000).

Natural frequencies are simply compared by their relative scatter in percent by Equation 4.41, where (1) and (2) are two arbitrary techniques of obtaining the frequencies. The methods are either numerical, analytical or experimental, but the comparison between numerical models and experimental results is principally of interest only if the experimental results are in good agreement with each other.

$$\Delta f = \frac{f_{(2),n} - f_{(1),n}}{f_{(1),n}} \cdot 100 \quad (4.41)$$

Similarly, the mode-shapes are compared in terms of the degree of linearity between two mode-shapes, also known as MAC-values, shown in Equation 4.42.

$$MAC \left( \left\{ \phi_n^{(1)} \right\}, \left\{ \phi_n^{(2)} \right\} \right) = \frac{\left| \left\{ \phi_n^{(1)} \right\}^H \left\{ \phi_n^{(2)} \right\} \right|^2}{\left( \left\{ \phi_n^{(1)} \right\}^H \left\{ \phi_n^{(1)} \right\} \right) \left( \left\{ \phi_n^{(2)} \right\}^H \left\{ \phi_n^{(2)} \right\} \right)} \quad (4.42)$$

The calculated complex mode-shapes are first plotted in the imaginary plane. This allows for analyzing the phase of the modes. When the phases are within  $\pm 10^\circ$  of either  $0^\circ$  or  $180^\circ$ , the phases are considered adequately small so that the modes can be interpreted by the real part of



---

the modes alone, Section 4.8.1 of (Rainieri et al. 2014). Otherwise, the mode shapes must be interpreted by use of Equation 3.18.

Other measures of how close the modes are to being normal (real) modes are the mean phase deviations (MPD) and the modal phase collinearity (MPC). For normal modes, the MPC value should be one, while the MPD should be zero.



---

# Chapter 5

## Case Study

This chapter presents a case study to illustrate, discuss and compare the different methods described in Chapters 3 and 4. Experimental data of a SCR model subjected to VIV is used to define the case study.

### 5.1 Description of the Experiment

The experimental data used for the case study of this thesis originates from a test project that was part of the joint industry project STRIDE Phase 4, administrated by 2H Offshore Engineering Ltd and subcontracted to MARINTEK. The experimental tests were carried out during the course of 2001, and a summary of the results was presented in the report by Halvor Lie (Lie 2001). Main objectives of the tests were

- To study VIV for a generic catenary riser configuration subject to various current velocities, with a varying incident angle between the riser and the current flow.
- To create input data for fundamental studies of VIV and improvements of theoretical models.

#### 5.1.1 The Test Facility

The test facility used for the towing of the SCR model was Towing Tank No.III at MARINTEK, with an overview shown in Figure 5.1.

The dimensions of the towing tank are given in Table 5.1. The SCR was towed by a towing carriage with a constant speed that could be adjusted to reach the desired uniform current speed.

*Table 5.1: Dimensions of MARINTEK Towing Tank No.3*

| Length (m) | Breadth (m) | Depth (m) |
|------------|-------------|-----------|
| 80         | 10.5        | 10        |

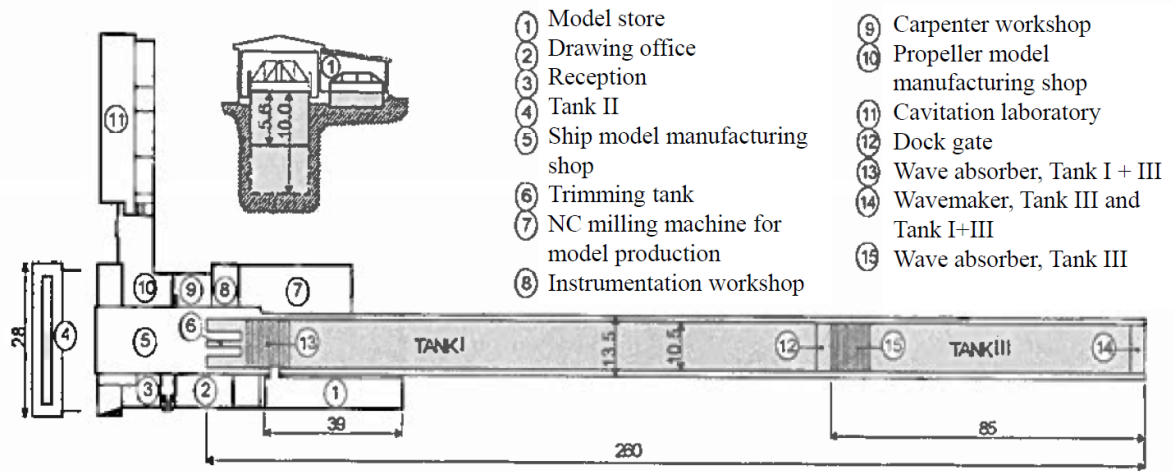


Figure 5.1: Overview of the MARINTEK test facility (Lie 2001).

### 5.1.2 The Experimental Setup

Figures 5.2 and 5.3 present the experimental setup of the catenary in the MARINTEK tank. The top of the brass catenary was attached to a horizontal beam, while the lower end was attached to a truss-structure.

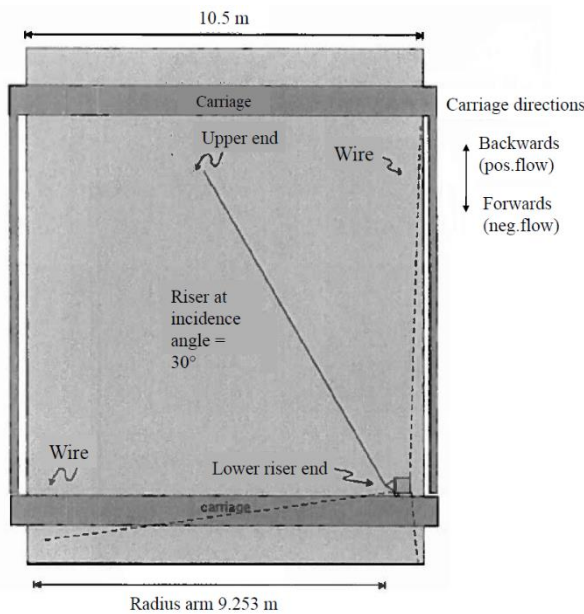


Figure 5.2: View of catenary setup from above (Lie 2001).

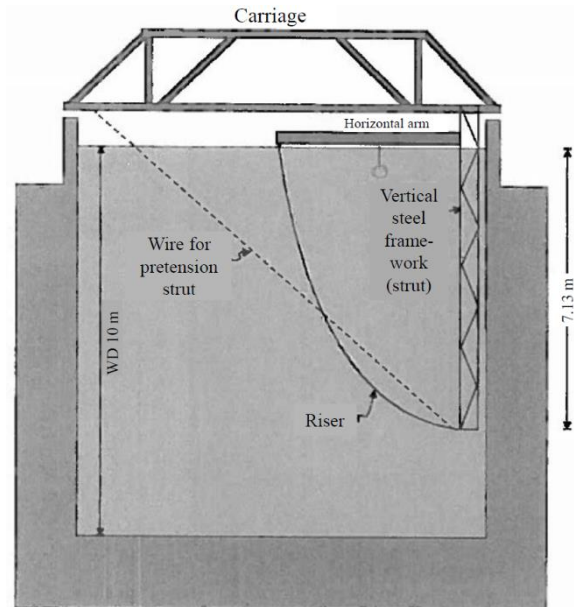


Figure 5.3: Vertical setup of catenary (Lie 2001).

In order to reduce vibration loading on the horizontal arm, the upper riser end was mechanically isolated from the carriage by applying a 50 kg mass near the riser end, connecting the arm end to the carriage by thin, pre-tensioned wires. The lower end of the truss-frame was also pre-tensioned to the carriage using thin wires.

### 5.1.3 The Catenary Riser Model

With a length to diameter ratio of about 890, the model riser is not representative of typical installed risers offshore, but is still sufficient for the comparison of numerically calculated modes to experimentally estimated ones. The catenary outer diameter was 14 mm, and it had a length of 12.5 meters. Additional model characteristics are given in Table 5.2.

*Table 5.2: Catenary properties used as input for static configurations and modal calculations (Lie 2001).*

|   |  |
|---|--|
| Total length between pinned ends  | 12.5 m   |
| Mass per unit length including content                                    | 0.357 kg/m   |
| Outer diameter  | 14 mm  |
| Wall thickness of riser   | 0.45 mm  |
| Density of brass  | 8980 kg/m <sup>3</sup> (nominal)                   |
| Youngs modulus for brass  | 1.05 · 10 <sup>11</sup> N/m <sup>2</sup> (nominal) |
| Axial stiffness, EA   | 2.01 · 10 <sup>6</sup> N (nominal)                 |
| Bending stiffness, EI   | 46.2 Nm <sup>2</sup> (nominal)                     |
| Percent relative damping in air, $\xi$                                    | 0.2-0.6 (measured)                                 |
| Horizontal distance between riser ends                                    | 9.253 m  |
| Vertical distance between riser ends                                      | 7.130 m  |
| Vertical height of upper end fixture (rotating point) above water surface | 0.050 m  |
| Tension, upper end  | 22.55 N (Calculated by RIFLEX)                     |
| Tension, lower end  | 8.44 N (Calculated by RIFLEX)                      |
| Angle from vertical, upper end  | 26 degrees (Calculated by RIFLEX)                  |
| Angle from vertical, lower end  | 88 degrees (Calculated by RIFLEX)                  |

Force transducers were used to weigh the total structure in air, and this gave the resulting mass per unit length including content. Structural damping estimates were found using free-decay tests in air.

As the brass tube used as the catenary could not be delivered in its full length, separate pieces of 5 meters were joined together by hard soldering sleeves of 20 mm length. These sleeves had an outer diameter of about 18 mm, and were located at 4.042 and 8.396 meters from the lower end. The same type of sleeve was used to house the accelerometers, as shown in Figure 5.4. Locations of the accelerometers are found in Table.5.3.

*Table 5.3: Accelerometer locations (Lie 2001).*

| Accelerometer | Distance from lower end (m) |
|---------------|-----------------------------|
| 1             | 1.137                       |
| 2             | 2.272                       |
| 3             | 3.408                       |
| 4             | 4.544                       |
| 5             | 5.682                       |
| 6             | 6.817                       |
| 7             | 7.953                       |
| 8             | 9.090                       |
| 9             | 10.224                      |
| 10            | 11.364                      |
| Upper joint   | 12.500                      |

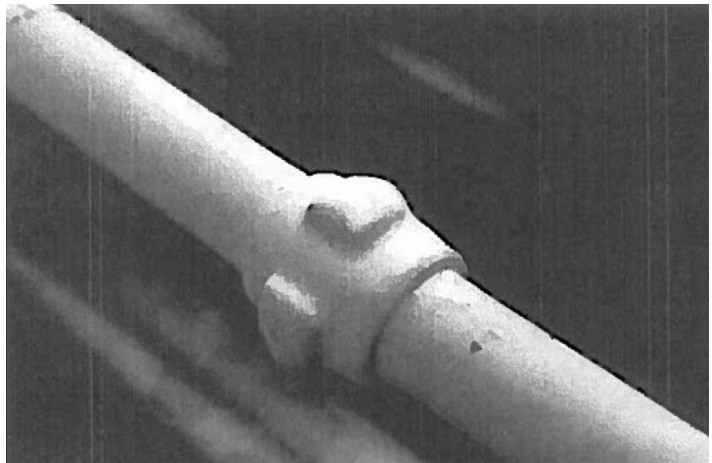


*Figure 5.4: Accelerometers with casing (Lie 2001).*

The accelerometers were placed in pairs normal to the longitudinal axis and perpendicular to each other. The cables from each pair were threaded through holes in the catenary, and passed through the pipe. To avoid differences in masses, dummy cables were used so that the amount of cable throughout the pipe was the same, and it was assumed that the sleeves solved the problem of local differences in axial and bending stiffness resulting from the cable holes. Accelerometer pair no. 7 failed during the experiments, so results from this sensor are not

included in this thesis. However, it was assumed that 6-8 pairs of accelerometers would be sufficient to serve the scope of the experiment.

The surface roughness of the catenary model was not documented during the experimental campaign. However, the surface was painted to enhance visibility in the recorded video images, and thus the surface is assumed rather smooth. The straightness of the model was measured in air, with a maximum deviation of about 2/3 of the catenary diameter.

Before carrying out the experiment, natural frequencies for the first 10 modes were found using string, beam and frame theory. Based on the natural frequencies of the frame FEM, the velocities that are expected to excite the various frequencies were calculated, using a Strouhal number of 0.2. The results from the preliminary calculations are found in Table 5.4. The excitation velocities to the right in this table show that the modes that are most likely to be present in the signals are modes 4-6, as these velocities lie within the applied towing velocities, presented in Section 5.1.5.

*Table 5.4: Preliminary calculations of natural frequencies and excitation velocities (Lie 2001).*

| Mode number | String (Hz) | Beam (Hz) | Frame (Hz) | $U = \frac{\omega_{frame} D}{2\pi St}$ (m/s) |
|-------------|-------------|-----------|------------|--|
| 1           | 0.282       | 0.099     | 0.299      | 0.021  |
| 2           | 0.563       | 0.397     | 0.690      | 0.048  |
| 3           | 0.845       | 0.893     | 1.230      | 0.086  |
| 4           | 1.127       | 1.588     | 1.947      | 0.136  |
| 5           | 1.410       | 2.481     | 2.853      | 0.200  |
| 6           | 1.692       | 3.573     | 3.953      | 0.247  |
| 7           | 1.974       | 4.863     | 5.248      | 0.367  |
| 8           | 2.255       | 6.351     | 6.740      | 0.472  |
| 9           | 2.537       | 8.039     | 8.429      | 0.590  |
| 10          | 2.819       | 9.924     | 10.317     | 0.722  |

### 5.1.4 The Coordinate Systems

Three different right handed Cartesian coordinate systems were used for the presentation of results from the experiment.

- One system is the global, assumed inertial coordinate system,  $x, y$  and  $z$ . As shown in Figure 5.5,  $y$  is the axis pointing in the towing direction of the pool and  $x$  points in the breadth direction.
- The second system is the local catenary coordinate system,  $x_r, y_r$  and  $z_r$ , with  $x_r$  and  $z_r$  denoting the catenary plane, and  $y_r$  going out of the catenary plane.
- The last coordinate system is the riser cross-section coordinate system,  $x_c, y_c$  and  $z_c$ .  $x_c$  is in the catenary plane, and  $y_c$  is orthogonal to the catenary plane, both aligned with an accelerometer pair.  $z_c$  is tangential to the riser cross-section midpoint angle with the horizontal plane.

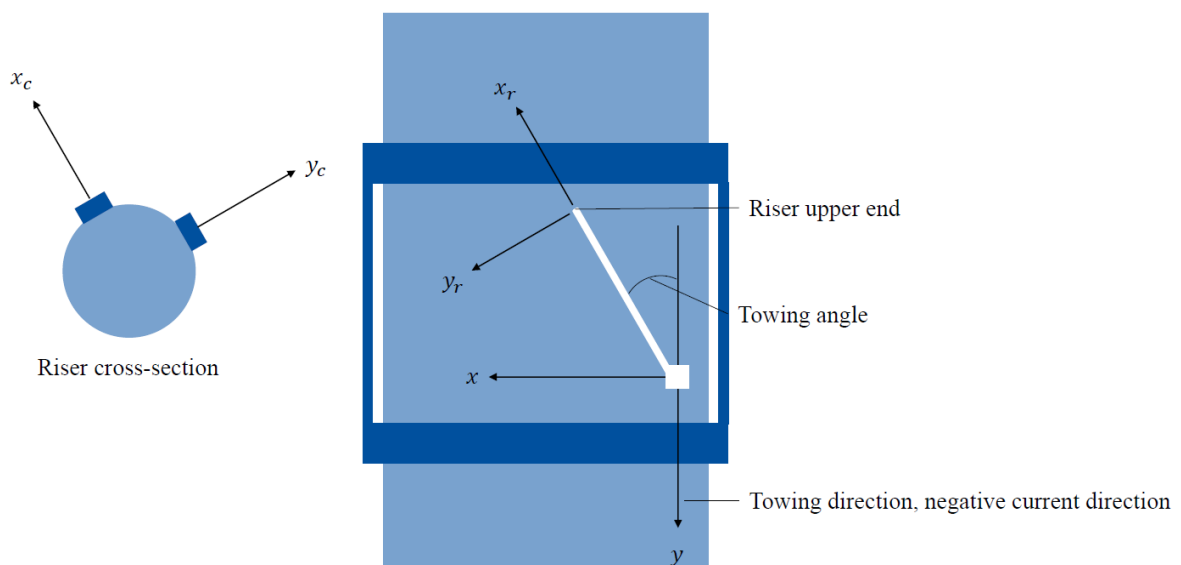


Figure 5.5: Coordinate systems used for experimental work and results, modified image from (Lie, 2001).



---

### 5.1.5 The Test Program

The catenary model was towed at velocities ranging from 0.12 to 0.34 m/s at 0.02 m/s steps. These towing velocities represent uniform currents of the same magnitudes.

During the test, the angles of inclination were varied from 0 to 90 degrees at 30-degree intervals. The duration of each run depends on the towing velocity, and is limited by the pool length. Average run durations were about 2 minutes.

Lie (2001) commented on the influence of the towing carriage on the 0° towing angle data series, as it was found that the wake effects behind the carriage could reduce the experienced current velocities to about a factor of 0.8 or 0.9 of the reference speeds.

Displacement time-series from the experiment are obtained by integrating the acceleration measurements twice in the frequency domain. Other measurements, like the catenary end forces and the test rig accelerations are not considered in the following case study.

## 5.2 Experimental results and discussion

Before continuing on to system identification and numerical analysis in the case study of this thesis, the data set itself is studied and discussed in the following text. The displacement results from both IL and CF directions obtained from the perpendicular sensors at location 5 are plotted in Figures 5.6 and 5.7. As is expected, the displacements are larger for the CF direction for both velocities, and the larger velocity results in larger displacements.

Also notice the transient state at the beginning of each time-series, in the carriage acceleration phase, where the displacement magnitudes are larger for both current velocities. This will affect the displacement envelopes of the raw-data series, and may erroneously affect observations that are linked to the various current speeds. (Niedzwecki & Moe 2007) discusses the effect of removing this transient phase when studying the resulting PSDs. In this thesis, to avoid possible noise resulting from these effects, the first twenty seconds of the time-series are removed from the analysis. This has consequences on the remaining time-series length, but should give a better representation of the responses resulting from the specific current velocities under investigation.

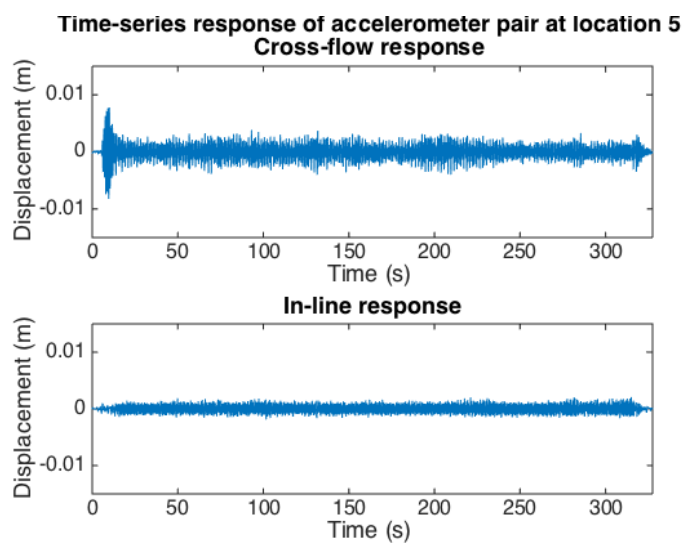


Figure 5.6: Displacement time-series from sensor 5 at 0.12 m/s current velocity.

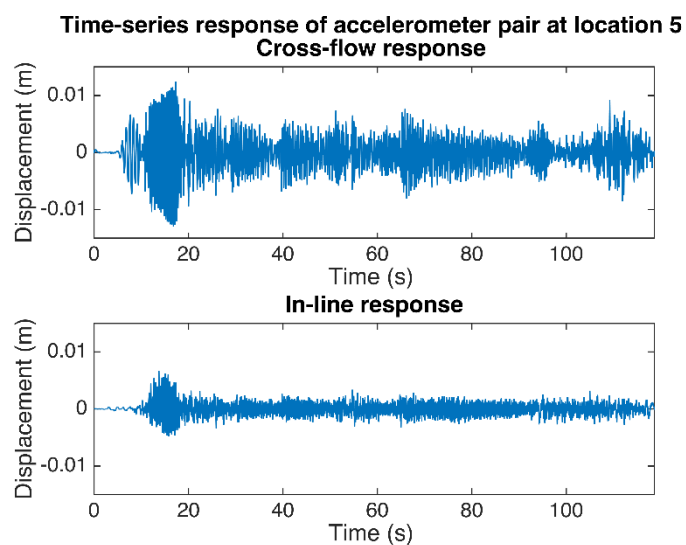


Figure 5.7: Displacement time-series from sensor 5 at 0.34 m/s current velocity

The PSDs calculated by a Welch-procedure using a Matlab function with two non-overlapping segments of the displacements measured at sensor 5 in the CF direction are shown below, in Figures 5.8 and 5.9.

For both velocities, the largest peaks are concentrated about a relatively narrow band of frequencies, mainly in the range from 0-5 Hz. Comparing this observation with the calculated modal excitation velocities shown in Table 5.4, the largest peaks seem to match relatively well with the calculations in the preliminary work. The peaks are gathered around 1-2 Hz for the 0.12 m/s flow speed, and the largest observed peak for 0.34 m/s flow speed is at about 4-5 Hz.

Based on Table 5.4, frequencies higher than that of the seventh mode are not likely occur. Although they are of magnitudes much smaller than in the 0-5 Hz range, there are peaks present above this mode. However, as they were not considered likely in the planning of the experiment, the accelerometer spacing and number limits the identification of possible mode shapes corresponding to these potential natural frequencies. Nonetheless, as the magnitudes of the peaks are relatively small, it is likely that they are due to measurement noise, such as vibrations from the carriage or sensor flaws.

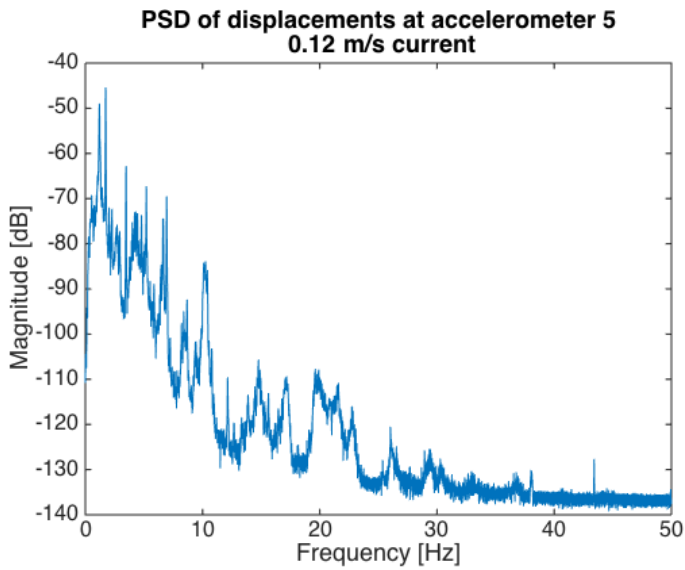


Figure 5.8. PSD of displacements measured at accelerometer 5 in the cross-flow direction, with a 0.12 m/s flow velocity.

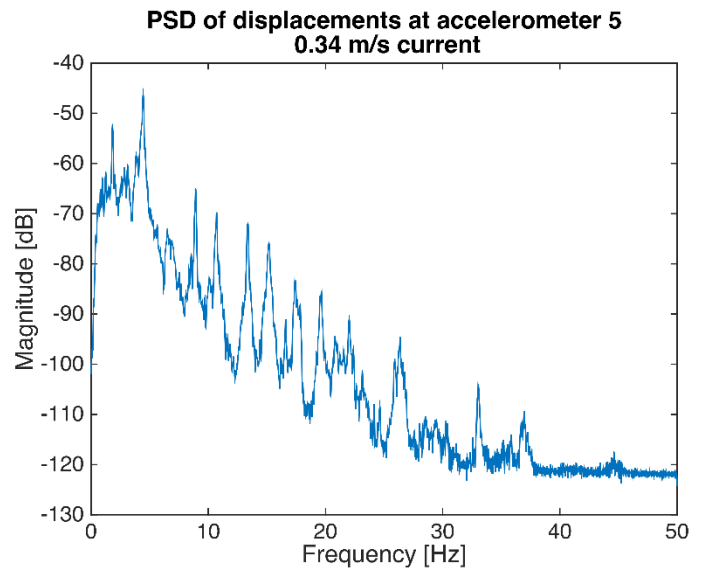


Figure 5.9. PSD of displacements measured at accelerometer 5 in the cross-flow direction, with a 0.34 m/s flow velocity.

Displacement envelopes of the truncated time-series are shown in Figures 5.10 and 5.11. The envelopes show the maximums and minimums at each of the accelerometer locations over the whole time-series, which do not necessarily occur simultaneously. For this thesis, the displacement extremes at accelerometer seven are estimated by linear interpolation between accelerometers six and eight.

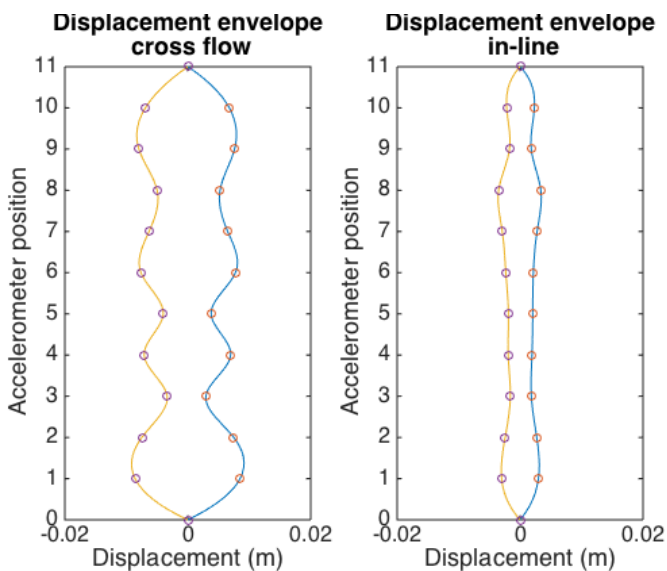


Figure 5.10: Displacement envelopes of the 0.12 m/s current flow velocity.

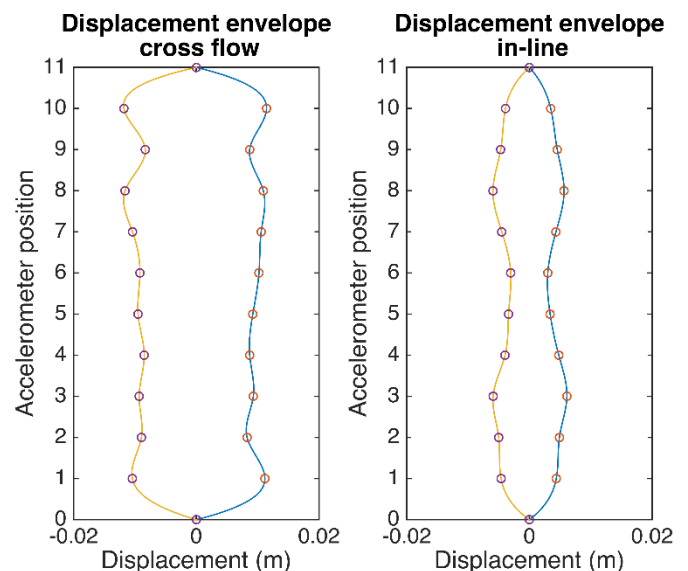


Figure 5.11: Displacement envelopes of the 0.34 m/s current flow velocity.

Notice that there are larger differences between nodes for the 0.12 m/s current flow than for the 0.34 m/s flow. This could be a result of the fact that there are more active modes for the higher velocity case, so if an accelerometer location is a nodal point for one mode shape, it could still have large displacements resulting from other active modes.

### 5.2.1 Case Study

As the CF displacement cases are of most interest for the scope of this thesis, the experimental data from the 90 degree towing angle is used. For this towing angle, the measurements from the accelerometer placed in the  $x_c$  direction will be in the riser plane.

*Table 5.5: Towing results selected for the Case Study.*

| Current velocities<br>(m/s) | Towing angle |       |            |       |
|-----------------------------|--------------|-------|------------|-------|
|                             | 0 degrees    |       | 90 degrees |       |
|                             | $x_c$        | $y_c$ | $x_c$      | $y_c$ |
| 0.12                        |              |       | X          |       |
| 0.24                        |              |       | X          |       |
| 0.34                        |              |       | X          |       |

OMA methods adopted for the case study are the TDD method, the p-LSCF method, the Cov-SSI method and the DD-SSI methods.

To investigate the similarities between the experimental results and the numerical models discussed in Section 3.3, the model characteristics of Table 5.2 are used as input in the static and dynamic analysis. Table 5.6 compares the eigenvalues obtained using the FEM solutions to dynamic analysis to those obtained using the WKB method by use of Eq.4.41. Figure 5.12 presents the correlations in terms of MAC values of the mode shapes resulting from FEM and WKB. The correlations on the diagonal represent the MAC values calculated from mode shape  $\phi_i$  of FEM and mode shape  $\phi_j$  of WKB, when the mode numbers  $i = j$ . These correlations should be as close to one as possible, and a value of one indicates perfect unity. The correlations off the diagonal are MAC values of mode shape  $\phi_i$  and  $\phi_j$ , when  $i \neq j$ . These correlations are expected to be as close to zero as possible, indicating that the calculated mode shapes are independent of mode shapes corresponding to other modes. As can be seen from Table 5.6 and

Figure 5.12, the solutions are relatively similar. The deviations in eigenfrequencies are relatively small. Also, the diagonal of Figure 5.12 are all equal to one, while the values off the diagonal are close to zero for all modes, indicating that the calculated mode shapes are similar. Therefore, when comparing results from experimentally obtained modes and mode shapes with the FEM method's results, it is assumed that the conclusions drawn would also be applicable to a similar comparison to the WKB method solutions.

Table 5.6: Eigenvalue comparison of FEM solutions relative to the WKB method solutions

| Mode no.                | 1     | 2     | 3     | 4     | 5     | 6     | 7     | 8     | 9     | 10    |
|-------------------------|-------|-------|-------|-------|-------|-------|-------|-------|-------|-------|
| Eigenvalue deviation[%] | -4.33 | -4.18 | -2.77 | -1.78 | -1.16 | -0.77 | -0.50 | -0.32 | -0.19 | -0.10 |

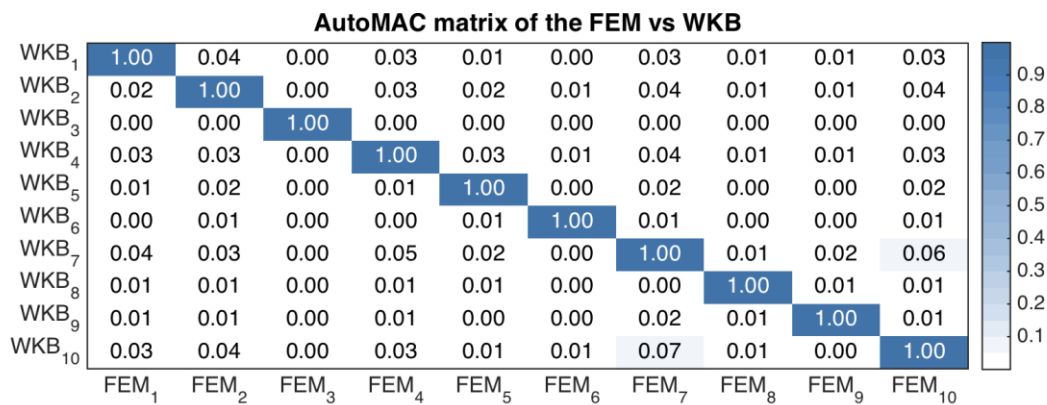


Figure 5.12: AutoMAC comparison of the WKB mode shapes relative to the FEM method mode shapes

### 5.3 Application of the Time Domain Decomposition method

The TDD method is implemented, following the discussion from Section 4.3.1, with the algorithm flow chart shown in Figure 5.13. Un-damped frequencies and damping are found from auto-correlations of the modal participation factor using the logarithmic decrement technique presented in Section 4.3.1.

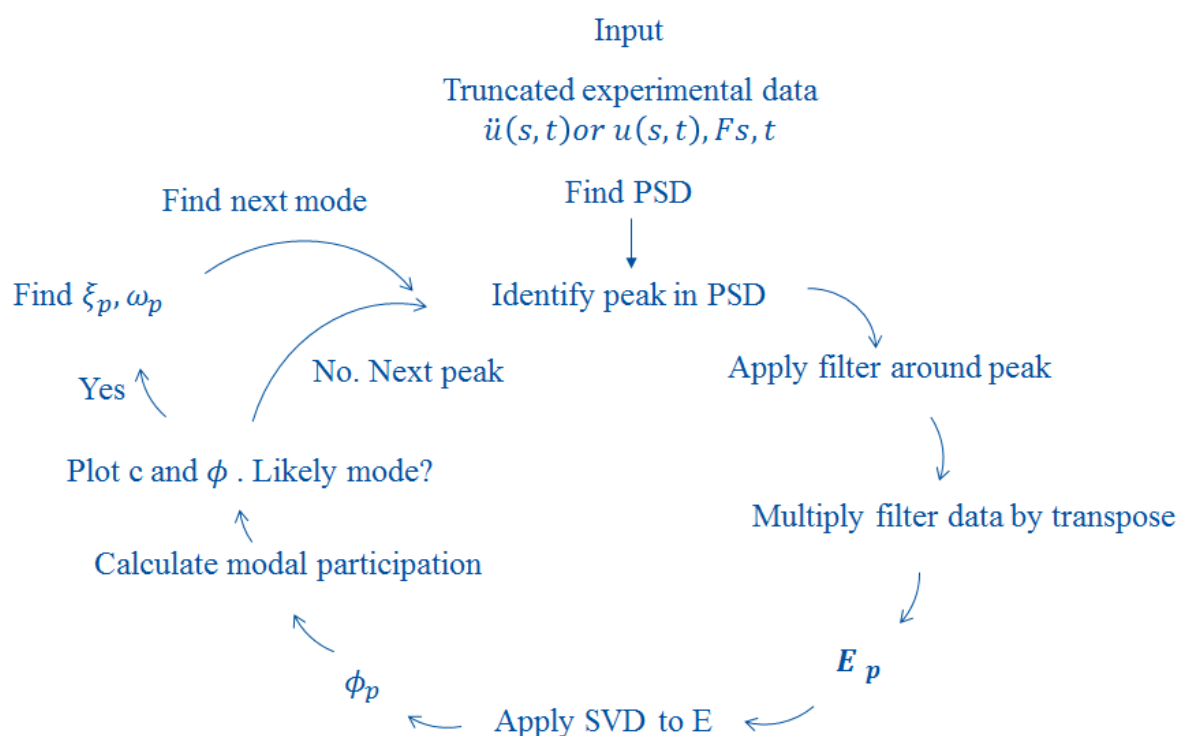
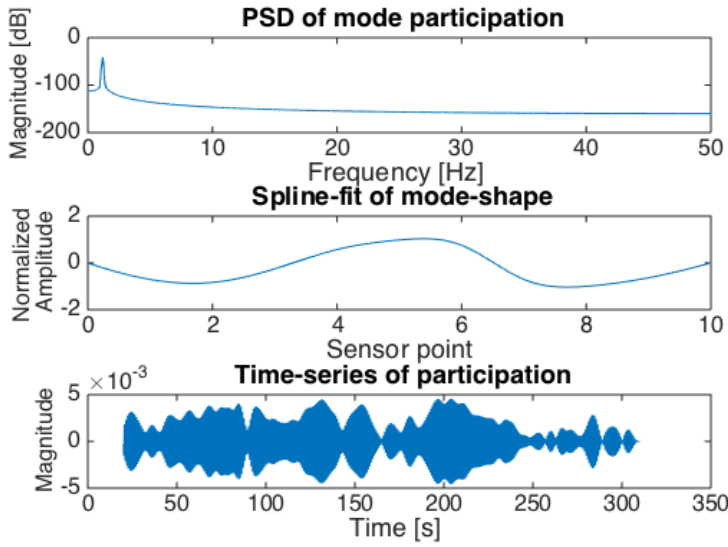
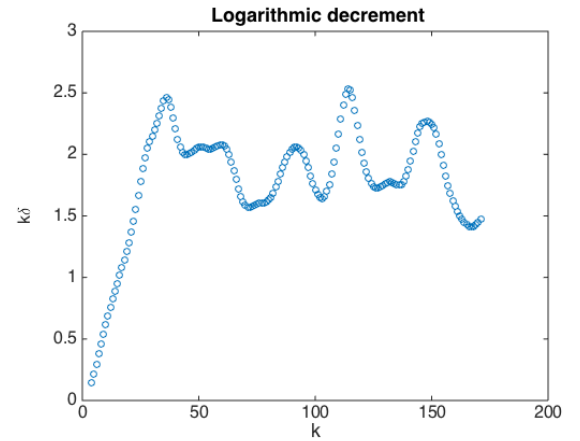


Figure 5.13: Flow-chart of implemented TDD method in Matlab

The codes allow for keeping or discarding plotted mode-shapes at identified PSD peaks, to help eliminate erroneous mode-shape identification due to data noise or closely spaced modes, using the identification window, Figure 5.14 (a). The slope of the decrement used for determining the damping is identified by the first, nearly linear, slope of Figure 5.14 (b).



(a)



(b)

Figure 5.14: (a) The identification window of the implemented TDD codes. (b) The identification window for determining the decrement slope for damping.

### 5.3.1 Results

Appendix C shows all the identified modes, their corresponding frequencies, mode shapes and damping according to the TDD method. By visual inspection, and by studying AutoMAC matrices (Figure 5.15) we can organize the results into the identified natural frequencies as in Tables 5.7, 5.8 and 5.9. Note that there is a possibility of failure in our visual inspection due to spatial aliasing as we are using a spline fitting function in Matlab, and as the values at accelerometer location 7 are linearly interpolated. Identified frequency peaks may also be a result of noise in the data resulting from the measurement equipment, the catenary carriage or other hydrodynamic effects. Hence, the corresponding identified mode shapes may resemble mode shapes, but will not correspond to actual modes. These false frequencies must be identified by comparisons between results from the various cases and methods, and are only ruled out where MAC values and eigenvalue deviation are distinctly weak.

#### 5.3.1.1 0.12 m/s case

Figure 5.15 shows a matrix containing MAC-values of each identified mode shape by TDD method,  $\phi_i$ , to each of the numerically calculated mode shapes,  $\phi_j$ . Here, the values of  $i$  do not necessarily correspond to the  $i^{th}$  mode, but represents the sequential step when the mode shape

was obtained. Values larger than 0.9 are considered relatively good values, but as the measurements are relatively noisy, lower values are included in the Tables 5.7, 5.8 and 5.9 for the sake of comparison, as the natural frequencies may match better than the mode shapes.

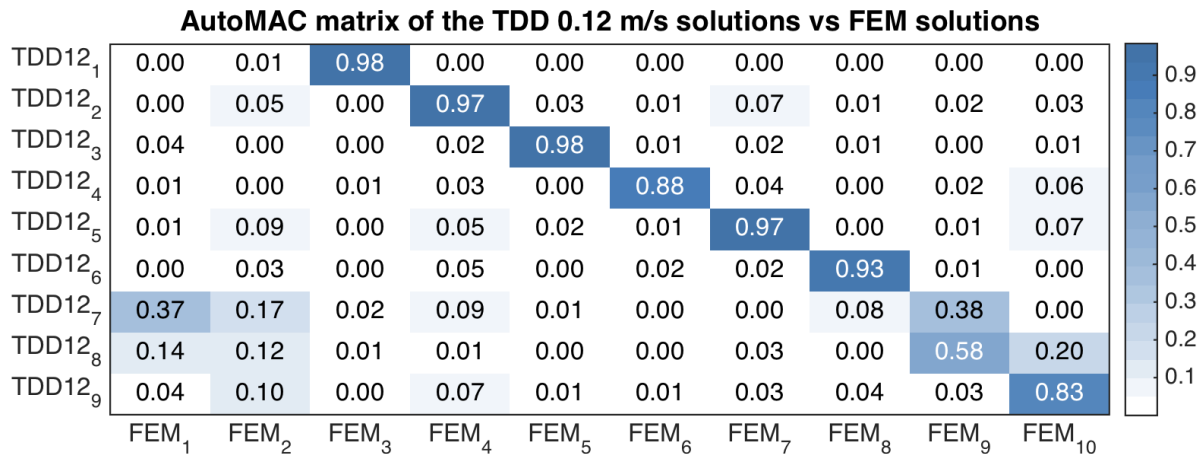


Figure 5.15: AutoMAC matrix from the comparison of the 0.12 m/s data using the TDD method and the FEM solutions

Notice that there are frequencies present in the 0.12 m/s signal starting from mode number 3, Table 5.7. As the observable mode shapes are limited due to the number of accelerometers, the mode shapes of the higher observed frequencies for this flow velocity could not be readily predicted. According to Table 5.4, modes higher than the 4<sup>th</sup> mode should not be excited, as a 0.12 m/s velocity is not supposed to excite modes higher than the 3<sup>rd</sup> mode. However, although the magnitudes of these frequencies in the PSD are of relatively negligible size, their mode shapes are still observed to have MAC-values relatively close to unity.

Modes 3, 4, 5 and 7 are the modes with the least amount of noise relative to the numerical solutions, and as can be seen, their deviations in terms of natural frequencies do not seem to have any noticeable trend.



Table 5.7: Identified natural frequencies using the TDD method on 0.12 m/s flow velocity results

| Mode no. | Natural frequency [Hz] | Damping [%] | Eigenvalue deviation from FEM [%] | MAC-FEM |
|----------|------------------------|-------------|-----------------------------------|---------|
| 1-2      | -                      | -           | -                                 | -       |
| 3        | 1.19                   | 1.22        | 12.40                             | 0.98    |
| 4        | 1.72                   | 0.25        | -1.11                             | 0.97    |
| 5        | 2.70                   | 1.84        | 3.30                              | 0.98    |
| 6        | 3.57                   | 0.09        | -2.99                             | 0.88    |
| 7        | 5.26                   | 0.21        | 6.58                              | 0.97    |
| 8        | 6.67                   | 0.27        | 4.37                              | 0.93    |
| 9        | 9.09                   | 1.03        | 13.22                             | 0.58    |
| 10       | 10.00                  | 0.79        | 1.37                              | 0.83    |

### 5.3.1.2 0.24 m/s case

As could be expected, Table 5.8 shows that the 0.24 m/s case seems to have more problems with identifying the lower modes, but predicts the higher modes better than for the 0.12 m/s case in comparison with numerical results. The AutoMAC plot can be found in Appendix C. Again the, eigenfrequencies carrying the larges magnitudes in the PSD predict the mode shapes well in comparison with the numerical solutions, although their eigenvalues differ by a relatively large amount.

Also, modes 8 and 9 are difficult to classify, as there are spurious modes or spatial aliasing present. However, in comparison with the 0.12 m/s case, it is more likely that the 8<sup>th</sup> mode has a frequency of about 6.67 Hz. The 9<sup>th</sup> mode is seemingly found at 8.33 Hz, as it is closer to the numerical calculations in MAC and eigenvalues.

Table 5.8: Identified natural frequencies using the TDD method on 0.24 m/s flow velocity results

| Mode no. | Natural frequency [Hz] | Damping [%]    | Eigenvalue deviation from FEM [%] | MAC-FEM         |
|----------|------------------------|----------------|-----------------------------------|-----------------|
| 1-2      | -                      | -              | -                                 | -               |
| 3        | 1.11                   | 0.73           | 4.89                              | 0.69            |
| 4        | 1.79                   | 2.32           | 2.45                              | 0.58            |
| 5        | 2.86                   | 0.10           | 9.19                              | 0.97            |
| 6        | 4.17                   | 1.16           | 13.19                             | 0.98            |
| 7        | 5.88                   | 0.07           | 19.12                             | 0.83            |
| 8        | 6.67/7.69              | 0.22/0.11      | 4.37/20.43                        | 0.95/0.95       |
| 9        | 8.33/9.09/<br>10.00    | 0.23/1.01/0.02 | 3.78/13.22/24.54                  | 0.99/0.85/ 0.79 |
| 10       | -                      | -              | -                                 | -               |

---

### 5.3.1.3 0.34 m/s case

For the 0.34 m/s case, a larger number of modes seem to be excited. Although the frequency identified as mode no. 6 has the largest magnitude in the PSD, in agreement with the calculated modes of Table 5.4, it seems that modes 7 and 8 are also well defined in the measured response. It seems that modes 1 and 2 are difficult to identify due to large amounts of noise in the lower frequencies, so the frequency shown in Table 5.9 corresponding to mode 2 is not expected to be an actual mode.

*Table 5.9: Identified natural frequencies using the TDD method on 0.34 m/s flow velocity results*

| Mode no. | Natural frequency [Hz] | Damping [%] | Eigenvalue deviation from FEM [%] | MAC-FEM   |
|----------|------------------------|-------------|-----------------------------------|-----------|
| 1        | -                      | -           | -                                 | -         |
| 2        | 0.95                   | 4.01        | 70.62                             | 0.32      |
| 3        | 1.79                   | 0.88        | 68.59                             | 0.93      |
| 4        | 1.39                   | 3.16        | -20.30                            | 0.83      |
| 5        | 2.70                   | 1.26        | 3.29                              | 0.86      |
| 6        | 4.35                   | 0.45        | 18.10                             | 0.95      |
| 7        | 5.56                   | 0.68        | 12.50                             | 0.99      |
| 8        | 6.67/7.69              | 0.82/0.53   | 4.37/20.43                        | 0.99/0.85 |
| 9        | 9.09                   | 0.16        | 13.22                             | 0.88      |
| 10       | 10.00                  | 0.61        | 1.372                             | 0.40      |

---

## 5.4 OMA investigations using MACEC

As part of the verification of the implemented TDD method in this thesis, the commercial software MACEC is used, which is a Matlab toolbox software. With its graphical user interface (GUI) it is very intuitive, but requires a user's basic knowledge of the OMA approaches available, and introduced in Section 4.3. The MACEC program was first coded as a part of a Master thesis project in 1997-1998. The code was then modified during Ph.D work between 1998 and 2001, and finally got a face-lift and new features as part of a Ph.D study between 2006 and 2011. Accompanying the software itself is a thorough User Manual, which provides tutorials on example cases relevant to a number of applications of the software (Reynders et al. 2014).

The input loading is unknown for the case studies relevant to this thesis. However, MACEC also includes methods for reference-based means of system identification, where a reference could be, for example, a load time-series at a specific node or many nodes. In the absence of input information, the modes and mode-shapes must be estimated using the output-only techniques. This limits the available methods to:

- Nonparametric PSD<sup>+</sup> using the correlogram and periodogram methods. Here, Peak Picking or CMIF/FDD can be selected.
- Reference-based data-driven stochastic subspace identification (DD-SSI)
- Reference-based covariance-driven stochastic subspace identification (Cov-SSI)
- Operational poly-reference Least Squares Complex Frequency identification

Because the Peak Picking method is much simpler than the TDD method, and the FDD method shares most of its features with the TDD method, the non-parametric methods are not adopted for this thesis.

A schematic step-by-step procedure of the MACEC investigations carried as part of this thesis can be found in Appendix B.

Output files from MACEC contain valuable information about natural frequencies, mode-shapes and damping, and the Cov-SSI method also returns information about the standard deviations of the output.

As the methods used in MACEC are not SDOF methods like the TDD method, the methods allow for identification of complex modes with phase shifts between elements. However, for

---

this case study, the mode shapes are expected to be normal, and it is, therefore, assumed that the large spreads in the complexity plots, see Figure 5.16 (b), are due to noise.

The plotted mode shapes are the real parts of the complex modes. Complex plots, mode shapes and AutoMAC matrices of all the MACEC obtained data can be found in Appendix D, and in the following the results are sorted in tables according to the modes they correspond to. The same limitations related to spatial aliasing or spurious frequencies as for the TDD method in Section 5.3.1 also apply to these methods.

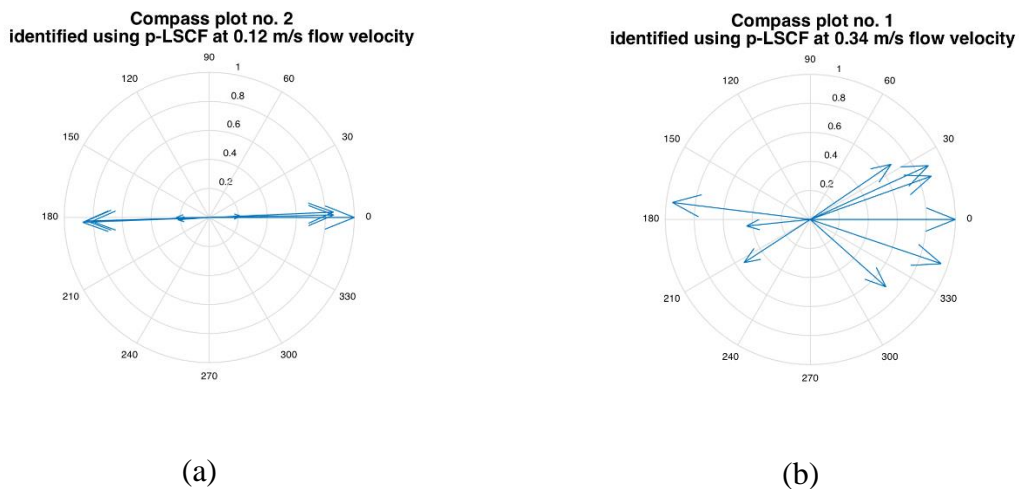


Figure 5.16: Complexity plots of (a) A very normal mode, the 4<sup>th</sup> mode found by 0.12 m/s velocity p-LSCF. (b) A relatively complex mode, the 3<sup>rd</sup> mode found by 0.34 m/s velocity p-LSCF

## 5.4.1 Results

### 5.4.1.1 Poly-reference Least Square Complex Frequency method

As this method has a stricter convergence criteria than the TDD method, less frequencies are identified as natural frequencies for the system. An example of a stabilization diagram used for the identification of modes using the p-LSCF method on 0.12 m/s current flow is shown in Figure 5.17. As can be seen, only one pole is stable throughout the model orders. This is due to the pole having the largest magnitude in the PSD, and supports the theory that vortex induced vibrations principally only contain one frequency, the lock-in frequency. However, it is clear that multiple frequencies are present nonetheless, and a few have been identified and compared with the FEM solutions in terms of MAC-values. Note that the stabilization criteria are altered

for all of the methods due to a large amount of noise in the data, and this must be considered when comparing results.

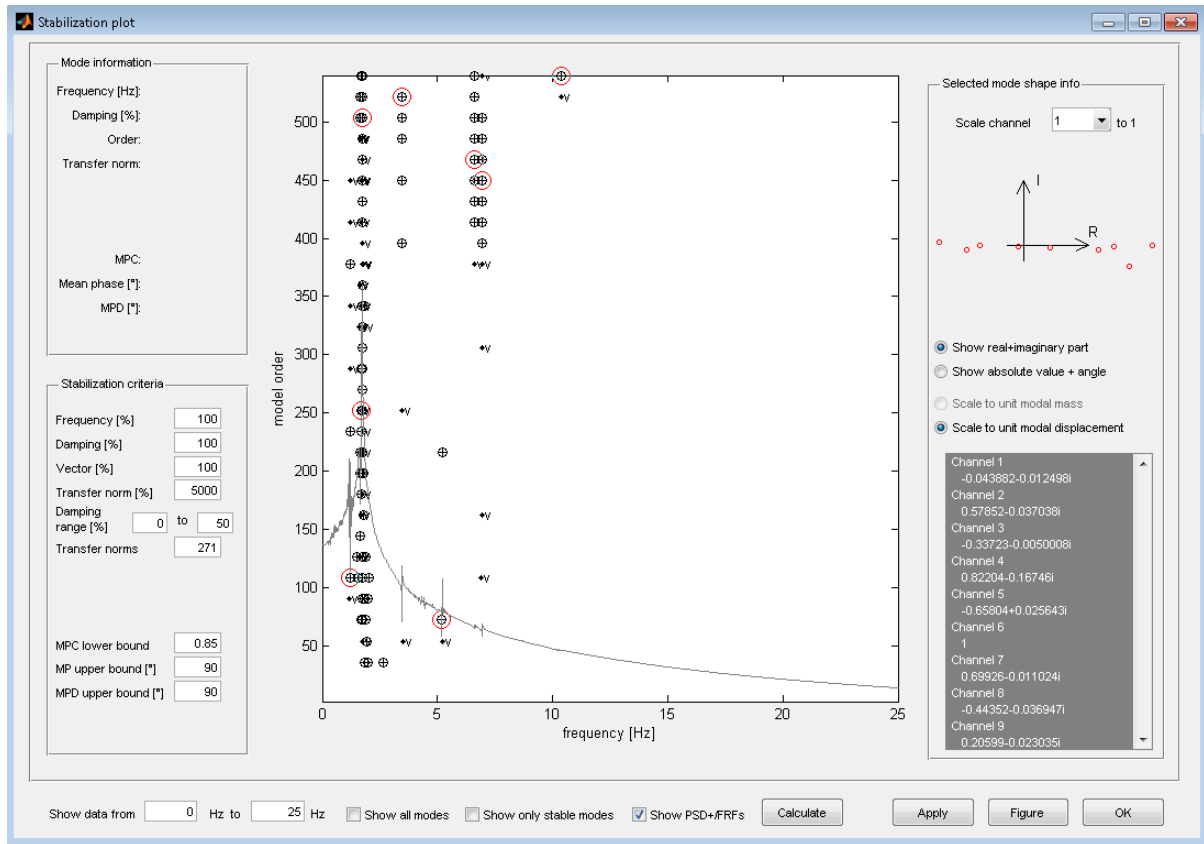


Figure 5.17: Stabilization diagram for the p-LSCF 0.12 m/s case

For the 0.12 m/s case the identified modes are found in Table 5.10. Notice the two stable poles with frequencies of 6.63 and 6.93 Hz respectively, both identified as mode 8, the 6.63 Hz frequency is closer to the numerical solutions, while the 6.93 Hz solution has a lower damping and mean phase deviation, supporting its selection.

Table 5.10: Identified natural frequencies using the p-LSCF method on 0.12 m/s flow velocity results

| Mode no. | Natural frequency [Hz] | Damping [Hz] | MPC [-]   | MPD [-]   | Eigenvalue deviation from FEM [%] | MAC-FEM [-] |
|----------|------------------------|--------------|-----------|-----------|-----------------------------------|-------------|
| 1-3      | -                      | -            | -         | -         | -                                 | -           |
| 4        | 1.75                   | 7.42         | 0.99      | 1.49      | 0.28                              | 0.97        |
| 5        | -                      | -            | -         | -         | -                                 | -           |
| 6        | 3.47                   | 0.03         | 0.97      | 3.36      | -5.64                             | 0.93        |
| 7        | 5.19                   | 0.12         | 0.94      | 2.75      | 5.06                              | 0.59        |
| 8        | 6.63/6.93              | 0.06/0.02    | 0.97/0.97 | 1.47/0.48 | 3.76/8.56                         | 0.97/0.91   |
| 9        | -                      | -            | -         | -         | -                                 | -           |
| 10       | 10.37                  | 0.03         | 0.97      | -2.98     | 0.05                              | 0.93        |

The three identified modes in the 0.24 m/s current velocity, Table 5.11, all have good MAC, MPC and MPD values, but they all have a deviation of about 10% in comparison to the FEM eigenvalues.

Table 5.11: Identified natural frequencies using the p-LSCF method on 0.24 m/s flow velocity results

| Mode no. | Natural frequency [Hz] | Damping [Hz] | MPC [-] | MPD [-] | Eigenvalue deviation from FEM [%] | MAC-FEM [-] |
|----------|------------------------|--------------|---------|---------|-----------------------------------|-------------|
| 1-4      | -                      | -            | -       | -       | -                                 | -           |
| 5        | 2.89                   | 0.06         | 0.99    | 2.61    | 10.60                             | 0.96        |
| 6        | 4.07                   | 0.09         | 0.91    | -0.27   | 10.55                             | 0.97        |
| 7-8      | -                      | -            | -       | -       | -                                 | -           |
| 9        | 8.69                   | 0.01         | 0.96    | 2.32    | 8.16                              | 1.00        |
| 10       | -                      | -            | -       | -       | -                                 | -           |

Notice in Table 5.12 that the mode identified as the 3<sup>rd</sup> mode using the p-LSCF method and the 0.34 m/s flow velocity measurements has a very large deviation to the 3<sup>rd</sup> modes identified using the 0.12 m/s and 0.24 m/s velocity results and the TDD method, and to the numerical solution. It is supported by the results of the TDD analysis of the 0.34 m/s measurements, but its stabilization diagram did not contain a very stable pole, so this result must be considered with caution. Also, its corresponding complexity plot, found in Figure 5.16 (b) suggests that

there is either a large amount of noise or un-proportional damping present, so the mode should not have been plotted as a real mode, and therefore shows an erroneously large MAC-value.

*Table 5.12: Identified natural frequencies using the p-LSCF method on 0.34 m/s flow velocity results*

| Mode no. | Natural frequency [Hz] | Damping [Hz] | MPC [-] | MPD [-] | Eigenvalue deviation from FEM [%] | MAC-FEM [-] |
|----------|------------------------|--------------|---------|---------|-----------------------------------|-------------|
| 1-2      | -                      | -            | -       | -       | -                                 | -           |
| 3        | 1.83                   | 0.27         | 0.55    | 3.88    | 72.95                             | 0.95        |
| 4        | -                      | -            | -       | -       | -                                 | -           |
| 5        | 3.15                   | 1.40         | 0.95    | 0.20    | 20.42                             | 0.72        |
| 6        | 4.28                   | 2.34         | 0.97    | -0.84   | 16.15                             | 0.99        |
| 7-8      | -                      | -            | -       | -       | -                                 | -           |
| 9        | 8.92                   | 0.18         | 0.94    | 0.00    | 11.09                             | 0.91        |
| 10       | 10.67                  | 0.17         | 0.94    | -0.45   | 8.18                              | 0.98        |



### 5.4.1.2 Covariance Driven Stochastic Subspace method

The results of the Cov-SSI method analysis all produced very few identified modes, but the identified modes all have relatively stable poles in the stabilization diagrams, see Figure 5.18. Modifying the stabilization criteria further did not produce more stable poles.

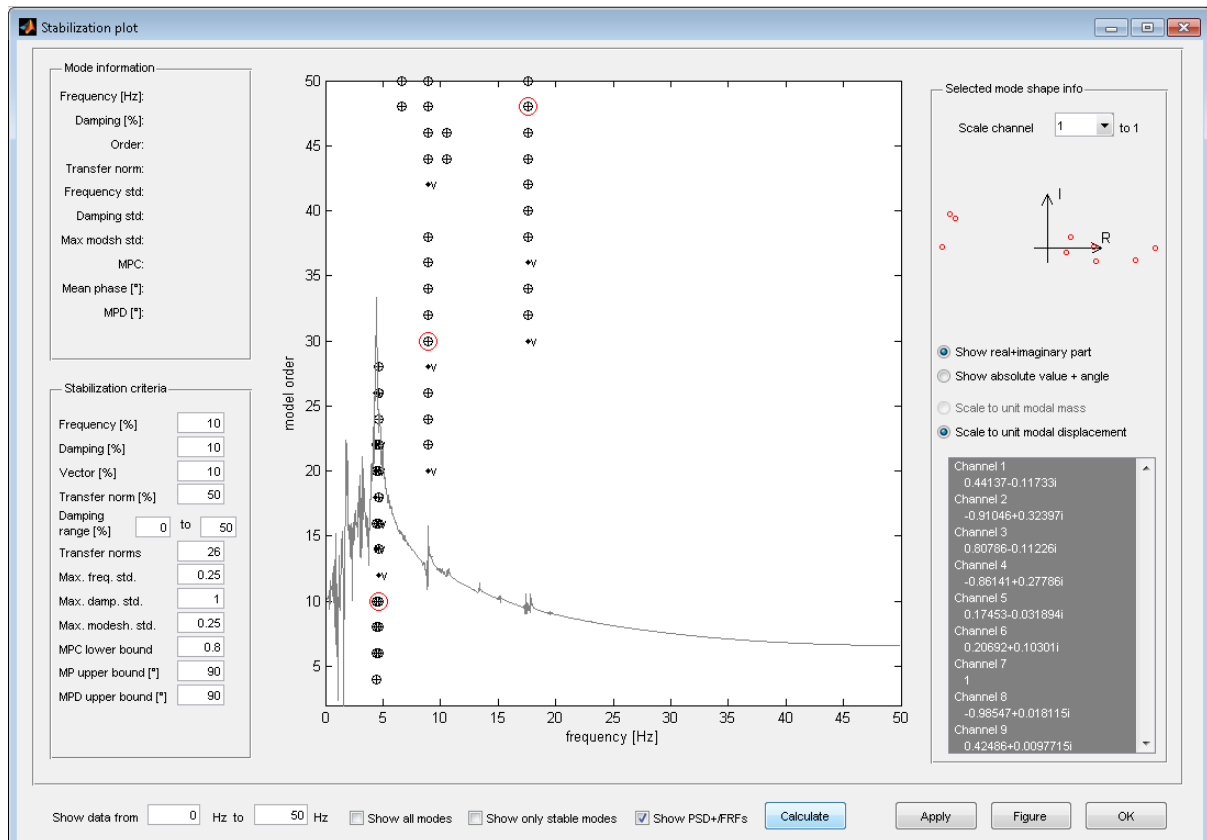


Figure 5.18: Example stabilization diagram for the Cov-SSI 0.34 m/s case.

Notice that all of the identified natural frequencies in Tables 5.13 to 5.15 except mode no.5 in the 0.12 m/s flow velocity have deviances to the numerical solutions of about 10 % or more. The largest deviation determined by the Cov-SSI method, is found in the 6<sup>th</sup> mode in the 0.34 m/s case, Table 5.15, which also has a relatively low MAC-value, even though it is the mode that is excited the most. The complexity plot for this mode, found in Appendix C, looks relatively normal, so the deviation could more likely be a result of measurement error or noise.

Table 5.13: Identified natural frequencies using the Cov-SSI method on 0.12 m/s flow velocity results

| Mode no. | Natural frequency [Hz] | Damping [Hz] | MPC [-] | MPD [-] | Eigenvalue deviation from FEM [%] | MAC-FEM [-] |
|----------|------------------------|--------------|---------|---------|-----------------------------------|-------------|
| 1-3      | -                      | -            | -       | -       | -                                 | -           |
| 4        | 1.20                   | 1.96         | 0.99    | 1.86    | 13.32                             | 0.98        |
| 5        | 1.73                   | 0.04         | 1.00    | 1.50    | -0.83                             | 0.97        |
| 6-10     | -                      | -            | -       | -       | -                                 | -           |

Table 5.14: Identified natural frequencies using the Cov-SSI method on 0.24 m/s flow velocity results

| Mode no. | Natural frequency [Hz] | Damping [Hz] | MPC [-] | MPD [-] | Eigenvalue deviation from FEM [%] | MAC-FEM [-] |
|----------|------------------------|--------------|---------|---------|-----------------------------------|-------------|
| 1-4      | -                      | -            | -       | -       | -                                 | -           |
| 5        | 2.90                   | 0.04         | 0.93    | 2.50    | 10.76                             | 0.96        |
| 6-8      | -                      | -            | -       | -       | -                                 | -           |
| 9        | 8.69                   | 0.04         | 0.94    | 3.24    | 8.28                              | 0.99        |
| 10       | -                      | -            | -       | -       | -                                 | -           |

Table 5.15: Identified natural frequencies using the Cov-SSI method on 0.34 m/s flow velocity results

| Mode no. | Natural frequency [Hz] | Damping [Hz] | MPC [-] | MPD [-] | Eigenvalue deviation from FEM [%] | MAC-FEM [-] |
|----------|------------------------|--------------|---------|---------|-----------------------------------|-------------|
| 1-5      | -                      | -            | -       | -       | -                                 | -           |
| 6        | 4.48                   | 0.06         | 0.96    | -1.15   | 21.59                             | 0.83        |
| 7-8      | -                      | -            | -       | -       | -                                 | -           |
| 9        | 8.89                   | 0.56         | 0.96    | 2.85    | 10.74                             | 0.90        |
| 10       | -                      | -            | -       | -       | -                                 | -           |

### 5.4.1.3 Data-Driven Stochastic Subspace Identification method

According to Table 5.16, the 3<sup>rd</sup>, 4<sup>th</sup> and 8<sup>th</sup> mode are identified to a large degree of certainty under the assumption of normal modes, as the MPC and MAC values are both close to unity. The eigenvalue deviations do not suggest any clear trends, which would be useful for identifying the reasons behind the discrepancies between measured and numerically predicted results. The other identified modes for this velocity case and method have slightly lower MPC values, and are therefore either complex modes, spurious modes or contain larger amounts of noise.

Table 5.16: Identified natural frequencies using the DD-SSI method on 0.12 m/s flow velocity results

| Mode no. | Natural frequency [Hz] | Damping [Hz] | MPC [-] | MPD [-] | Eigenvalue deviation from FEM [%] | MAC-FEM [-] |
|----------|------------------------|--------------|---------|---------|-----------------------------------|-------------|
| 1-2      | -                      | -            | -       | -       | -                                 | -           |
| 3        | 1.20                   | 1.28         | 0.99    | 2.02    | 13.50                             | 0.98        |
| 4        | 1.73                   | 0.02         | 0.99    | 1.48    | -0.84                             | 0.97        |
| 5        | -                      | -            | -       | -       | -                                 | -           |
| 6        | 3.51                   | 0.79         | 0.84    | -0.40   | -4.58                             | 0.92        |
| 7        | 5.20                   | 0.27         | 0.86    | -10.90  | 5.34                              | 0.96        |
| 8        | 6.80                   | 0.18         | 0.98    | 2.82    | 6.49                              | 0.97        |
| 9-10     | -                      | -            | -       | -       | -                                 | -           |

Notice that Table 5.17 shows close to the same value for mode 5 as the other 3 methods do, supporting its identification. Also, the MPC and MAC values are relatively good. Modes 3 and 4 contain large amounts of damping, likely from noise, but the 3<sup>rd</sup> mode looks likely in terms of MPC and MAC value. The higher modes also behave well. However, when investigating some of the frequencies outside of the assumed identifiable mode range, it was noticed that the 10<sup>th</sup> mode shares linearity with the 12<sup>th</sup> mode as well as the 10<sup>th</sup>, so it may contain large amounts of noise, see Figure 5.19.

Table 5.17: Identified natural frequencies using the DD-SSI method on 0.24 m/s flow velocity results

| Mode no. | Natural frequency [Hz] | Damping [Hz] | MPC [-] | MPD [-] | Eigenvalue deviation from FEM [%] | MAC-FEM [-] |
|----------|------------------------|--------------|---------|---------|-----------------------------------|-------------|
| 1-2      | -                      | -            | -       | -       | -                                 | -           |
| 3        | 1.1528                 | 7.9148       | 0.9169  | -5.0306 | 8.82                              | 0.89        |
| 4        | 1.8037                 | 12.8815      | 0.8458  | 4.2817  | 3.45                              | 0.29        |
| 5        | 2.8991                 | 0.0401       | 0.9328  | 2.5798  | 10.79                             | 0.97        |
| 6-7      | -                      | -            | -       | -       | -                                 | -           |
| 8        | 7.4071                 | 1.3887       | 0.9212  | -3.6506 | 15.96                             | 0.95        |
| 9        | 8.6981                 | 0.0194       | 0.9429  | 3.0497  | 8.32                              | 0.99        |
| 10       | 10.3978                | 0.5496       | 0.9581  | 0.4672  | 5.40                              | 0.91        |

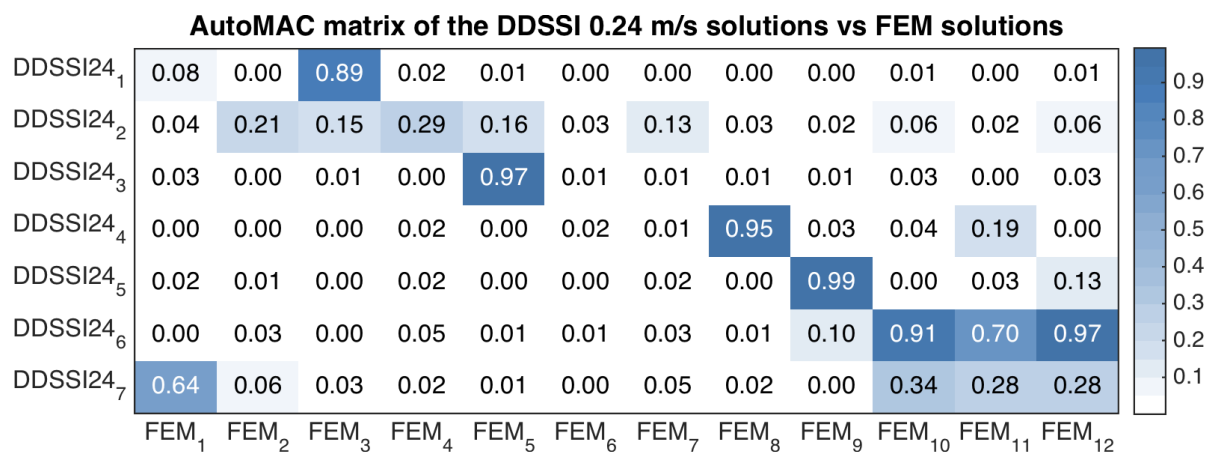


Figure 5.19: AutoMAC matrix of the DDSSI 0.24 m/s and FEM solution

The DD-SSI method 0.34 m/s case, Table 5.18, also identified the highest modes better than the lower modes. Notice that the 6<sup>th</sup> mode has a large deviation in eigenfrequency, although it has a higher MAC-value than the Cov-SSI method.

Table 5.18: Identified natural frequencies using the DD-SSI method on 0.34 m/s flow velocity results

| Mode no. | Natural frequency [Hz] | Damping [Hz] | MPC [-] | MPD [-] | Eigenvalue deviation from FEM [%] | MAC-FEM [-] |
|----------|------------------------|--------------|---------|---------|-----------------------------------|-------------|
| 1        | -                      | -            | -       | -       | -                                 | -           |
| 2        | 1.1562                 | 20.65        | 0.8982  | 1.7498  | 9.15                              | 0.51        |
| 3        | -                      | -            | -       | -       | -                                 | -           |
| 4        | 1.9261                 | 11.9707      | 0.9296  | -3.1908 | 10.48                             | 0.75        |
| 5        | 3.1159                 | 2.9477       | 0.9479  | 0.1501  | 19.07                             | 0.78        |
| 6        | 4.4592                 | 0.4871       | 0.9544  | -1.4217 | 21.13                             | 0.89        |
| 7        | 5.1531                 | 6.3966       | 0.939   | -0.2869 | 4.35                              | 0.99        |
| 8        | 6.6952                 | 4.552        | 0.9694  | 7.1751  | 4.82                              | 0.98        |
| 9        | 8.9013                 | 0.469        | 0.9639  | 2.8836  | 10.85                             | 0.90        |
| 10       | -                      | -            | -       | -       | -                                 | -           |

The 7<sup>th</sup> and 8<sup>th</sup> modes both have very good MAC values and MPC, but the 8<sup>th</sup> mode has a surprisingly large MPD. Still, a closer look at the complexity plot (Figure 5.20) reveals that the mode shape poles are still almost in a straight line, but are all deviating by values of about 10 degrees. Hence, the mode may still be normal and reliable.

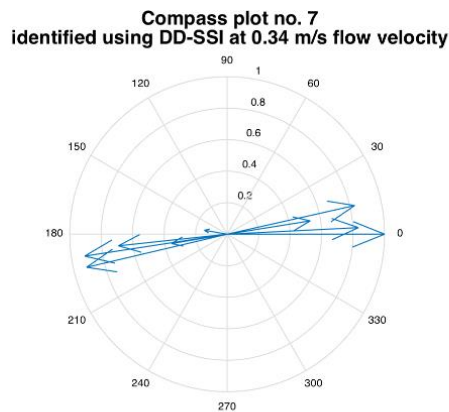


Figure 5.20: Complexity plot of the 8<sup>th</sup> mode using the DD-SSI method and 0.34 m/s current flow.

## 5.5 Numerical investigations of the accelerometers effects on the solution of the eigenvalue problem

The discussion of the deviation in mode-shapes and eigenvalues led to the hypothesis of the accelerometer mass and added mass influencing the experimental data. To investigate these effects, the codes used by Raed Lubbad in the numerical example presented in his doctoral thesis are modified for this thesis to account for masses at the accelerometer locations. The reason for this is to see if the assumption that the masses do not affect the experienced mode shapes is insufficient.

### 5.5.1 DNV DeepC and Riflex for Static Analysis

Because the closed-form solutions for the static configuration and tension variation is limited to strings, without bending stiffness, and the incorporation of local masses would deem a computationally heavy iterative process, the static configurations have been found using the DNV Deep C software module RIFLEX.

RIFLEX is a state-of-the-art software capable of analyzing flexible, metallic and steel catenary systems subject to hydrodynamic loading, and loading due to vessel-catenary interaction. The DeepC user interface makes the modelling easy and intuitive.

For the catenary case under investigation in this thesis, the line object of the software is used, connected to fairleads at points with a specified distance. Boundary conditions are applied at the ends so that the catenary is fixed from translational motion, but free to rotate in the catenary plane, see Table 5.19. The line characteristics used in the analysis are found in Table 5.2.

*Table 5.19: Boundary conditions of the modeled catenary*

| Direction | Translation | Rotation |
|-----------|-------------|----------|
| X         | Fixed       | Fixed    |
| Y         | Fixed       | Free     |
| Z         | Fixed       | Fixed    |

Lumped buoys are placed at the accelerometer locations, with the sizes and masses as presented in Table 5.20. The masses are not exact accelerometer masses, but likely masses of varying

size according to a similar study of accelerometer masses on a plate structure (Baharin & Abdul Rahman 2009). Figure 5.21 shows a 2D view of the catenary profile.

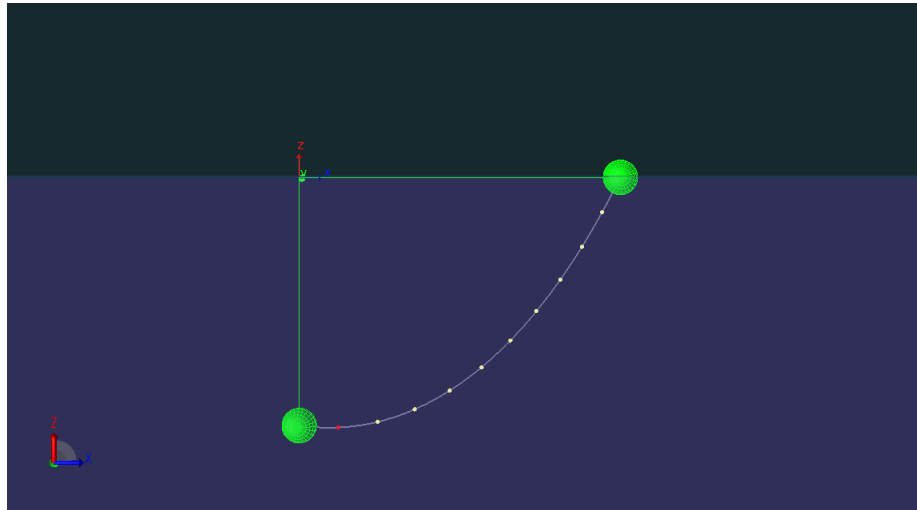


Figure 5.21: Static configuration using DeepC/RIFLEX

Table 5.20: Mass and dimensions of 6 accelerometer cases

|                 |         |         |         |         |         |         |
|-----------------|---------|---------|---------|---------|---------|---------|
| Mass (kg)       | 1       | 2       | 3       | 4       | 5       | Extreme |
|                 | 0.00584 | 0.01584 | 0.02584 | 0.03584 | 0.04584 | 1       |
| Dimensions (mm) | Length  |         | Breadth |         | Height  |         |
|                 | 5       |         | 2       |         | 5       |         |

## 5.5.2 Natural Frequency and Mode-Shape Investigation Using Matlab

The flow chart of the modified Matlab-scripts is found in Figure 5.22. The original codes are implemented based on techniques presented in Chapter 8.10 of (Kwon & Bang 2000).

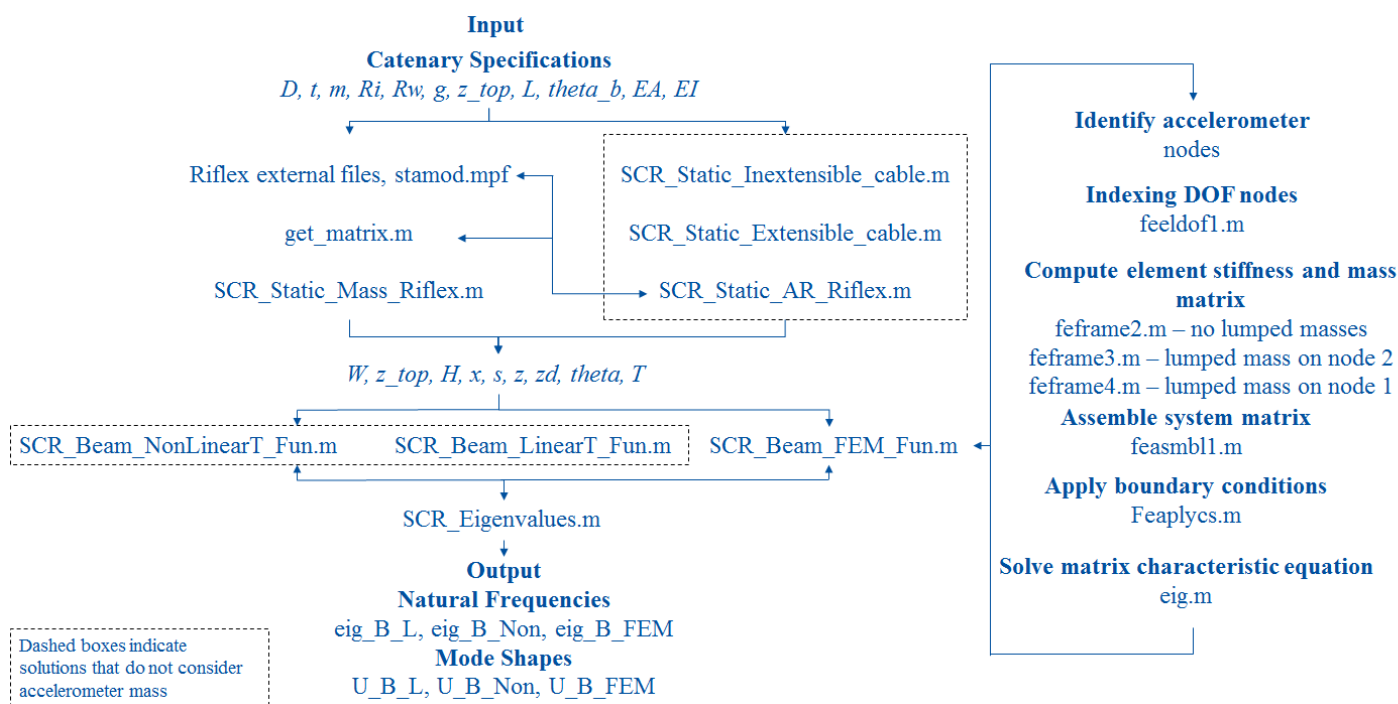


Figure 5.22: Flow-chart of matlab script for investigation of accelerometer effects

The resulting modes and mode-shapes are firstly compared with the numerically and analytically calculated values without loading, as presented in (Lubbad et al. 2011), primarily considering the solutions from the FEM code and non-linear tension variation of cables and beams, as discussed in Section 3.3. The comparison of the two methods for the case of catenaries without specific accelerometer loading is shown in Section 5.2.1. The comparison between the accelerometer mass loaded catenary with the pure catenary is given terms of MAC values for mode-shapes and percentage difference for natural frequencies. It is important, however, to remember that these values do not reveal anything about the accuracy of the solutions, but can give an indication of the precision of the solution.



### 5.5.3 Results

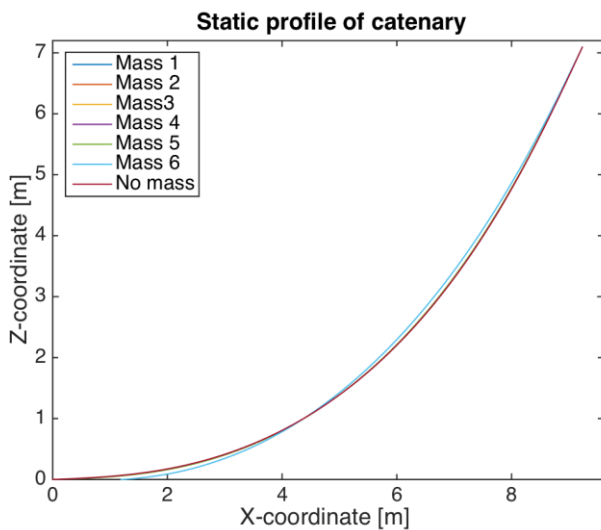


Figure 5.23: Static profile of accelerometer mass loaded catenary

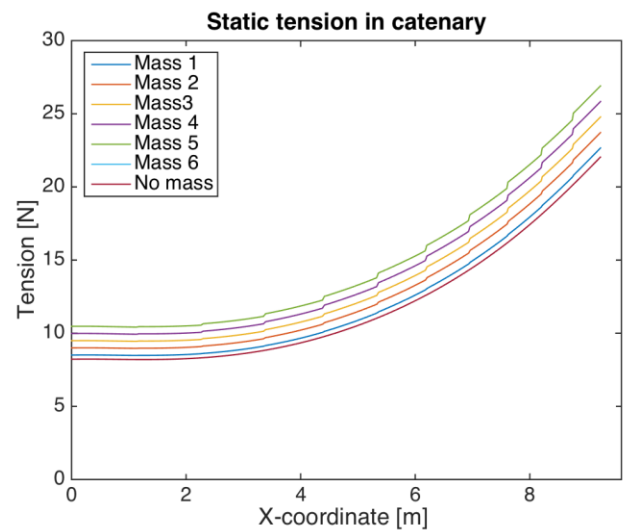


Figure 5.24: Tension profile of accelerometer mass loaded catenary

Figures 5.23 and 5.24 show the static profiles and tensions variation along the catenary obtained from the static analysis in RIFLEX. Noticeably, the profile does not change as a result of masses 1-5, while mass 6 is large enough to modify the profile. The tension along the catenary increases with increasing mass, and the discontinuities of the curves in the diagram of Figure 5.24 are results of the lumped masses.

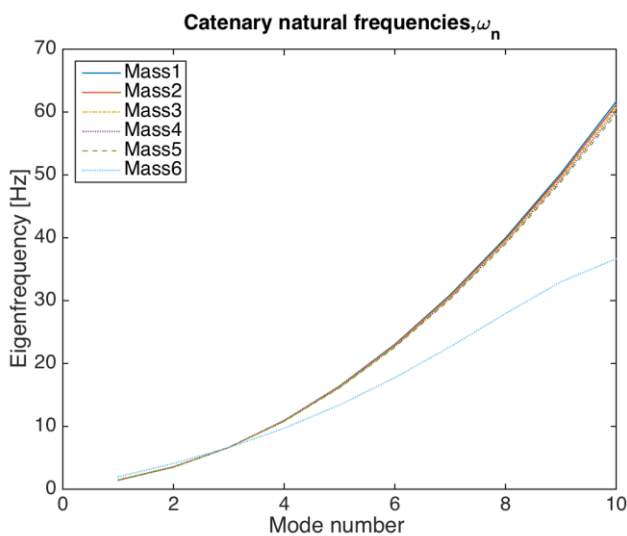


Figure 5.25: Calculated eigenfrequencies of accelerometer loaded catenary

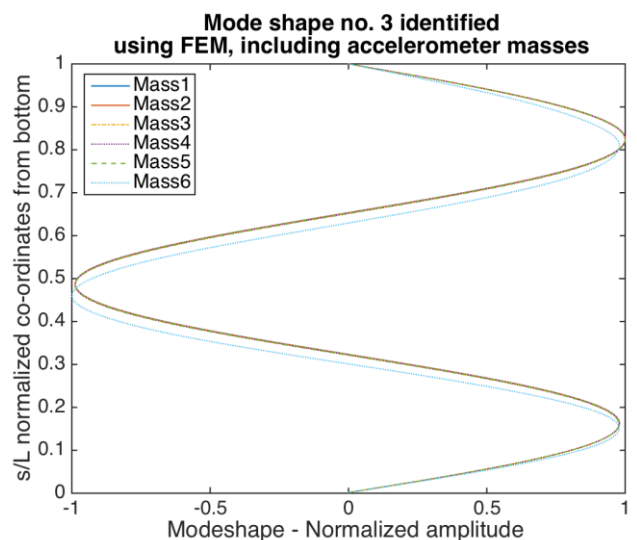


Figure 5.26: A plot of the 3rd mode shape obtained from FEM analysis of the accelerometer loaded masses

Figures 5.25 and 5.26 present the resulting eigenfrequencies and mode shape number 3 of the FEM analysis including accelerometer masses. The comparison of the results in Figure 5.25 to the solutions without accelerometer masses in terms of Eq.4.41 are presented in Table 5.21. As is shown, masses 1-6 increase the eigenfrequencies of the lower modes, and reduce the eigenfrequencies of the higher modes, but mode 3 seems to be kept almost constant.

Table 5.21: Eigenfrequencies of accelerometer loaded catenary relative to original FEM solution

| Mode no. | 1     | 2     | 3     | 4      | 5      | 6      | 7      | 8      | 9      | 10     |
|----------|-------|-------|-------|--------|--------|--------|--------|--------|--------|--------|
| Mass no. |       |       |       |        |        |        |        |        |        |        |
| 1        | 0.73  | 0.28  | -0.02 | -0.19  | -0.28  | -0.33  | -0.36  | -0.39  | -0.43  | -0.49  |
| 2        | 0.73  | 0.28  | -0.02 | -0.19  | -0.28  | -0.33  | -0.36  | -0.39  | -0.43  | -0.49  |
| 3        | 3.16  | 1.27  | -0.02 | -0.75  | -1.15  | -1.36  | -1.50  | -1.63  | -1.81  | -2.10  |
| 4        | 4.30  | 1.74  | -0.02 | -1.02  | -1.57  | -1.86  | -2.05  | -2.23  | -2.48  | -2.90  |
| 5        | 5.39  | 2.19  | -0.02 | -1.28  | -1.97  | -2.34  | -2.59  | -2.82  | -3.14  | -3.70  |
| 6        | 39.99 | 17.14 | -0.30 | -11.45 | -18.53 | -23.29 | -26.96 | -30.35 | -34.61 | -40.86 |

All the mode shapes obtained from the accelerometer loaded analysis are compared with the pure catenary results in terms of MAC-values in Figure 5.27. Figure 5.12 shows that there is little or no cross-correlation of the mode shapes associated with different mode numbers obtained numerically. Therefore, the correlations shown in Figure 5.27 are the MAC-values of mode shape  $\phi_i$  obtained from the accelerometer mass influenced analysis with  $\phi_j$  from the pure catenary analysis, where  $i = j$ , and  $i$  and  $j$  are mode numbers. Notice that the smallest mass has the largest effect on the shape of the higher modes, while the lower modes seem to be unaffected. Mass 6 seems to affect modes 2-5 the most, while the higher modes have increasing MAC-values.

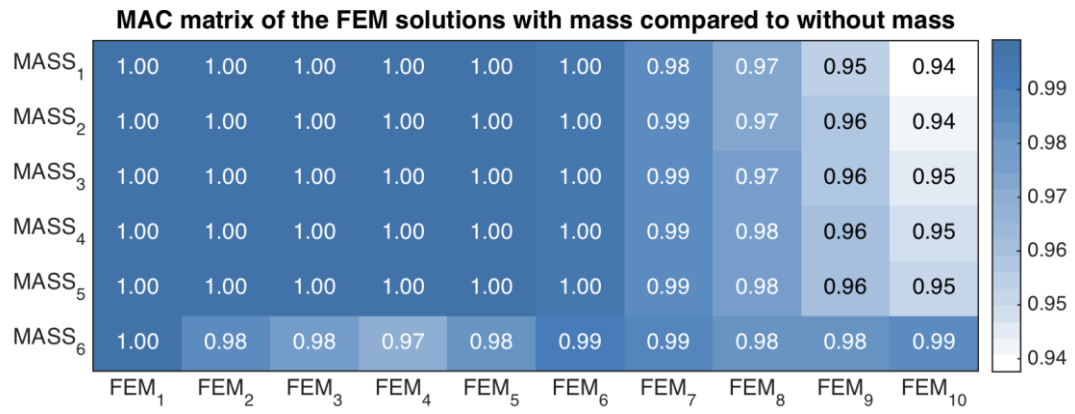


*Figure 5.27: MAC matrix of eigenfrequencies 1-10 of mass loaded mode shapes vs original FEM mode shapes*

## 5.6 Discussions

The following sections compare and discuss the results presented in Sections 5.3, 5.4, and 5.5, with additional information attached in Appendices C and D.

### 5.6.1 System identification and FEM comparison

The results presented in Sections 5.3 and 5.4 using the various OMA methods are plotted with their corresponding mode numbers in Figure 5.28. The solid line represents the numerically calculated natural frequencies using FEM, and not considering accelerometer masses. With observations based on this figure it is tempting to conclude that the FEM solutions, and therefore also the WKB solutions, predict the natural frequencies of the catenary quite well. However, notice that modes 7-10 are seemingly underestimated compared with all of the methods and current flow cases.

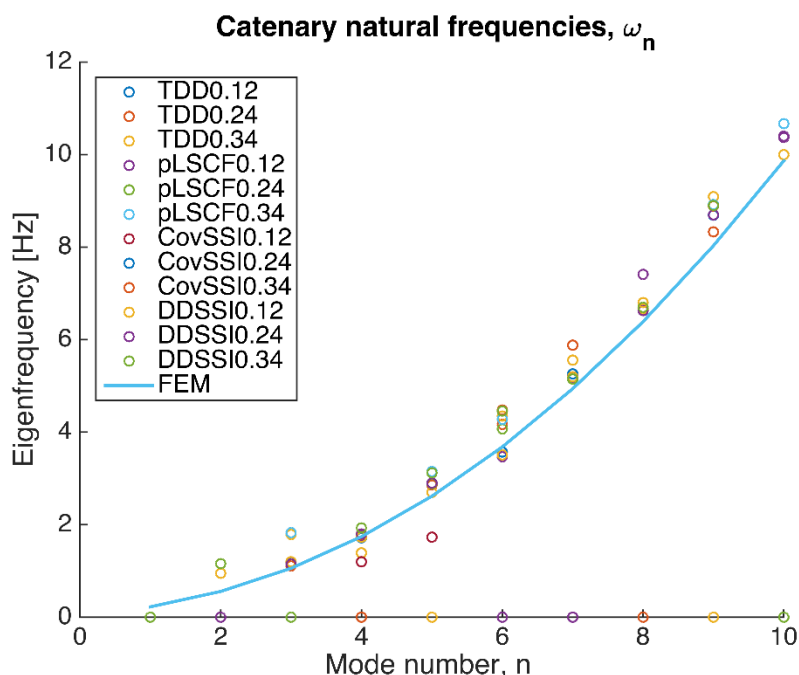


Figure 5.28: Experimental and FEM natural frequency results

The underestimation of natural frequencies can result from a range of faulty assumptions or errors in the system identification methods. An increase in tension along the catenary stiffens the structure, resulting in reduced frequencies for the higher modes. Therefore, one possible

---

reason for the underestimation of frequencies is an overestimation of the mass per unit length or constant added mass of the catenary.

Another potential source of error is the overestimation of complexity in the modes, resulting in overestimation of damping. However, as can be observed from Figure 5.29, the damping estimates for the highest considered modes are relatively low, deeming this source of error less likely.

The relative scatter of frequencies in each mode is difficult to explain. Especially the fact that a natural frequency can correspond to different mode shapes, e.g. 1.79, which is calculated to be the fourth mode using the TDD method with the 0.24 m/s current data, and the third mode using the TDD method with the 0.34 m/s current data. This could of course be a result of computational error, spurious frequencies and noise. However, in a note about VIV obtained by personal communication with Carl M. Larsen, he mentioned the possibility of the added mass effects on the preferred mode shape by the natural frequencies. This observation was also made in a VIV experiment investigating VIV in a shearing current of a rotating rig at MARINTEK (Lie et al. 1997). If this is the case, the analytical and numerical models describing the catenary equations of motion, Section 3.3, would have to be altered to include higher order added mass effects.

Figure 5.29 shows the scatter of damping estimates related to each of the mode numbers in all the current velocity cases. Clearly, there are large deviations, especially in the mode range with the largest participations in the various current flow cases. It is difficult to determine the reason for this large amount of error, and this is something that should be given more attention in further work. A possible reason is the amount of noise present, which can result from:

- The data not accurately being modelled by a state-space model
- Measurement noise due to sensor inaccuracies
- Computational noise due to the finite precision of the data series
- The finite number of data points

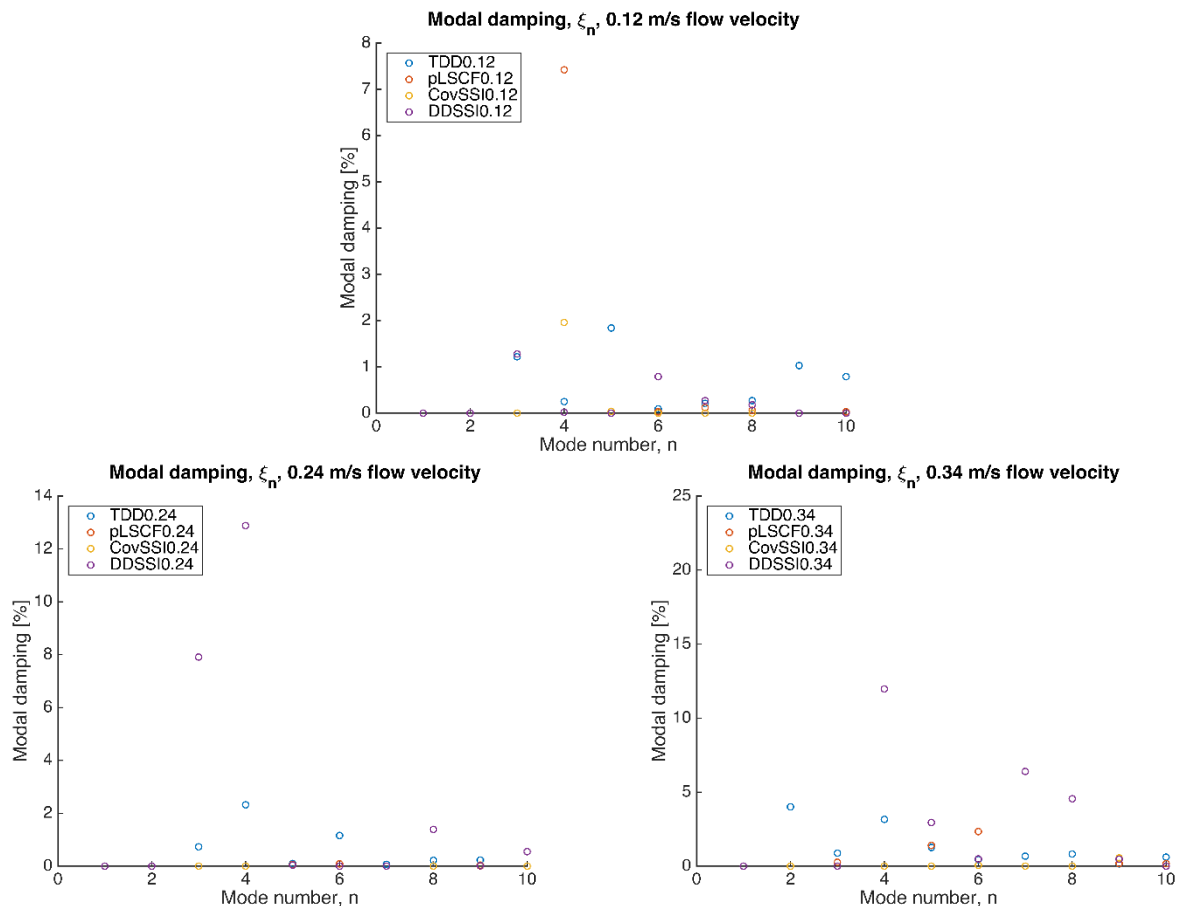


Figure 5.29: Modal damping estimate comparison

In comparison with FEM, MAC values calculated for the OMA obtained mode shapes are recognized to be very high, and for some cases even unity. Based on this observation and assuming that the complexities calculated in some of the modes are due to noise, a conclusion could be drawn that the potential for un-proportional damping in this case study riser is not very likely.

This observation also questions the assumption of the “space sharing” model of VIV analysis, and strengthens the reasoning for using a “time sharing” model, which assumes a travelling wave, as observed in most of the predicted mode shapes of this thesis. However, notice that in Figure 5.30 the mode with the largest participation is present for most of the time-series, while the other participating modes fluctuate more. But there is no clear tendency that one mode dies out as another increases. Therefore, by use of the “time sharing” method of VIV modelling, the responses are likely to be underestimated.

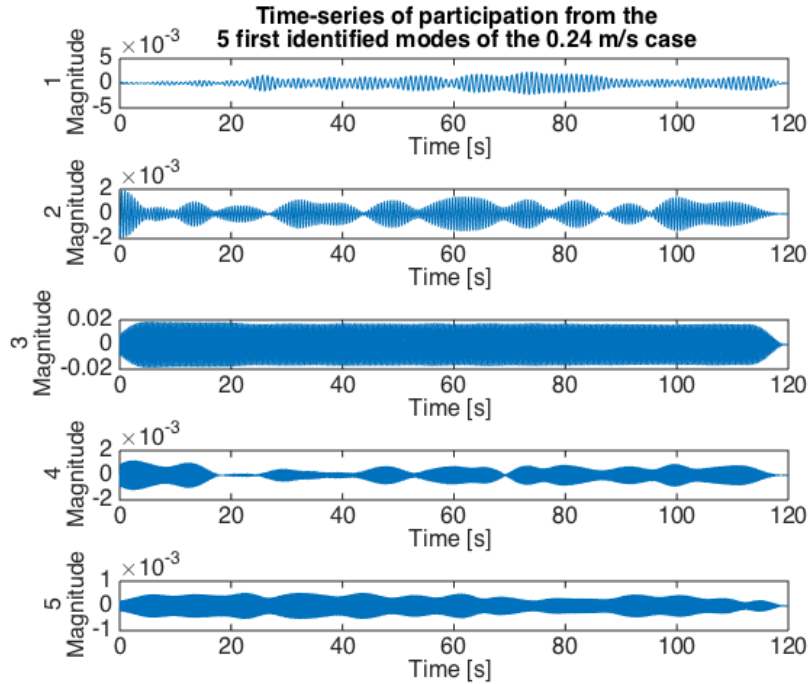


Figure 5.30: Time-series of modal participation of the 5 first identified modes used TDD with the 0.24 m/s measurements

### 5.6.2 Accelerometer added mass effects

The results of the numerical investigations presented in Section 5.5.3 show that the first order added mass effect due to the mass and volume of the accelerometers are not likely to be the reason for the deviations of the numerical solutions from results of preliminary studies of the experimental results. The results of the system identification studies in this thesis show that the deviations in mode shapes were more likely a result of noise and spline fitting errors in preliminary studies. The number of high MAC values supports this reasoning. Adding a reasonable amount of mass at the accelerometer locations did not alter the mode shapes noticeably, and did not create the expected damped mode shape effect.

Additionally, adding masses at the accelerometer locations increased the tension along the riser length. This resulted in the higher modes having lower natural frequencies than the catenary without lumped masses, conflicting with the observations shown in Section 5.6.1. A source of error in these calculations is the fact that the riser mass per unit length was kept constant, and should have been reduced to maintain a constant total weight, as measured by MARINTEK. This should be incorporated in further studies of this effect.





---

## Chapter 6

### Concluding remarks

In this thesis, general theories concerning vortex induced vibrations and their consequences in terms of dynamic responses in slender catenary structures have been presented and discussed. Operational modal analysis techniques for system identification of measured responses resulting from VIV are introduced and discussed.

Following from the theory of dynamic analysis of catenary structures subject to VIV, results from the 2001 MARINTEK experiment were used for the case study, with the purpose of trying to understand the relation between the presented analytical and numerical models, and observed measurements. The major conclusions of this study are as follows:

- Firstly, the TDD method is implemented in a Matlab program, considering three velocity cases of cross-flow displacements in the catenary plane. The results show that in each of the cases, one of the frequencies has a higher degree of contribution than other frequencies, but multiple frequencies are present throughout the measurements. Also, the frequencies corresponding to each mode varied. The obtained mode shapes have a relatively high degree of correlation with the numerically calculated mode shapes.
- Secondly, the poly-reference least squares complex frequency method and the DD- and Cov-SSI methods of OMA were used for studying the data in the commercial Matlab toolbox MACEC. As for the TDD method, the mode shape estimates have high MAC-values, and the corresponding natural frequencies vary. The damping estimates show a great amount of scatter. Also, there is a varying degree of certainty in the results, as some modal frequencies are more difficult to obtain due to signal noise or other sources of error.
- Continuing, the effect of accelerometer masses and first order added mass effects are studied using a numerical model in Matlab. There are limitations in the results because of the simplification of the added masses. However, based on the minimal changes in mode shapes, and the eigenvalues changing opposite to what they should in comparison with experimental data, the effects of the masses are concluded to be

negligible. This conclusion coincides with original assumptions made for the analytical and numerical models.

- A comparison between the OMA obtained eigenfrequencies and the corresponding numerically calculated modes show that there is a great amount of agreement in how the natural frequencies increase with mode number. However, for this case study, the analytical and numerical calculations apparently underestimate magnitudes of the frequencies. Also, there is a possibility that the frequencies corresponding to each mode shape vary resulting from higher order added mass effects, which are not considered in the numerical or analytical methods.

---

## Chapter 7 Recommendations for future work

It is recommended that further investigations into the dynamic responses of slender catenary structures subject to vortex induced vibrations are attempted. Areas that may be of interest in the continuation of this work are:

- Investigations of the reliability of the mass estimates resulting from the measurements done at MARINTEK in 2001. If the mass estimates are found to be higher than they should be, the numerical result would likely obtain a better fit with the results from the experimental study.
- In order to analytically or numerically reconstruct the measured responses, the incorporation of modal damping is necessary, as structural damping is present to a certain extent in the measurements. Investigations using a Rayleigh damping matrix in a finite element model could be of interest. However, better experimental damping estimates would be preferable in order to give better estimates of the weighting coefficients of Eq.3.10.
- As the observable range of modes is limited due to the number of accelerometer and their spacing, it would be preferable to obtain new measurements to verify or improve the results of this thesis. According to (Rainieri et al. 2014), the preferable record length for OMA is about 1000-2000 times the natural period of the fundamental mode, and this should be taken into account for future experiments. Improved equipment could also serve to obtain better quality observations, lowering noise levels in the measurements.
- New experimental data could also be used to study the damping estimates. This could better understanding of the large scatter in damping estimates shown in this thesis.
- Investigations of the possibility of multiple natural frequencies corresponding to the same mode shape, or changing mode shape due to higher order added mass effects.
- It would be interesting to investigate the actual observability of the presented experimental data. This could for example be done by use of an observability matrix.



---

## Bibliography

- Baharin, N. H. & Abdul Rahman, R. (2009). *Effect of accelerometer mass on thin plate vibration*. Jurnal Mekanikal. 100-111 pp.
- Blevins, R. D. (1994). *Flow-induced vibration*. 2nd ed. Malabar, Fla: Krieger.
- Brincker, R., Ventura, C. & Andersen, P. (2001). *Damping estimation by frequency domain decomposition*. 19th International Modal Analysis Conference. 698-703 pp.
- Carullo, A. & Parvis, M. (2001). *An Ultrasonic Sensor for Distance Measurement in Automotive Applications*. IEEE Sensors Journal. 143-147 pp.
- Casas, J., Cruz, P. & Casas, J. (2003). *Fiber optic sensors for bridge monitoring*. Journal of Bridge Engineering, 8, No. 6. pp. 362-373.
- Chopra, A. K. (2007). *Dynamics of structures: theory and applications to earthquake engineering*. 3rd ed. Prentice-Hall international series in civil engineering and engineering mechanics. Upper Saddle River, N.J: Pearson Prentice Hall.
- Cook, R. D. (2002). *Concepts and applications of finite element analysis*. 4th ed. New York: Wiley.
- Crowe, C. T. (2009). *Engineering fluid mechanics*. 9th ed. Hoboken, N.J: Wiley.
- DNV. (2006). *Free Spanning Pipelines: March 2006*. Recommended Practice, DNV-RP-F105. Høvik: Det Norske Veritas.
- DNV. (2010). *Riser Fatigue: October 2010*. Recommended Practice, DNV-RP-204. Høvik: Det Norske Veritas.
- Ewins, D. J. (2000). *Modal testing: theory, practice and application*. 2nd ed. Modal testing 2, vol. 10. Baldock: Research Studies Press.
- Faltinsen, O. M. (1993). *Sea loads on floating offshore systems*. Richardson, TX: OTC.
- Fang, S. M. (2013). *Structural Response Evaluation Using Non-Uniform Sensor Arrays*: Texas A&M University. 262 pp.
- Fang, S. M. N., J. M. (2014). *Comparison of Airfoil And Ribbon Fairings For Suppression Of Flow-induced Vibrations*. International Journal of Computational Methods & Experimental Measurements. 16 pp.
- Giuliani, G., Bozzi-Pietra, S. & Donati, S. (2003). *Self-mixing laser diode vibrometer*. Meas. Sci. Technol. 24-32 pp.
- Golub, G. H. & Van Loan, C. F. (1996). *Matrix computations*. 3rd ed. ed. Johns Hopkins series in the mathematical sciences, vol. 3. Baltimore: Johns Hopkins University Press.

- 
- Guillaume, P., Verboven, P., Vanlanduit, S., Van Der Auweraer, H. & Peeters, B. (2003). *A poly-reference implementation of the least-squares complex frequency-domain estimator*. Proceedings of IMAC. 183-192 pp.
- Hoen, C. (2005). *An engineering interpretation of the complex eigensolution of linear dynamic systems*. Proceedings of International Modal Analysis Conference XXIII.
- Hsu, Y. & Pan, C. (2014). *The Static WKB Solution to Catenary Problems with Large Sag and Bending Stiffness*. Mathematical Problems in Engineering. 11 pp.
- IEA. (2014). *Key World Energy Statistics 2014*: International Energy Agency.
- Kim, B., Stubbs, N. & Park, T. (2005). *A new method to extract modal parameters using output-only responses*. J. Sound Vibr. 215-230 pp.
- Kim, Y. C. (1983). *Nonlinear vibrations of long slender beams*: Massachusetts Institute of Technology.
- Kwon, Y. W. & Bang, H. (2000). *The finite element method using MATLAB*. 2nd ed. CRC mechanical engineering series. Boca Raton, Fla: CRC Press.
- Lallement, G. & Inman, D. J. (1995). *A tutorial on complex eigenvalues*. Proceedings for SPIE - The International Society for Optical Engineering. 490-490 pp.
- Lie, H., Larsen, C. M. & Vandiver, J. K. (1997). *Vortex induced vibrations of long marine risers : model test in a rotating rig*, Trondheim: Marintek, SINTEF-gruppen.
- Lie, H. (2001). *VIV Model Test of a Catenary Riser - STRIDE Ph. 4*, Trondheim, Norway: Norwegian Marine Technology Research Institute.
- Lubbad, R. & Moe, G. (2008). *Closed-form solutions for vibrations of nearly vertical strings and beams by means of asymptotic methods*. Journal of Engineering Mechanics. 1064-1070 pp.
- Lubbad, R. K., Moe, G. & Niedzwecki, J. M. (2011). *Frequency and Mode Shape Estimates of Marine Catenary Systems using Asymptotic Approximations*. Trondheim: NTNU. 23 pp.
- Moe, G. & Arntsen, Ø. A. (2001). *An analytic model for static analysis of catenary risers*. Cupertino, Calif.: International Society of Offshore and Polar Engineers.
- Moe, G., Teigen, T. r., Simantiras, P., Willis, N. & Lie, H. (2004). *Predictions and Model Tests of an SCR Undergoing VIV in Flow at Oblique Angles*. ASME 2004 23rd International Conference on Offshore Mechanics and Arctic Engineering: American Society of Mechanical Engineers. 1023-1034 pp.
- Newland, D. E. (2005). *An introduction to random vibrations, spectral & wavelet analysis*. 3rd ed. Mineola, N.Y: Dover.
-

- 
- Niedzwecki, J. M. & Moe, G. (2005). *Investigation of a catenary riser undergoing VIV*. WIT Conference of Fluid Structure Interaction. 8 pp.
- Niedzwecki, J. M. & Moe, G. (2007). *Development of SCR VIV in a changing flow field*. WIT Conference Fluid Structure Interaction and Moving Boundary Problems IV. 10 pp.
- Rainieri, C., Fabbrocino, G. & SpringerLink. (2014). *Operational Modal Analysis of Civil Engineering Structures: An Introduction and Guide for Applications*. New York, NY: Springer New York Imprint: Springer.
- Reynders, E., Schevenels, M. & De Roeck, G. (2014). *MACEC 3.3: A matlab toolbox for experimental and operational modal analysis*, Leuven, Belgium: Faculty of Engineering, Department of Civil Engineering, Structural Mechanics Section.
- Triantafyllou, M. S., Bliet, A. & Hyunkyung, S. (1985). *Dynamic analysis as a tool for open-sea mooring system design*. Transactions-Society of Naval Architects and Marine Engineers. 303-324 pp.





---

# Appendix A

## Task Description

### **Background**

A wide range of offshore science and engineering applications utilize slender catenary-shaped structural elements in their design. These applications include moorings and steel catenary riser designs. The susceptibility of these slender catenary-shapes to vortex-induced vibrations remains the subject of theoretical, numerical and experimental studies.

### **Task**

The research for this Master thesis will start by analyzing experimental data selected from a model test program of a towed catenary model. The multi-modal cross-flow response behavior of the catenary model will be investigated. The natural frequencies and the corresponding mode-shapes of the catenary model will be calculated analytically and numerically. The accuracy of the eigenvalue calculations will be established through comparison with experimental data. Finally, modal analysis techniques will be applied in an attempt to analytically reconstruct the measured response of the catenary model.

### **Task description**

- Literature study
- Numerical modelling of catenary dynamics
- Validation of numerical model with available measurement data
- System identification

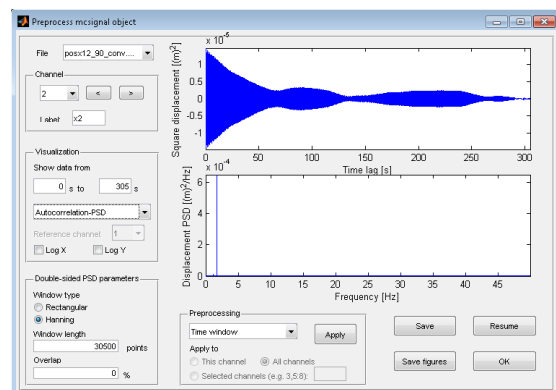


# Appendix B

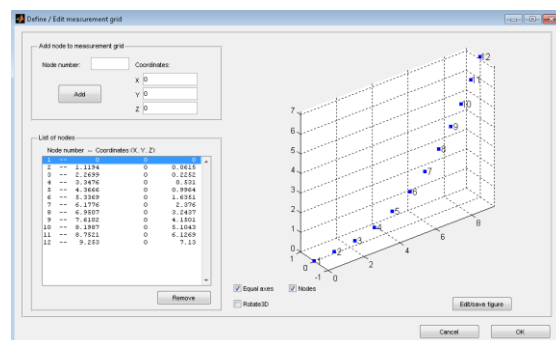
## Step-by-step MACEC procedure

The following presents the step-by-step method used to analyze the case study data in the commercial Matlab toolbox MACEC.

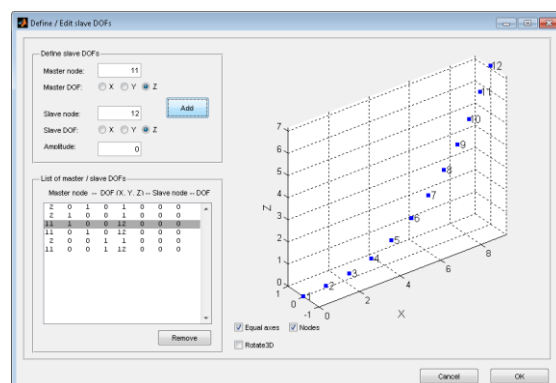
- Import acceleration or displacement measurements. Convert to mcsignal.
- Process the data by applying necessary filters, windows or detrending. A Hanning window is used to remove any transient parts of the time-series.



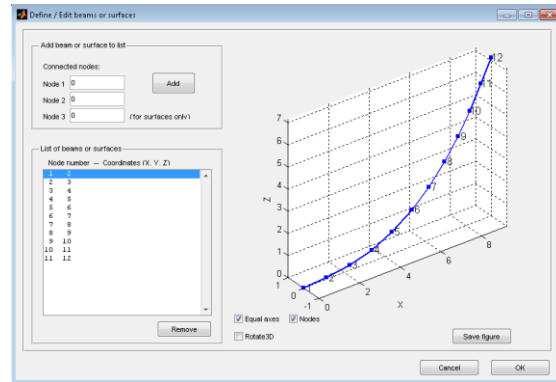
- Create a geometry by producing a grid of nodes. The positions of the nodes are based on the node geometry found by the static analysis in DeepC.



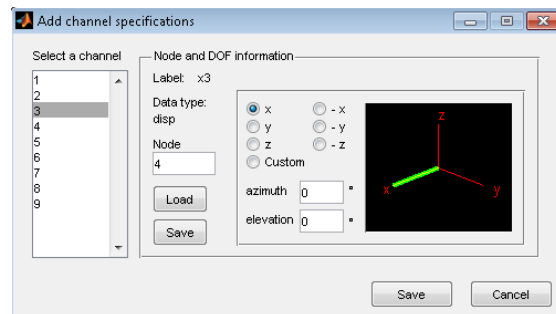
- Specify slave nodes. For this thesis this implies specifying that nodes 1 and 12 are fixed in all directions by slaving to neighboring nodes with amplification 0.



- Define beams or surfaces between nodes.



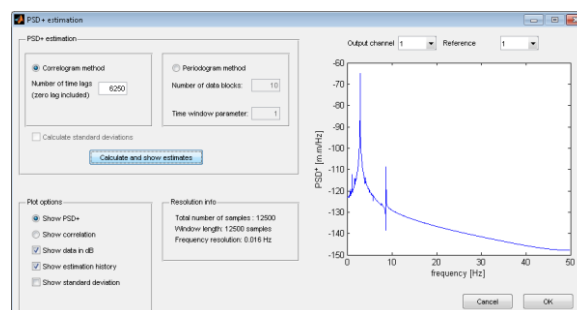
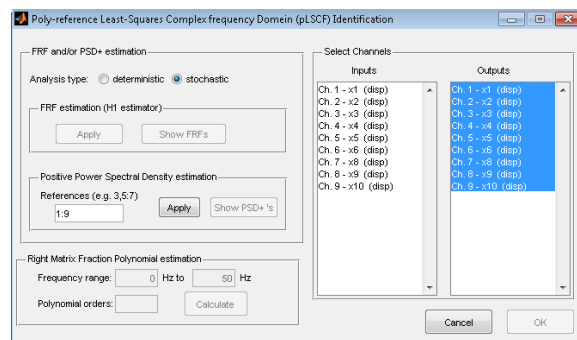
- Specify connection between signal and nodal DOFs.



A mcsignal proc file is now ready to follow steps of the signal processing techniques

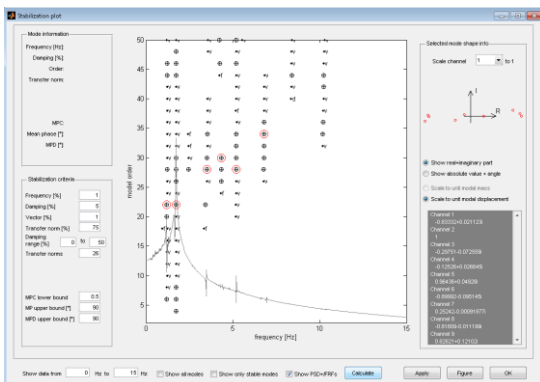
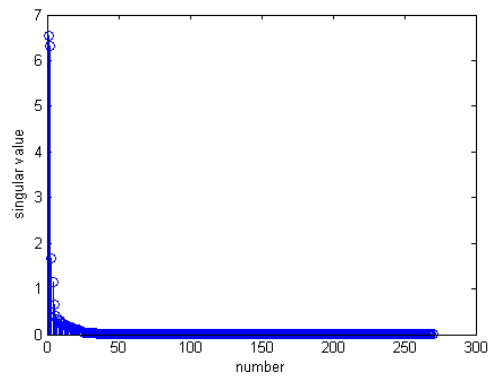
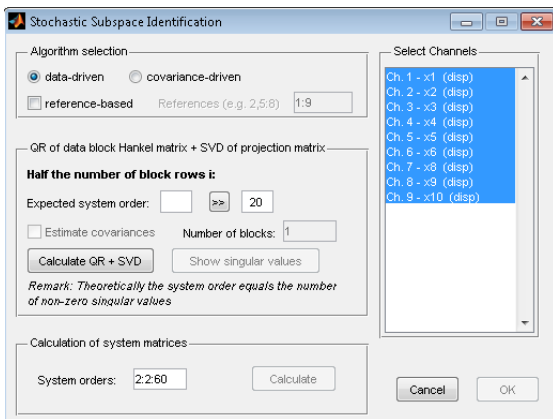
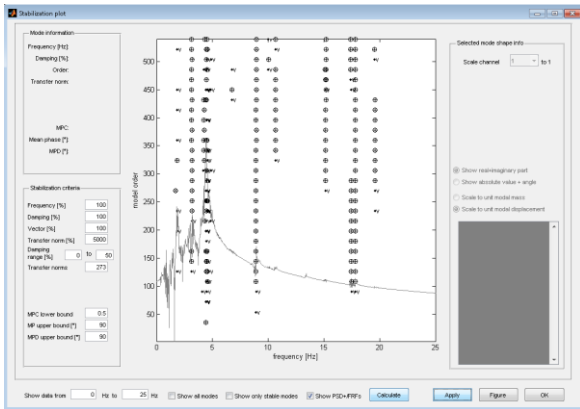
Processing of the data is based on the theory of the methods given in Section 4.3.

- pLSCF
  - Specify the output channels to be used for the calculation of auto- and cross PSDs.
  - Specify the expected order of the polynomials. Run the modal analysis using the method, and identify the modes in the stabilization diagram. The stabilization criteria may be too strict, and can be modified to allow for more stable poles.



- DD-SSI/ Cov-SSI

Select all channels to be used. Specify expected model order, which is the expected number of singular values. For the example SVD diagram shown to the right, a natural number of system order would be about 50, but a higher order could be specified to increase the solutions of the algorithms. The two methods of calculating poles are run separately, and their resulting stabilization diagrams are used to identify natural frequencies. As for p-LSCF, the stabilization criteria can be modified if needed.





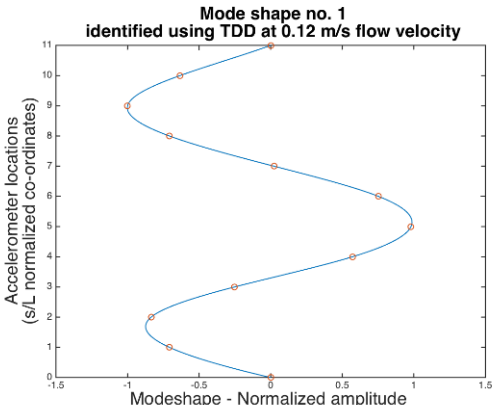
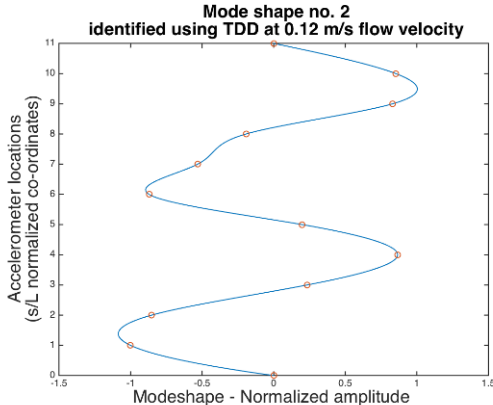
# Appendix C

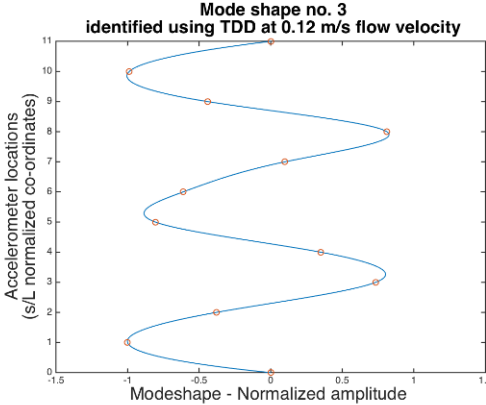
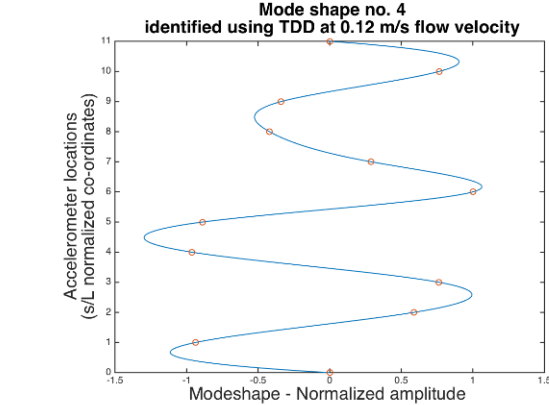
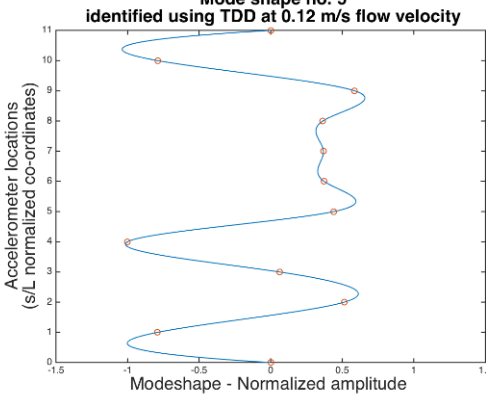
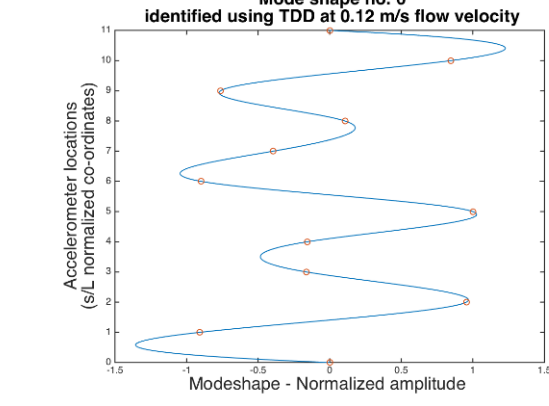
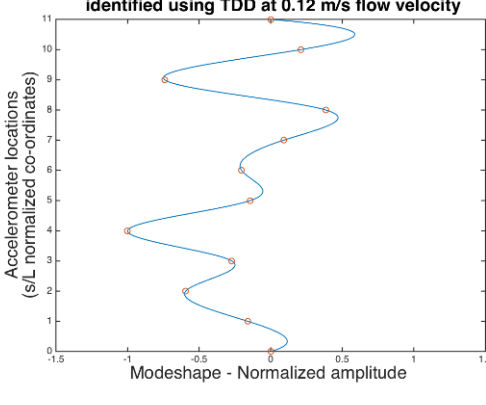
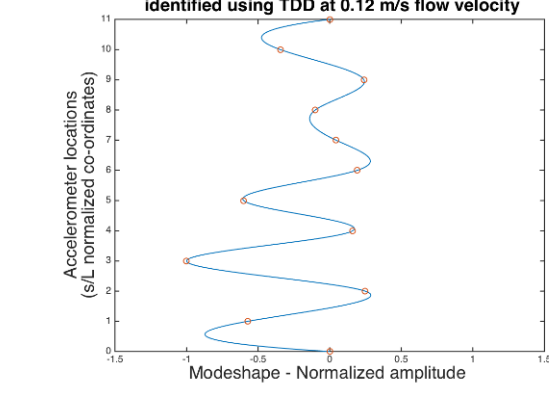
## The TDD Method Results

This appendix summarizes the results obtained by the TDD method with the three different flow velocity cases. The results are sorted by the sequential step that they were identified, and show the estimated natural frequency, estimated damping ratio and a spline fit mode shape. The values at accelerometer location no. 7 are linearly interpolated values.

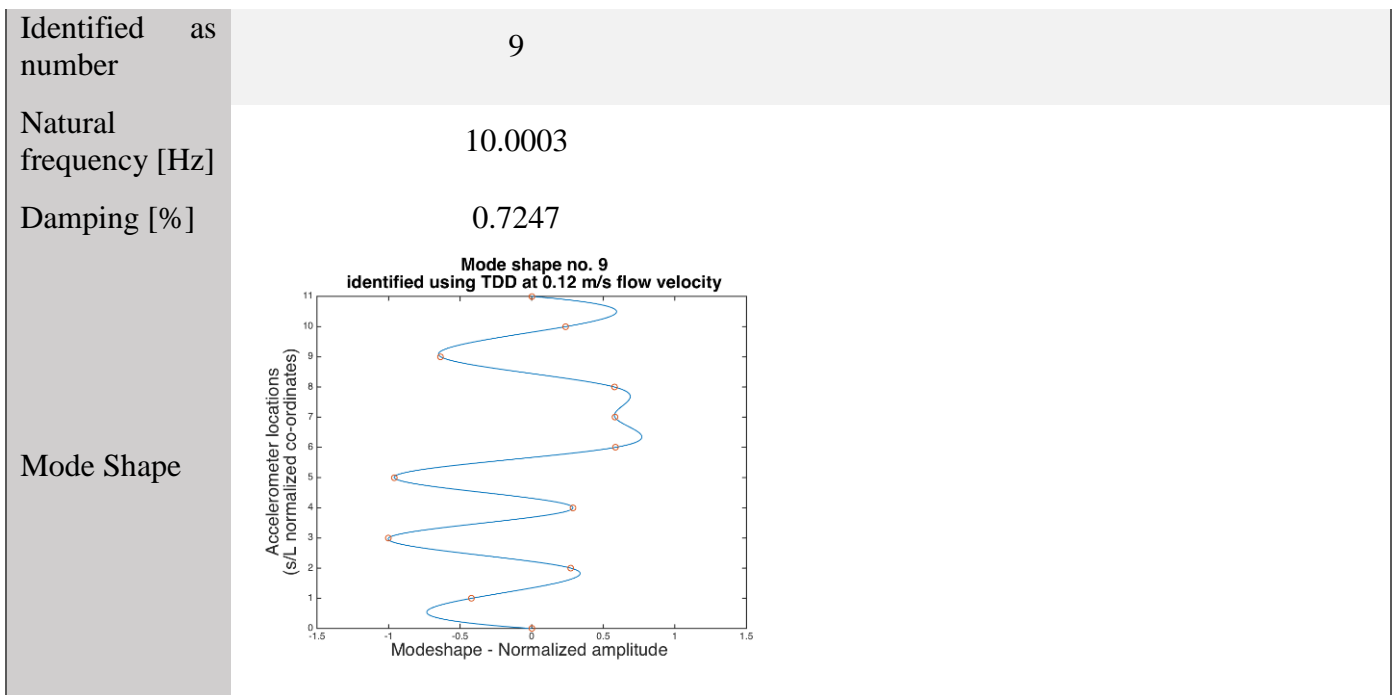
### C.1 0.12 m/s

Table C 1: Results from TDD method, 0.12 m/s flow velocity

|                        |   |  |
|------------------------|---|--|
| Identified as number   | 1   | 2  |
| Natural frequency [Hz] | 1.1906  | 1.7241   |
| Damping [%]            | 1.2208  | 0.2491   |
| Mode Shape             |  |  |
| Identified as number   | 3   | 4  |
| Natural frequency [Hz] | 2.7032  | 3.5714   |
| Damping [%]            | 1.8400  | 0.0860   |

|                        |   |  |
|------------------------|---|--|
| Mode Shape             |    |    |
| Identified as number   | 5   | 6  |
| Natural frequency [Hz] | 5.2632  | 6.6667   |
| Damping [%]            | 0.2100  | 0.2664   |
| Mode Shape             |   |   |
| Identified as number   | 7   | 8  |
| Natural frequency [Hz] | 8.3333  | 9.0913   |
| Damping [%]            | 0.3501  | 0.9720   |
| Mode Shape             |  |  |





Identified peaks with irregular mode-shapes (possible modes with unfortunate accelerometer spacing).

|        |        |         |         |         |
|--------|--------|---------|---------|---------|
| 1      | 2      | 3       | 4       | 5       |
| 0.5714 | 7.6922 | 11.1111 | 14.2858 | 16.6668 |

Figure C 1 shows the correlations between mode shapes according to the description given in section 5.3.1.1.

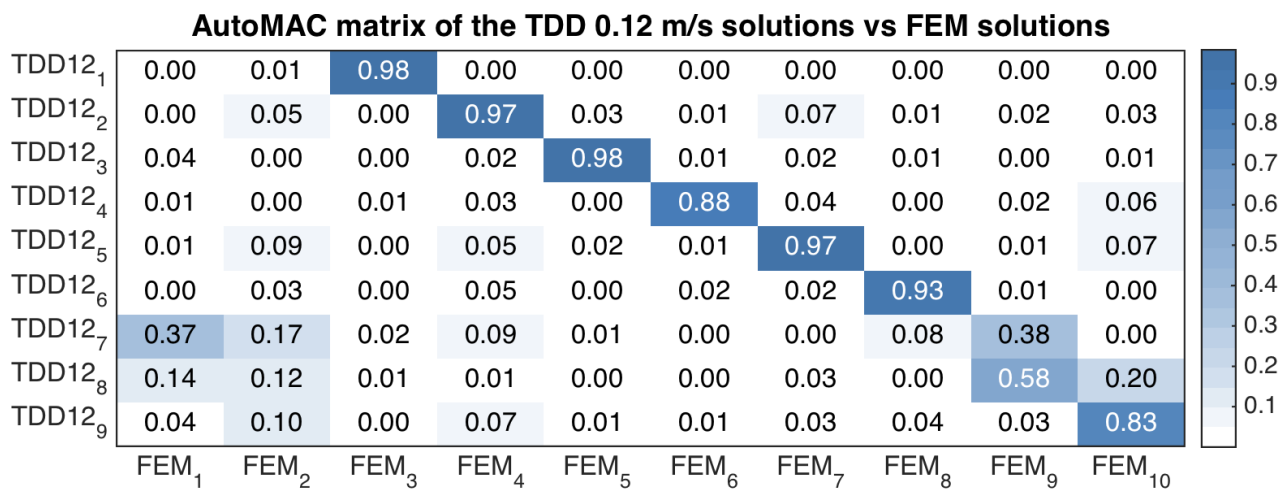
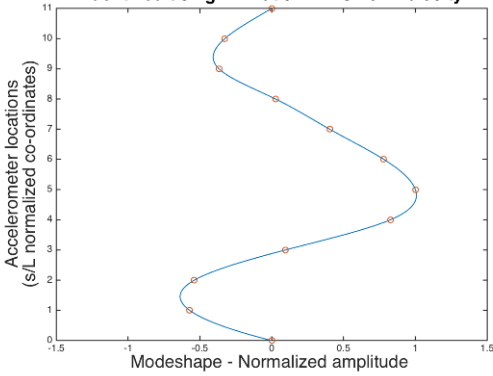
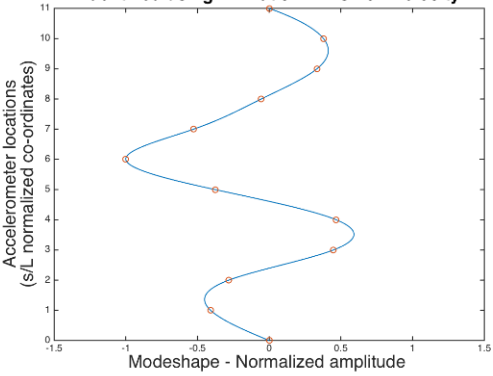
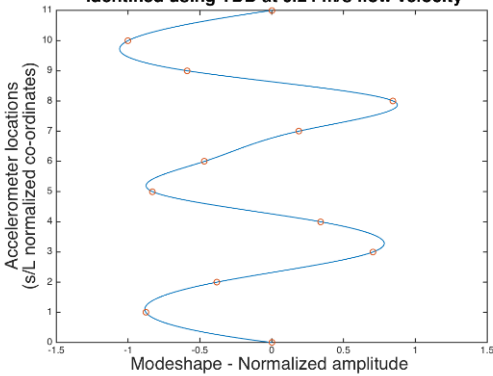
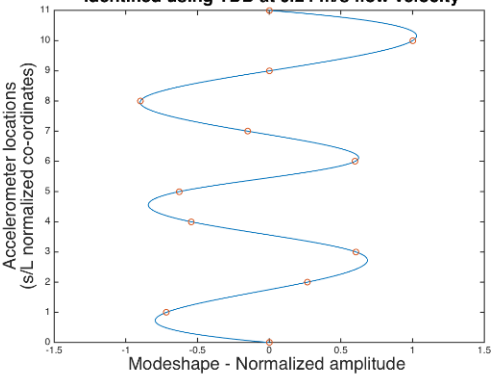
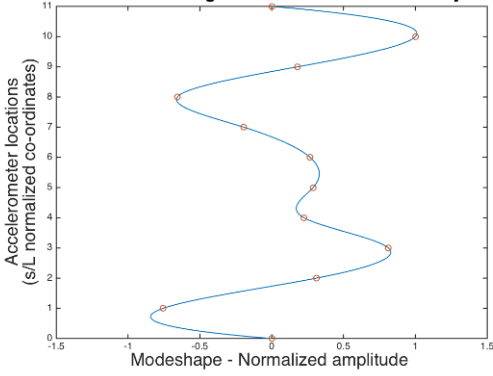
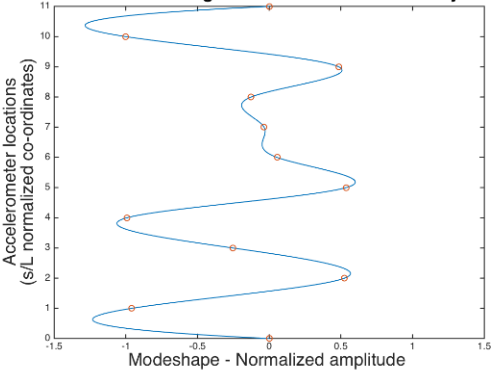
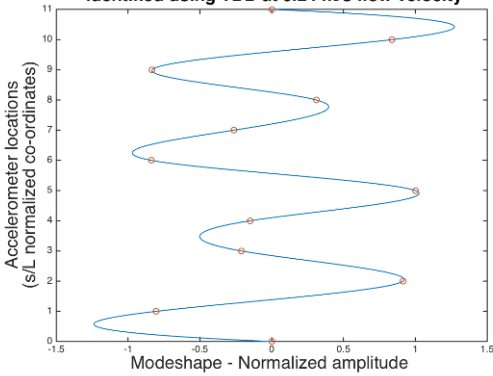
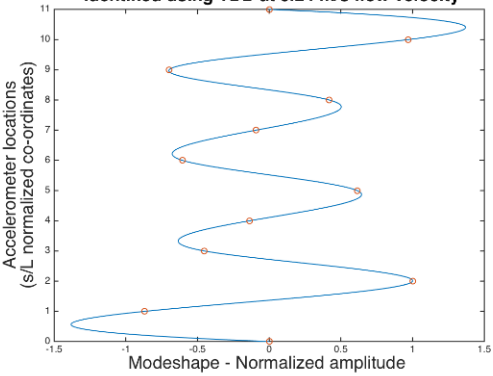


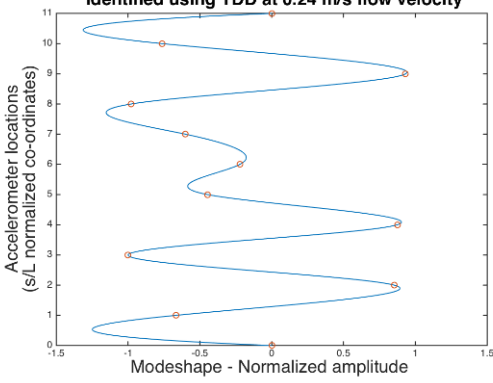
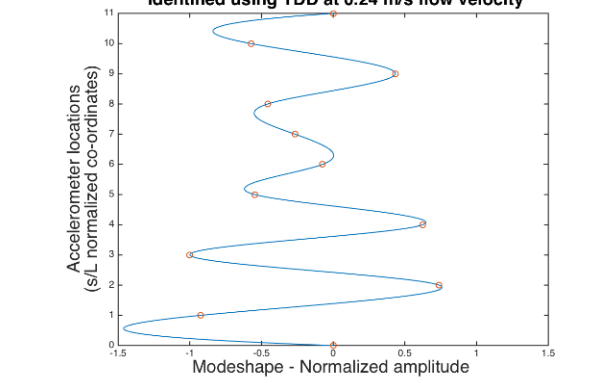
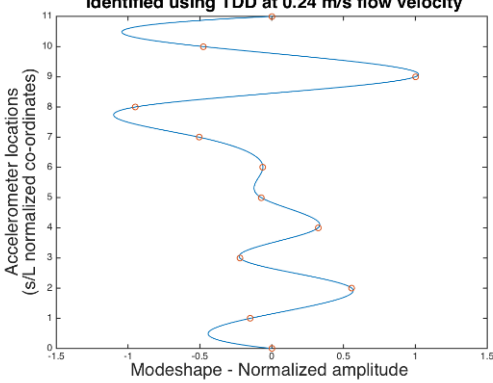
Figure C 1: MAC matrix for TDD method obtained mode shapes, 0.12 m/s current velocity

## C.2 0.24 m/s

Table C 2: Results from TDD method, 0.24 m/s flow velocity

|                        |  |   |
|------------------------|--|---|
| Identified as number   | 1  | 2   |
| Natural frequency [Hz] | 1.1111   | 1.7862  |
| Damping                | 0.7282   | 2.3154  |
| Mode Shape             | <p>Mode shape no. 1<br/>identified using TDD at 0.24 m/s flow velocity</p>   | <p>Mode shape no. 2<br/>identified using TDD at 0.24 m/s flow velocity</p>   |
| Identified as number   | 3  | 4   |
| Natural frequency [Hz] | 2.8572   | 4.1670  |
| Damping [%]            | 0.1011   | 1.1641  |
| Mode Shape             | <p>Mode shape no. 3<br/>identified using TDD at 0.24 m/s flow velocity</p>  | <p>Mode shape no. 4<br/>identified using TDD at 0.24 m/s flow velocity</p>  |

|                        |  |   |
|------------------------|--|---|
| Identified as number   | 5  | 6   |
| Natural frequency [Hz] | 5.0026   | 5.8824  |
| Damping [%]            | 3.2423   | 0.0695  |
| Mode Shape             | <p>Mode shape no. 5<br/>identified using TDD at 0.24 m/s flow velocity</p>    | <p>Mode shape no. 6<br/>identified using TDD at 0.24 m/s flow velocity</p>    |
| Identified as number   | 7  | 8   |
| Natural frequency [Hz] | 6.6667   | 7.6922  |
| Damping [%]            | 0.2212   | 0.1071  |
| Mode Shape             | <p>Mode shape no. 7<br/>identified using TDD at 0.24 m/s flow velocity</p>  | <p>Mode shape no. 8<br/>identified using TDD at 0.24 m/s flow velocity</p>  |
| Identified as number   | 9  | 10  |
| Natural frequency [Hz] | 8.3333   | 9.0913  |
| Damping [%]            | 0.2371   | 1.0120  |

|                        |  |  |
|------------------------|--|--|
| Mode Shape             |   |  |
| Identified as number   | 11   |  |
| Natural frequency [Hz] | 10.0000  |  |
| Damping [%]            | 0.0180   |  |
| Mode Shape             |  |  |

Identified peaks with irregular mode-shapes (possible modes with unfortunate accelerometer spacing)

|         |         |         |
|---------|---------|---------|
| 1       | 2       | 3       |
| 12.5000 | 14.2858 | 16.6668 |

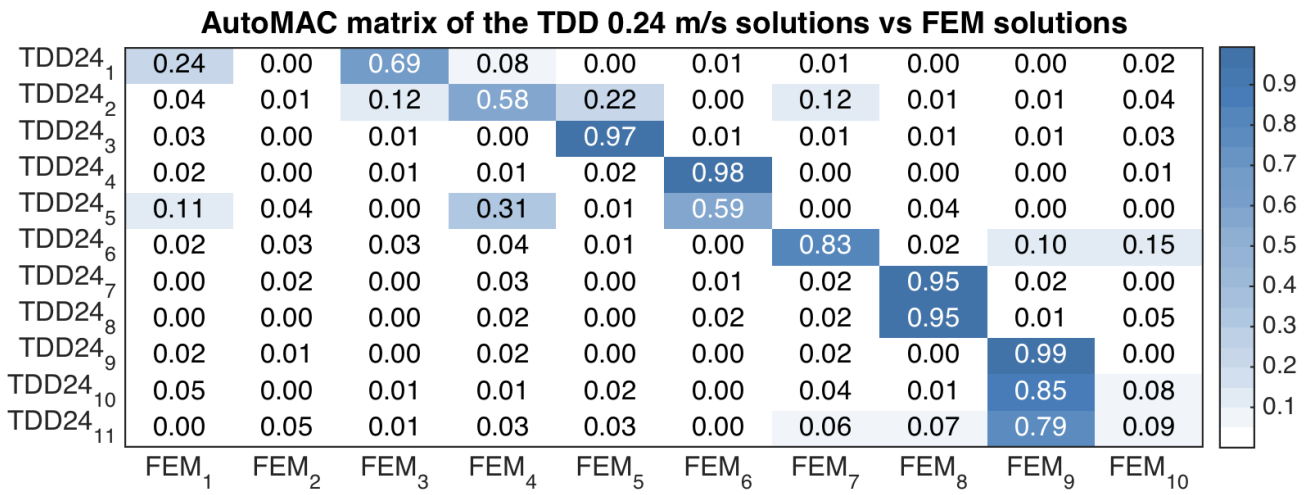
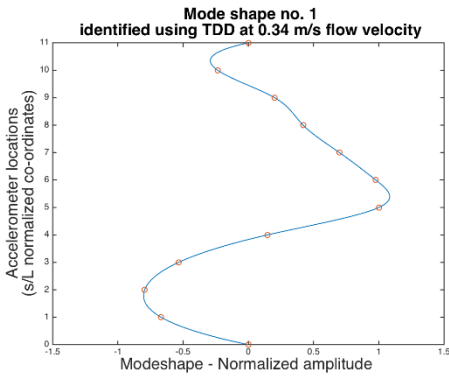
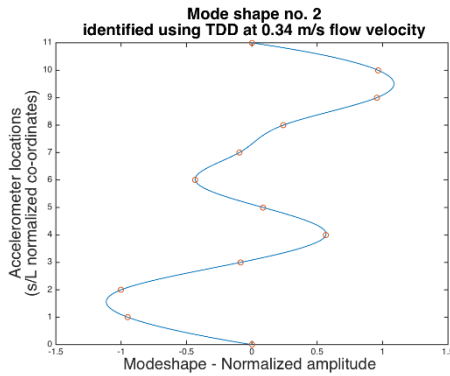
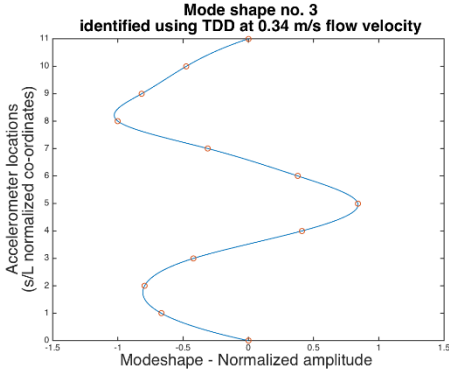
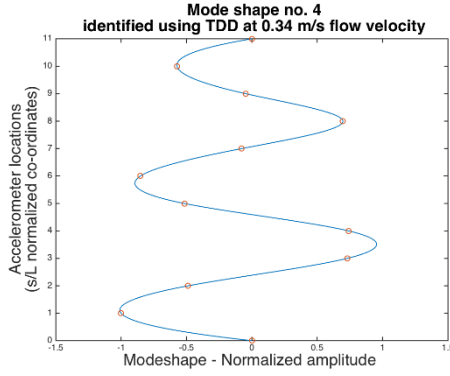
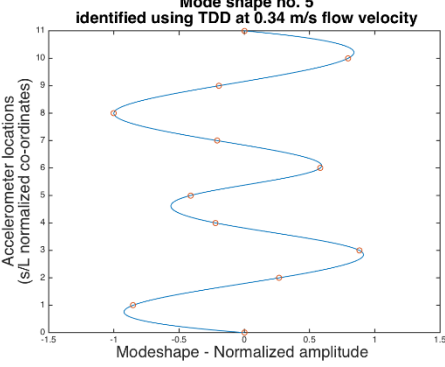
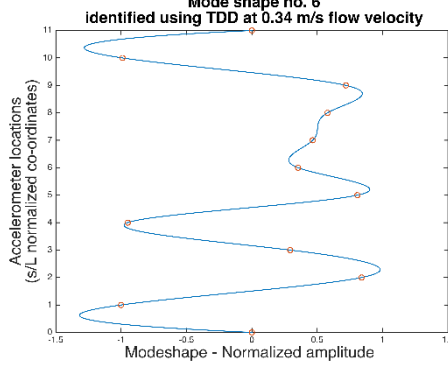
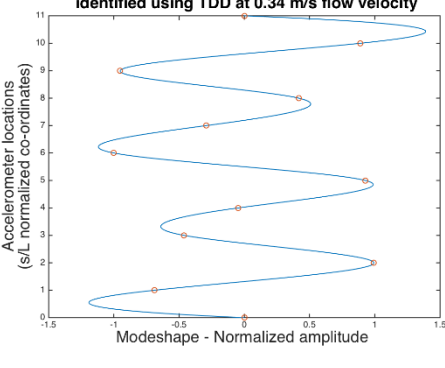
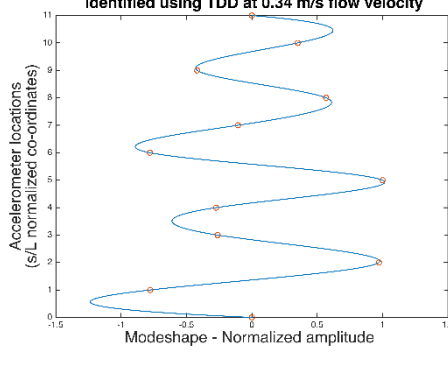
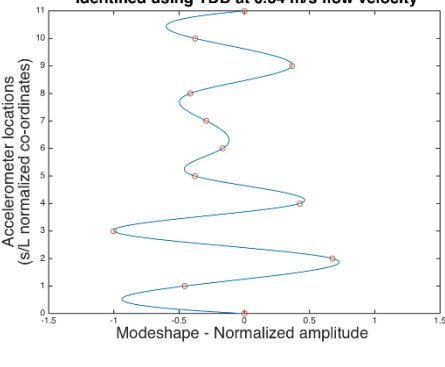
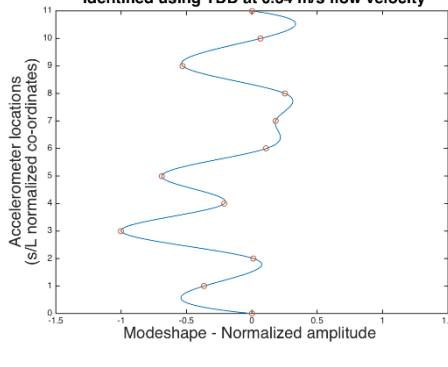


Figure C 2: MAC matrix for TDD method obtained mode shapes, 0.24 m/s current velocity

## C.3 0.34 m/s

Table C 3: Results from TDD method, 0.34 m/s flow velocity

|                        |   |  |
|------------------------|---|--|
| Identified as number   | 1   | 2  |
| Natural frequency [Hz] | 0.9531  | 1.3896   |
| Damping [%]            | 4.0056  | 3.1552   |
| Mode Shape             |   |   |
| Identified as number   | 3   | 4  |
| Natural frequency [Hz] | 1.7858  | 2.7029   |
| Damping [%]            | 0.8758  | 1.2588   |
| Mode Shape             |  |  |
| Identified as number   | 5   | 6  |
| Natural frequency [Hz] | 4.3479  | 5.5557   |
| Damping [%]            | 0.4468  | 0.6812   |

|                        |  |  |
|------------------------|--|--|
| Mode Shape             |  <p>Mode shape no. 5<br/>identified using TDD at 0.34 m/s flow velocity</p>   |  <p>Mode shape no. 6<br/>identified using TDD at 0.34 m/s flow velocity</p>    |
| Identified as number   | 7  | 8  |
| Natural frequency [Hz] | 6.6669   | 7.6924   |
| Damping [%]            | 0.8195   | 0.5254   |
| Mode Shape             |  <p>Mode shape no. 7<br/>identified using TDD at 0.34 m/s flow velocity</p>  |  <p>Mode shape no. 8<br/>identified using TDD at 0.34 m/s flow velocity</p>   |
| Identified as number   | 9  | 10   |
| Natural frequency [Hz] | 9.0909   | 10.0001  |
| Damping [%]            | 0.1590   | 0.6119   |
| Mode Shape             |  <p>Mode shape no. 9<br/>identified using TDD at 0.34 m/s flow velocity</p> |  <p>Mode shape no. 10<br/>identified using TDD at 0.34 m/s flow velocity</p> |

Identified peaks with irregular mode-shapes (possible modes with unfortunate accelerometer spacing)

|         |         |         |         |         |         |
|---------|---------|---------|---------|---------|---------|
| 1       | 2       | 3       | 4       | 5       | 6       |
| 11.1111 | 12.5000 | 14.2858 | 16.6668 | 20.0003 | 25.0006 |

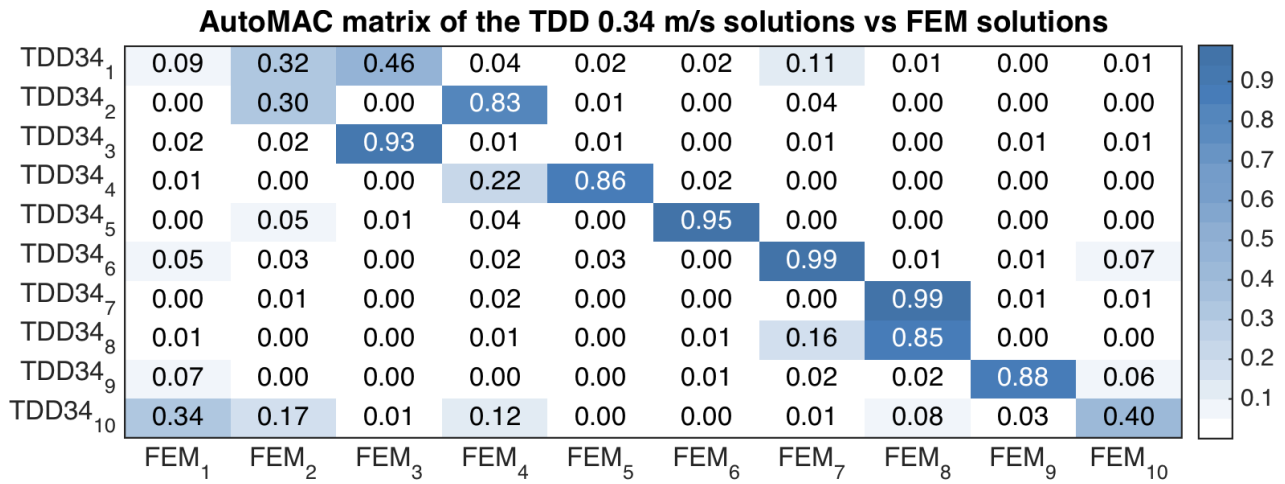


Figure C 3: MAC matrix for TDD method obtained mode shapes, 0.34 m/s current velocity



---

# Appendix D

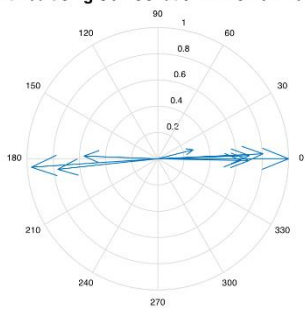
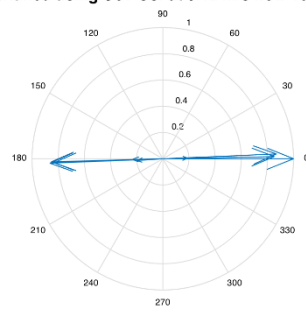
## The MACEC Method Results

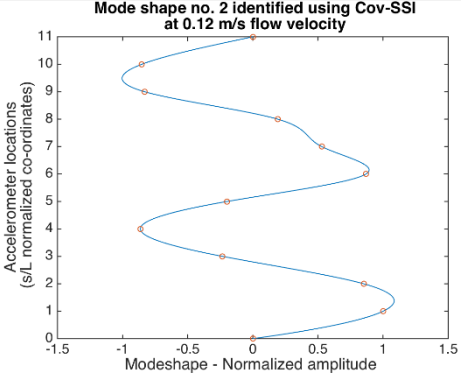
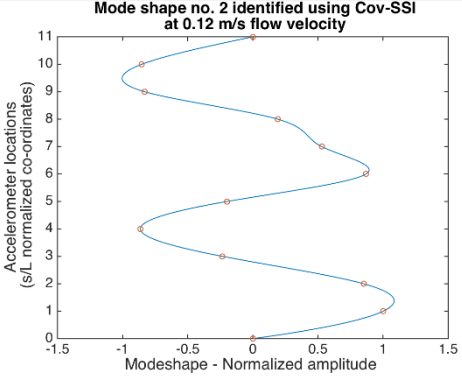
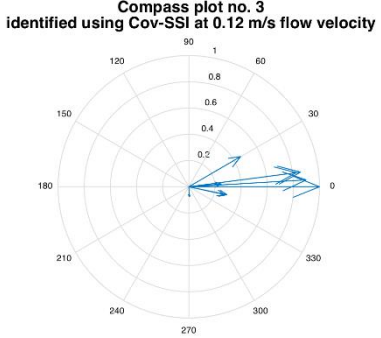
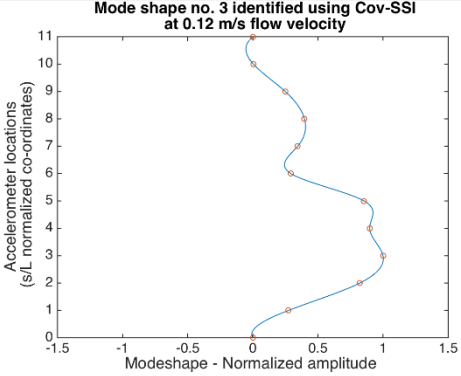
This appendix summarizes the results obtained by the methods available in the Matlab toolbox MACEC using the three different flow velocity cases. The results are sorted by the sequential step that they were identified, and show the estimated natural frequency, estimated damping ratio and a spline fit mode shape. The values at accelerometer location no. 7 are linearly interpolated values.

### D.1 Covariance driven SSI

#### D.1.1 0.12 m/s

*Table D 1: Results from Cov-SSI method, 0.12 m/s flow velocity*

| Identified as number   | 1   | 2   |
|------------------------|---|---|
| Complex plot           |  |  |
| Natural frequency [Hz] | 1.2004  | 1.7290  |
| Damping [%]            | 1.9587  | 0.0431  |

|                        |   |  |
|------------------------|---|--|
| Mode Shape             |    |  |
| Identified as number   | 3   |  |
| Complex plot           |   |  |
| Natural frequency [Hz] | 4.3263  |  |
| Damping [%]            | 10.0640   |  |
| Mode Shape             |  |  |

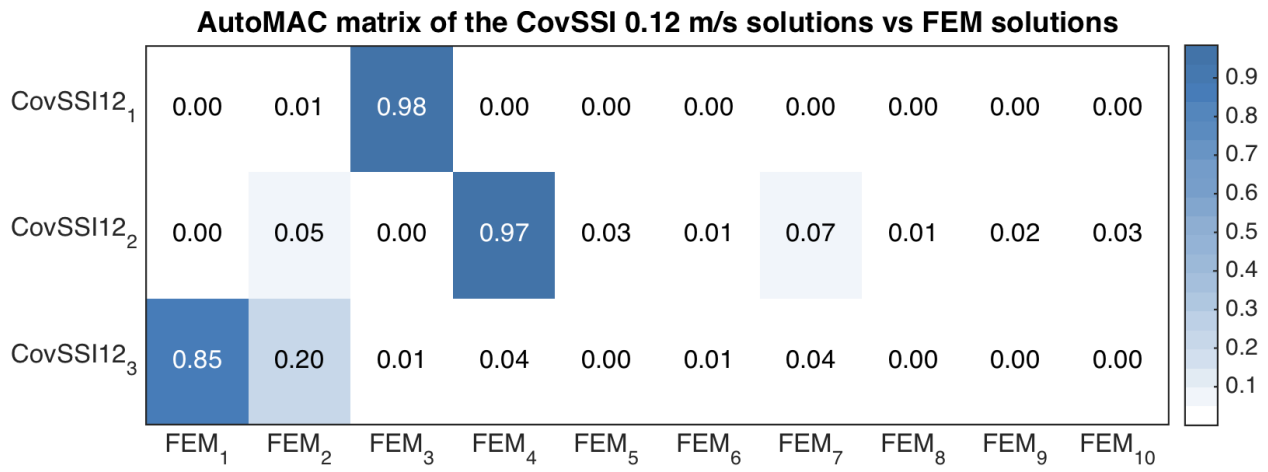


*Figure D 1: MAC matrix for Cov-SSI method obtained mode shapes, 0.12 m/s current velocity*

D.1.2 0.24 m/s

Table D 2: Results from Cov-SSI method, 0.24 m/s flow velocity

| Identified as number   | 1  | 2  |
|------------------------|--|--|
| Complex plot           | <p>Compass plot no. 1 identified using Cov-SSI at 0.24 m/s flow velocity</p> | <p>Compass plot no. 2 identified using Cov-SSI at 0.24 m/s flow velocity</p> |
| Natural frequency [Hz] | 1.1603   | 2.8984   |
| Damping [%]            | 16.1109  | 0.0391   |
| Mode Shape             | <p>Mode shape no. 1 identified using Cov-SSI at 0.24 m/s flow velocity</p>   | <p>Mode shape no. 2 identified using Cov-SSI at 0.24 m/s flow velocity</p>   |
| Identified as number   | 3  |  |
| Complex plot           | <p>Compass plot no. 3 identified using Cov-SSI at 0.24 m/s flow velocity</p> |  |
| Natural frequency [Hz] | 8.6945   |  |

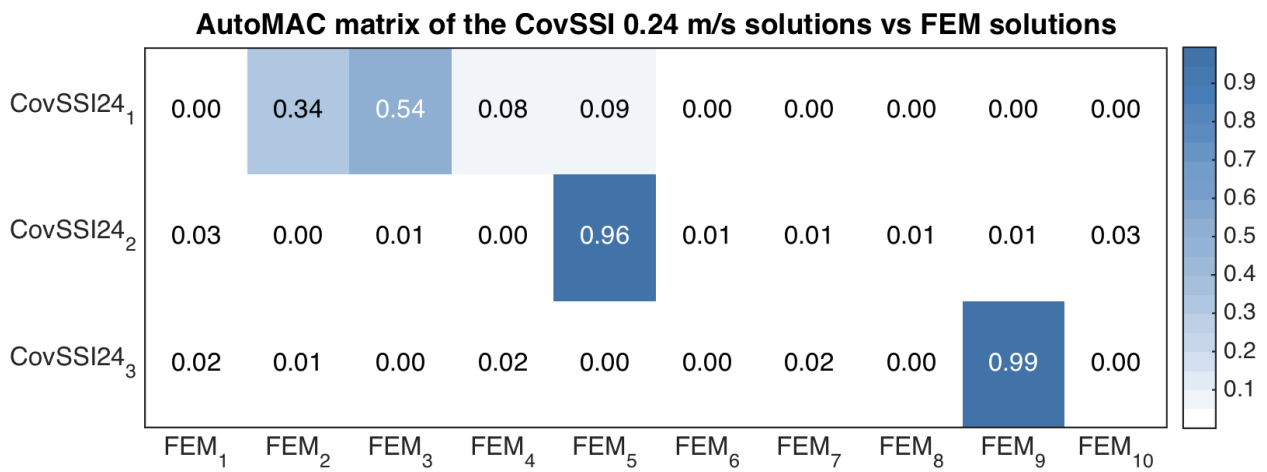
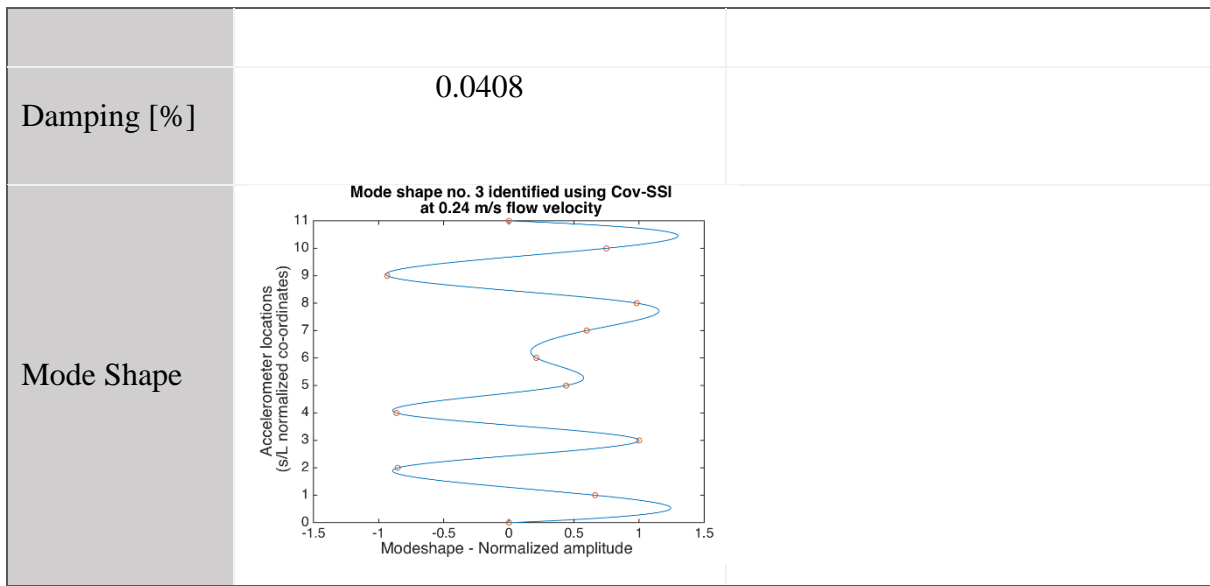


Figure D 2: MAC matrix for Cov-SSI method obtained mode shapes, 0.24 m/s current velocity

D.1.3 0.34 m/s

Table D 3: Results from Cov-SSI method, 0.34 m/s flow velocity

| Identified as number   | 1  | 2  |
|------------------------|--|--|
| Complex plot           | <p>Compass plot no. 1 identified using Cov-SSI at 0.34 m/s flow velocity</p> | <p>Compass plot no. 2 identified using Cov-SSI at 0.34 m/s flow velocity</p> |
| Natural frequency [Hz] | 4.4764   | 8.8920   |
| Damping [%]            | 0.0568   | 0.5618   |
| Mode Shape             | <p>Mode shape no. 1 identified using Cov-SSI at 0.34 m/s flow velocity</p>   | <p>Mode shape no. 2 identified using Cov-SSI at 0.34 m/s flow velocity</p>   |
| Identified as number   | 3  |  |
| Complex plot           | <p>Compass plot no. 3 identified using Cov-SSI at 0.34 m/s flow velocity</p> |  |
| Natural frequency [Hz] | 17.6407  |  |

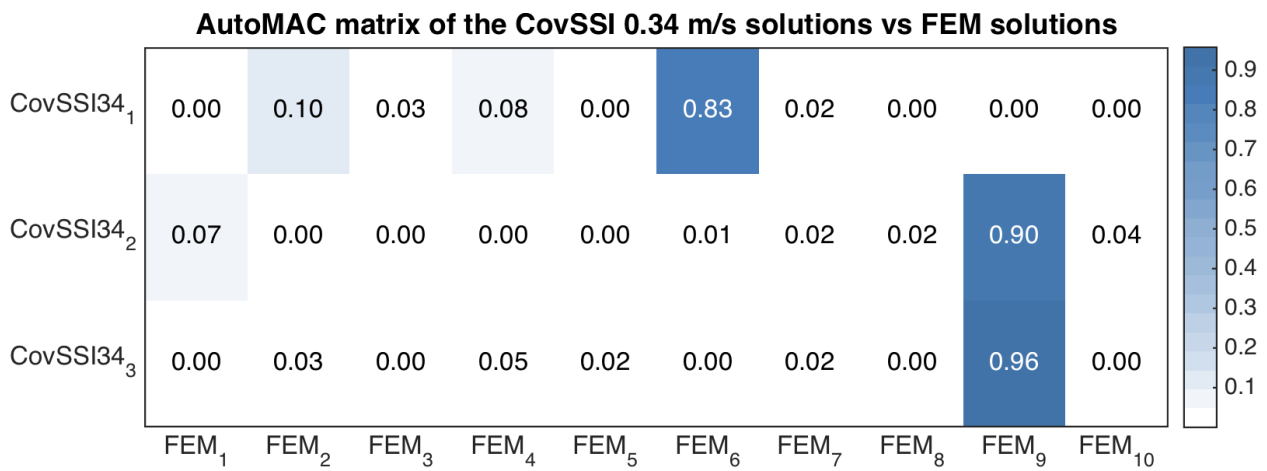
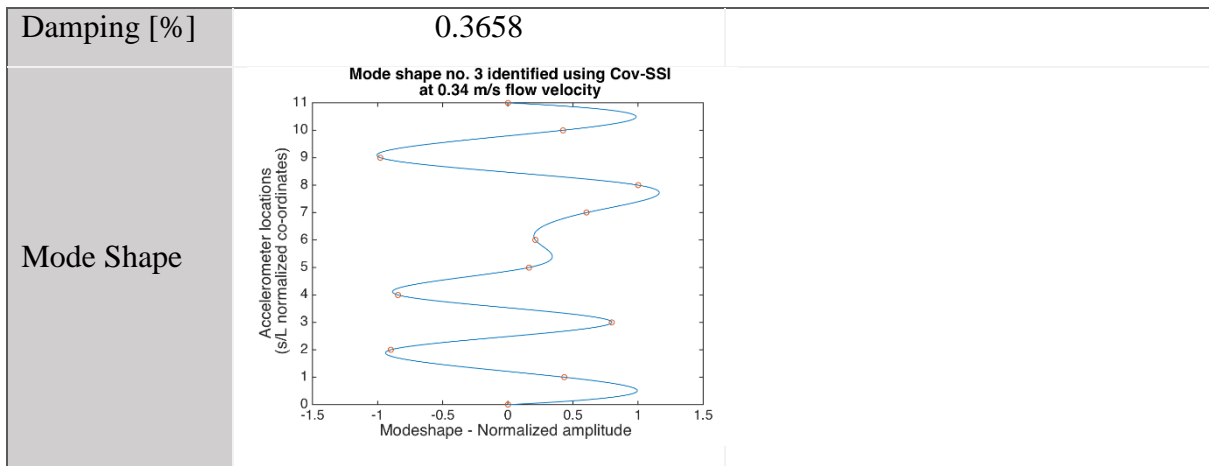


Figure D 3: MAC matrix for Cov-SSI method obtained mode shapes, 0.34 m/s current velocity

## D.2 Data-driven SSI

### D.2.1 0.12 m/s

Table D 4: Results from DD-SSI method, 0.12 m/s flow velocity

| Identified as number   | 1   | 2   |
|------------------------|---|---|
| Complex plot           | <p>Compass plot no. 1<br/>identified using DD-SSI at 0.12 m/s flow velocity</p> | <p>Compass plot no. 2<br/>identified using DD-SSI at 0.12 m/s flow velocity</p> |
| Natural frequency [Hz] | 1.2023  | 1.7288  |
| Damping [%]            | 1.2754  | 0.0175  |
| Mode Shape             | <p>Mode shape no. 1 identified using DD-SSI at 0.12 m/s flow velocity</p>       | <p>Mode shape no. 2 identified using DD-SSI at 0.12 m/s flow velocity</p>       |



|                        |   |   |
|------------------------|---|---|
| Identified as number   | 3   | 4   |
| Complex plot           | <p>Compass plot no. 3 identified using DD-SSI at 0.12 m/s flow velocity</p> | <p>Compass plot no. 4 identified using DD-SSI at 0.12 m/s flow velocity</p> |
| Natural frequency [Hz] | 3.5127  | 4.3449  |
| Damping [%]            | 0.7920  | 6.0561  |
| Mode Shape             | <p>Mode shape no. 3 identified using DD-SSI at 0.12 m/s flow velocity</p>   | <p>Mode shape no. 4 identified using DD-SSI at 0.12 m/s flow velocity</p>   |
| Identified as number   | 5   | 6   |
| Complex plot           | <p>Compass plot no. 5 identified using DD-SSI at 0.12 m/s flow velocity</p> | <p>Compass plot no. 6 identified using DD-SSI at 0.12 m/s flow velocity</p> |
| Natural frequency [Hz] | 5.2018  | 6.8024  |
| Damping [%]            | 0.2705  | 0.1845  |

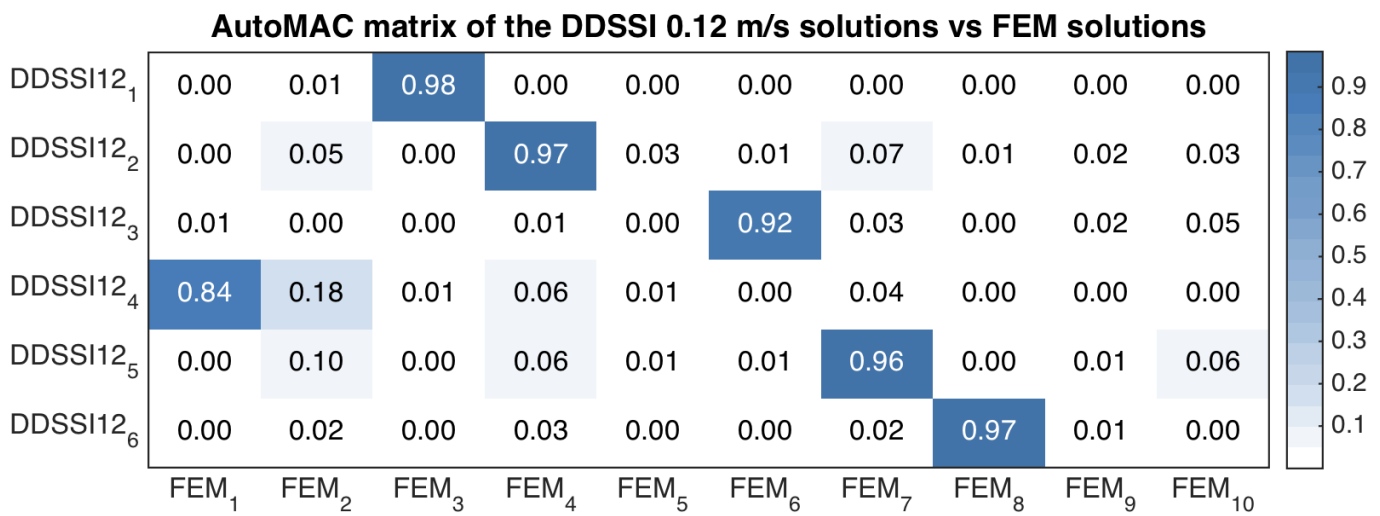
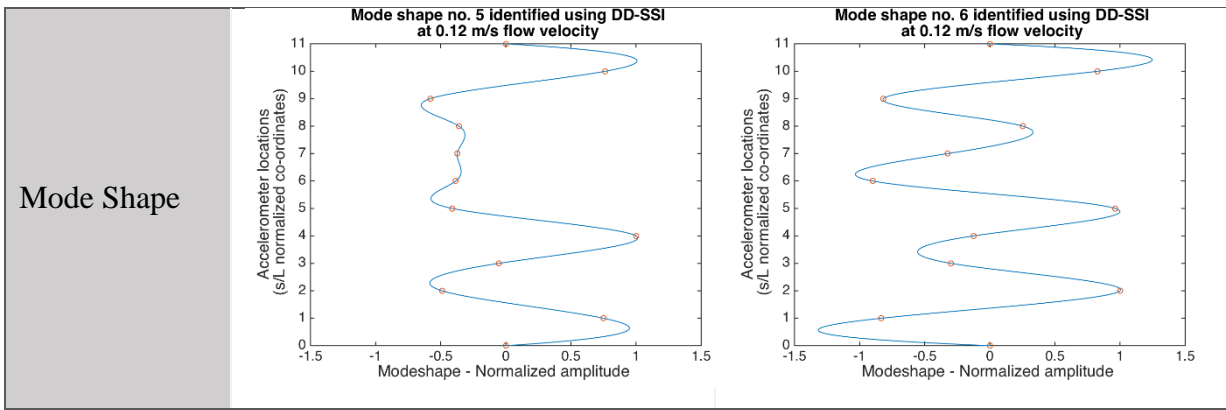
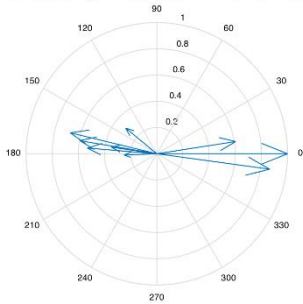
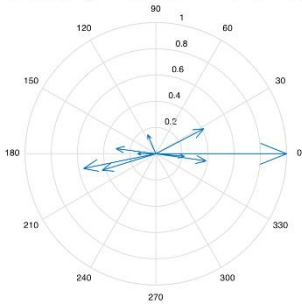
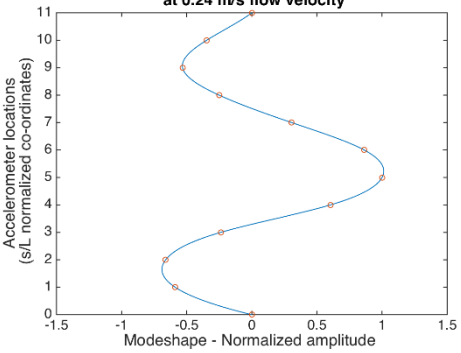
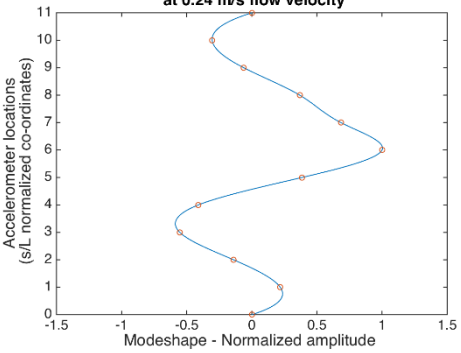
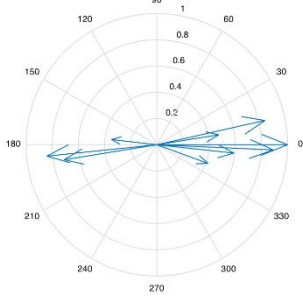
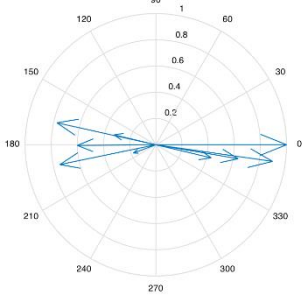
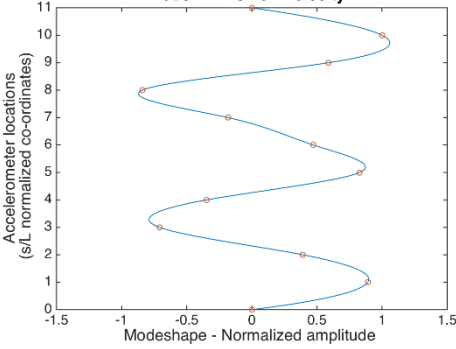
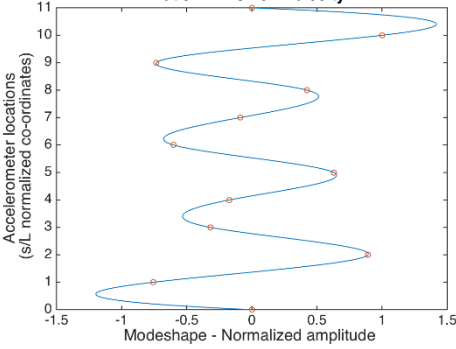
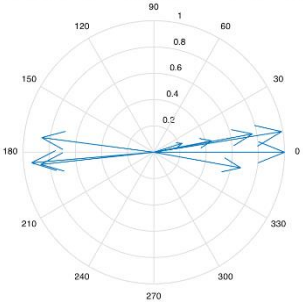
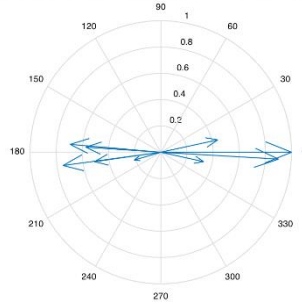
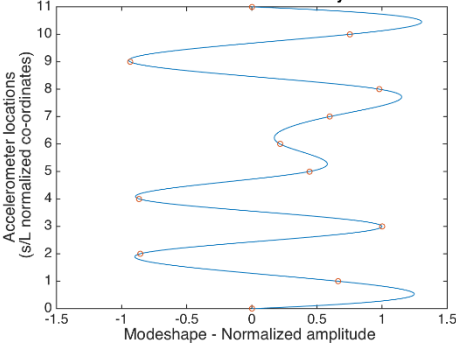
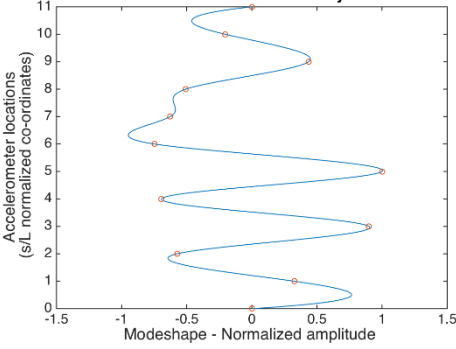


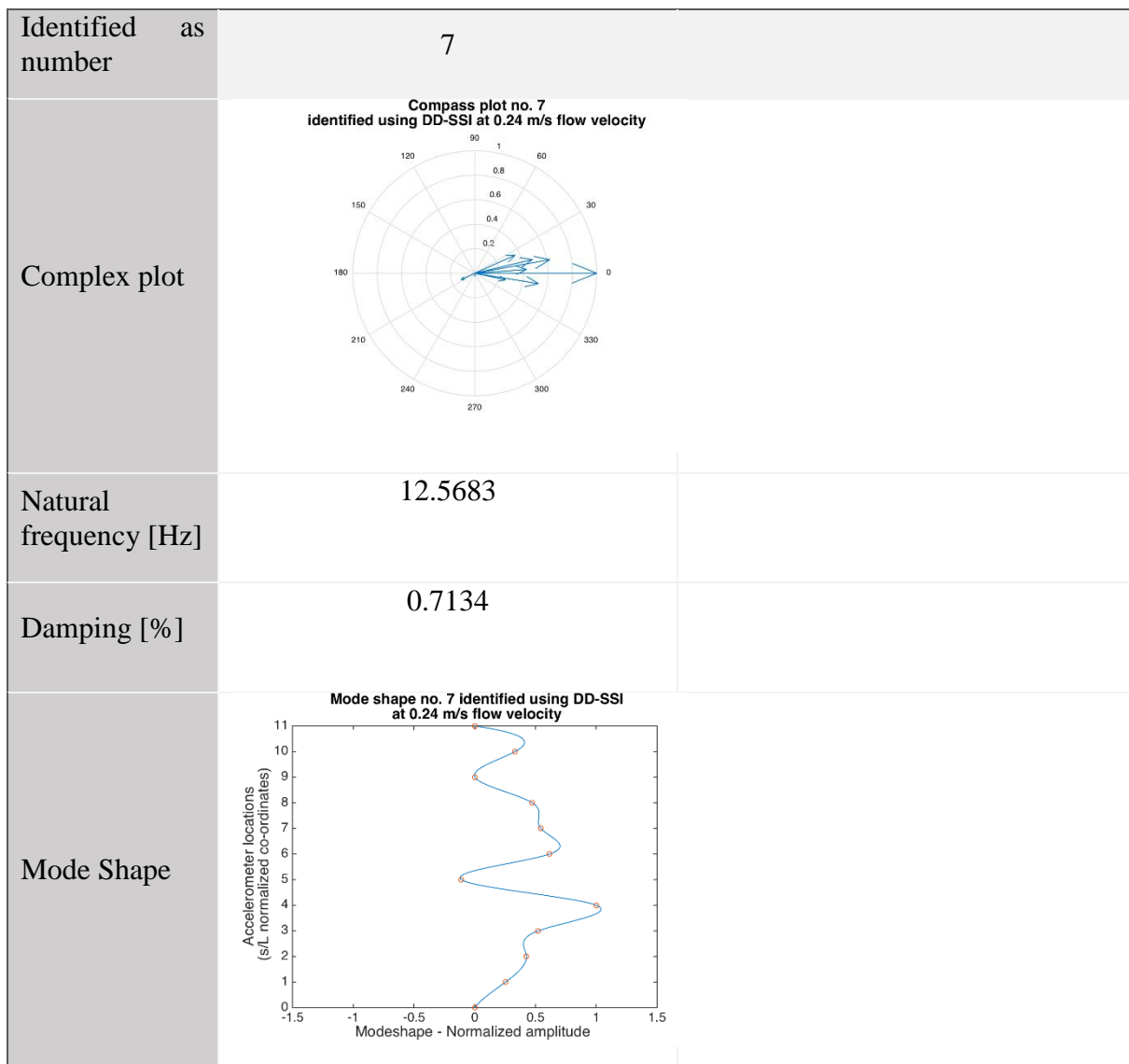
Figure D 4: MAC matrix for DD-SSI method obtained mode shapes, 0.12 m/s current velocity

## D.2.2 0.24 m/s

Table D 5: Results from DD-SSI method, 0.24 m/s flow velocity

| Identified as number   | 1   | 2   |
|------------------------|---|---|
| Complex plot           | <p>Compass plot no. 1 identified using DD-SSI at 0.24 m/s flow velocity</p>    | <p>Compass plot no. 2 identified using DD-SSI at 0.24 m/s flow velocity</p>    |
| Natural frequency [Hz] | 1.1528  | 1.8037  |
| Damping [%]            | 7.9148  | 12.8815   |
| Mode Shape             | <p>Mode shape no. 1 identified using DD-SSI at 0.24 m/s flow velocity</p>    | <p>Mode shape no. 2 identified using DD-SSI at 0.24 m/s flow velocity</p>     |
| Identified as number   | 3   | 4   |
| Complex plot           | <p>Compass plot no. 3 identified using DD-SSI at 0.24 m/s flow velocity</p>  | <p>Compass plot no. 4 identified using DD-SSI at 0.24 m/s flow velocity</p>  |
| Natural frequency [Hz] | 2.8991  | 7.4071  |

|                        |  |  |
|------------------------|--|--|
| Damping [%]            | 0.0401   | 1.3887   |
| Mode Shape             | <p>Mode shape no. 3 identified using DD-SSI at 0.24 m/s flow velocity</p>     | <p>Mode shape no. 4 identified using DD-SSI at 0.24 m/s flow velocity</p>      |
| Identified as number   | 5  | 6  |
| Complex plot           | <p>Compass plot no. 5 identified using DD-SSI at 0.24 m/s flow velocity</p>  | <p>Compass plot no. 6 identified using DD-SSI at 0.24 m/s flow velocity</p>  |
| Natural frequency [Hz] | 8.6981   | 10.3978  |
| Damping [%]            | 0.0194   | 0.5496   |
| Mode Shape             | <p>Mode shape no. 5 identified using DD-SSI at 0.24 m/s flow velocity</p>   | <p>Mode shape no. 6 identified using DD-SSI at 0.24 m/s flow velocity</p>    |



**AutoMAC matrix of the DDSSI 0.24 m/s solutions vs FEM solutions**

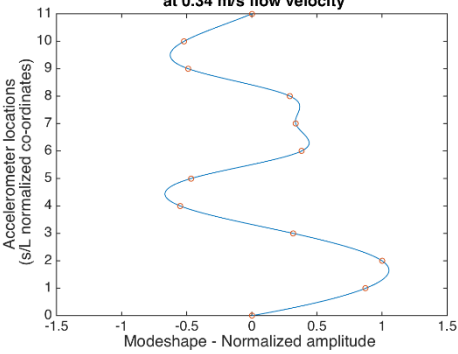
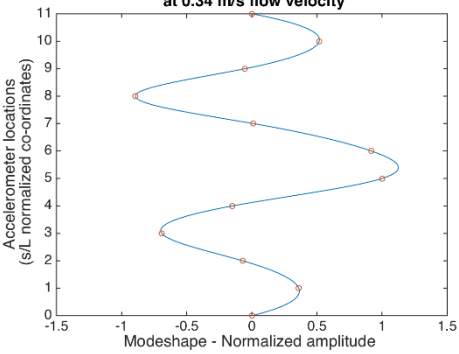
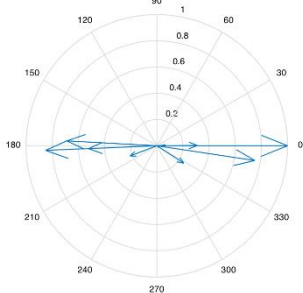
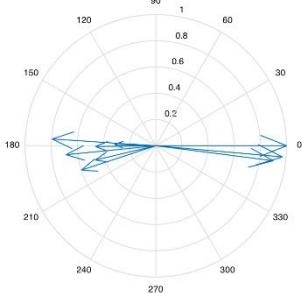
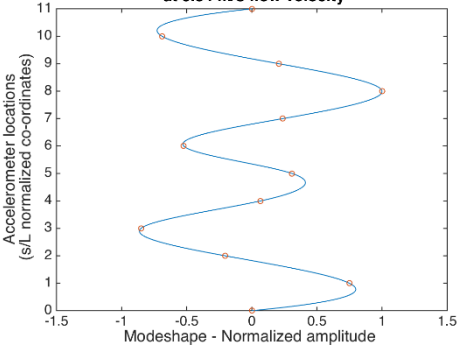
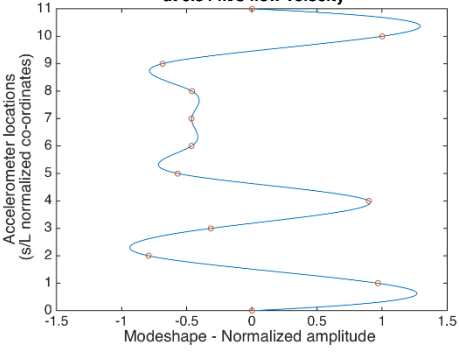
|                      |                  |                  |                  |                  |                  |                  |                  |                  |                  |                   |
|----------------------|------------------|------------------|------------------|------------------|------------------|------------------|------------------|------------------|------------------|-------------------|
| DDSSI24 <sub>1</sub> | 0.08             | 0.00             | 0.89             | 0.02             | 0.01             | 0.00             | 0.00             | 0.00             | 0.00             | 0.01              |
| DDSSI24 <sub>2</sub> | 0.04             | 0.21             | 0.15             | 0.29             | 0.16             | 0.03             | 0.13             | 0.03             | 0.02             | 0.06              |
| DDSSI24 <sub>3</sub> | 0.03             | 0.00             | 0.01             | 0.00             | 0.97             | 0.01             | 0.01             | 0.01             | 0.01             | 0.03              |
| DDSSI24 <sub>4</sub> | 0.00             | 0.00             | 0.00             | 0.02             | 0.00             | 0.02             | 0.01             | 0.95             | 0.03             | 0.04              |
| DDSSI24 <sub>5</sub> | 0.02             | 0.01             | 0.00             | 0.02             | 0.00             | 0.00             | 0.02             | 0.00             | 0.99             | 0.00              |
| DDSSI24 <sub>6</sub> | 0.00             | 0.03             | 0.00             | 0.05             | 0.01             | 0.01             | 0.03             | 0.01             | 0.10             | 0.91              |
| DDSSI24 <sub>7</sub> | 0.64             | 0.06             | 0.03             | 0.02             | 0.01             | 0.00             | 0.05             | 0.02             | 0.00             | 0.34              |
|                      | FEM <sub>1</sub> | FEM <sub>2</sub> | FEM <sub>3</sub> | FEM <sub>4</sub> | FEM <sub>5</sub> | FEM <sub>6</sub> | FEM <sub>7</sub> | FEM <sub>8</sub> | FEM <sub>9</sub> | FEM <sub>10</sub> |

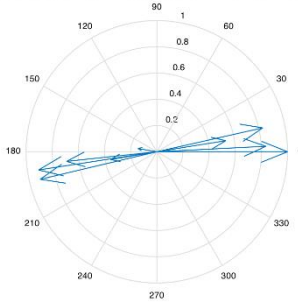
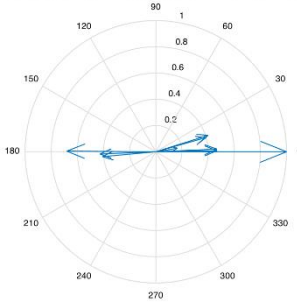
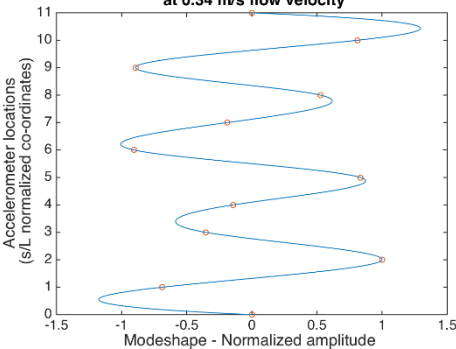
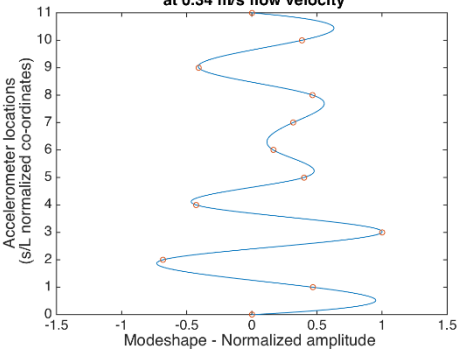
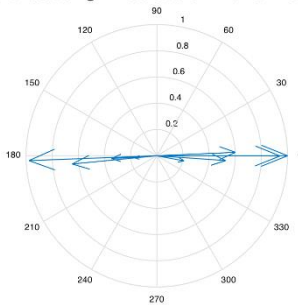
Figure D 5: MAC matrix for DD-SSI method obtained mode shapes, 0.24 m/s current velocity

D.2.3 0.34 m/s

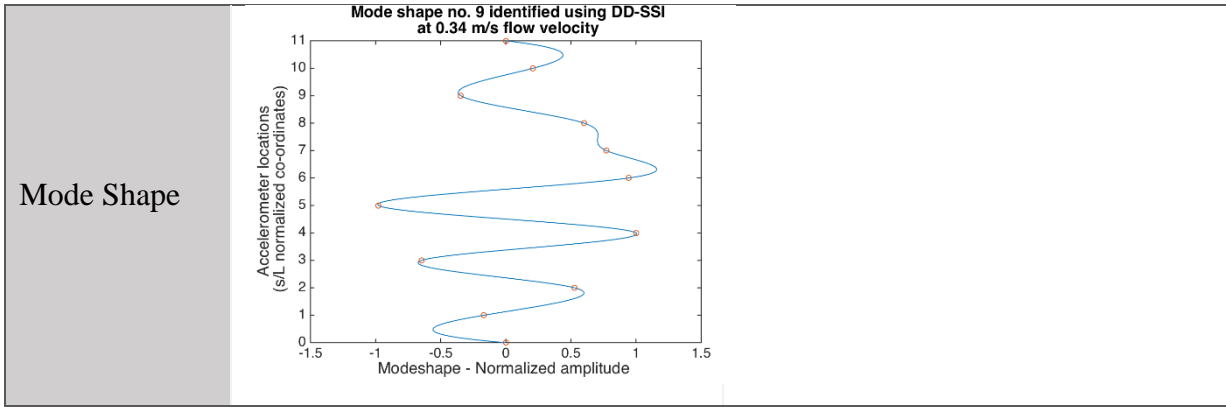
Table D 6: Results from DD-SSI method, 0.34 m/s flow velocity

| Identified as number   | 1   | 2   |
|------------------------|---|---|
| Complex plot           | <p>Compass plot no. 1 identified using DD-SSI at 0.34 m/s flow velocity</p> | <p>Compass plot no. 2 identified using DD-SSI at 0.34 m/s flow velocity</p> |
| Natural frequency [Hz] | 0.8349  | 1.1562  |
| Damping [%]            | 30.5146   | 20.6500   |
| Mode Shape             | <p>Mode shape no. 1 identified using DD-SSI at 0.34 m/s flow velocity</p>   | <p>Mode shape no. 2 identified using DD-SSI at 0.34 m/s flow velocity</p>   |
| Identified as number   | 3   | 4   |
| Complex plot           | <p>Compass plot no. 3 identified using DD-SSI at 0.34 m/s flow velocity</p> | <p>Compass plot no. 4 identified using DD-SSI at 0.34 m/s flow velocity</p> |

|                        |  |  |
|------------------------|--|--|
| Natural frequency [Hz] | 1.9261   | 3.1159   |
| Damping [%]            | 11.9707  | 2.9477   |
| Mode Shape             | <p>Mode shape no. 3 identified using DD-SSI at 0.34 m/s flow velocity</p>     | <p>Mode shape no. 4 identified using DD-SSI at 0.34 m/s flow velocity</p>      |
| Identified as number   | 5  | 6  |
| Complex plot           | <p>Compass plot no. 5 identified using DD-SSI at 0.34 m/s flow velocity</p>  | <p>Compass plot no. 6 identified using DD-SSI at 0.34 m/s flow velocity</p>  |
| Natural frequency [Hz] | 4.4592   | 5.1531   |
| Damping [%]            | 0.4871   | 6.3966   |
| Mode Shape             | <p>Mode shape no. 5 identified using DD-SSI at 0.34 m/s flow velocity</p>   | <p>Mode shape no. 6 identified using DD-SSI at 0.34 m/s flow velocity</p>    |

|                        |   |  |   |  |
|------------------------|---|--|---|--|
| Identified as number   | 7   |  | 8   |  |
| Complex plot           | <p>Compass plot no. 7 identified using DD-SSI at 0.34 m/s flow velocity</p>    |  | <p>Compass plot no. 8 identified using DD-SSI at 0.34 m/s flow velocity</p>  |  |
| Natural frequency [Hz] | 6.6952  |  | 8.9013  |  |
| Damping [%]            | 4.5520  |  | 0.4690  |  |
| Mode Shape             | <p>Mode shape no. 7 identified using DD-SSI at 0.34 m/s flow velocity</p>     |  | <p>Mode shape no. 8 identified using DD-SSI at 0.34 m/s flow velocity</p>    |  |
| Identified as number   | 9   |  |   |  |
| Complex plot           | <p>Compass plot no. 9 identified using DD-SSI at 0.34 m/s flow velocity</p>  |  |   |  |
| Natural frequency [Hz] | 15.1055   |  |   |  |
| Damping [%]            | 0.5761  |  |   |  |





**AutoMAC matrix of the DDSSI 0.34 m/s solutions vs FEM solutions**

|                      |                  |                  |                  |                  |                  |                  |                  |                  |                  |                   |
|----------------------|------------------|------------------|------------------|------------------|------------------|------------------|------------------|------------------|------------------|-------------------|
| DDSSI34 <sub>1</sub> | 0.09             | 0.16             | 0.65             | 0.10             | 0.02             | 0.00             | 0.02             | 0.01             | 0.00             | 0.01              |
| DDSSI34 <sub>2</sub> | 0.13             | 0.51             | 0.23             | 0.05             | 0.02             | 0.03             | 0.05             | 0.01             | 0.02             | 0.07              |
| DDSSI34 <sub>3</sub> | 0.01             | 0.16             | 0.13             | 0.75             | 0.00             | 0.00             | 0.04             | 0.01             | 0.02             | 0.03              |
| DDSSI34 <sub>4</sub> | 0.03             | 0.00             | 0.22             | 0.01             | 0.78             | 0.02             | 0.00             | 0.00             | 0.00             | 0.01              |
| DDSSI34 <sub>5</sub> | 0.00             | 0.08             | 0.02             | 0.05             | 0.00             | 0.89             | 0.00             | 0.00             | 0.00             | 0.00              |
| DDSSI34 <sub>6</sub> | 0.04             | 0.03             | 0.00             | 0.03             | 0.04             | 0.01             | 0.99             | 0.00             | 0.02             | 0.05              |
| DDSSI34 <sub>7</sub> | 0.00             | 0.01             | 0.00             | 0.01             | 0.00             | 0.00             | 0.01             | 0.98             | 0.02             | 0.01              |
| DDSSI34 <sub>8</sub> | 0.07             | 0.00             | 0.00             | 0.00             | 0.00             | 0.01             | 0.02             | 0.02             | 0.90             | 0.05              |
| DDSSI34 <sub>9</sub> | 0.04             | 0.01             | 0.00             | 0.02             | 0.02             | 0.00             | 0.05             | 0.00             | 0.08             | 0.93              |
|                      | FEM <sub>1</sub> | FEM <sub>2</sub> | FEM <sub>3</sub> | FEM <sub>4</sub> | FEM <sub>5</sub> | FEM <sub>6</sub> | FEM <sub>7</sub> | FEM <sub>8</sub> | FEM <sub>9</sub> | FEM <sub>10</sub> |

Figure D 6: MAC matrix for DD-SSI method obtained mode shapes, 0.34 m/s current velocity

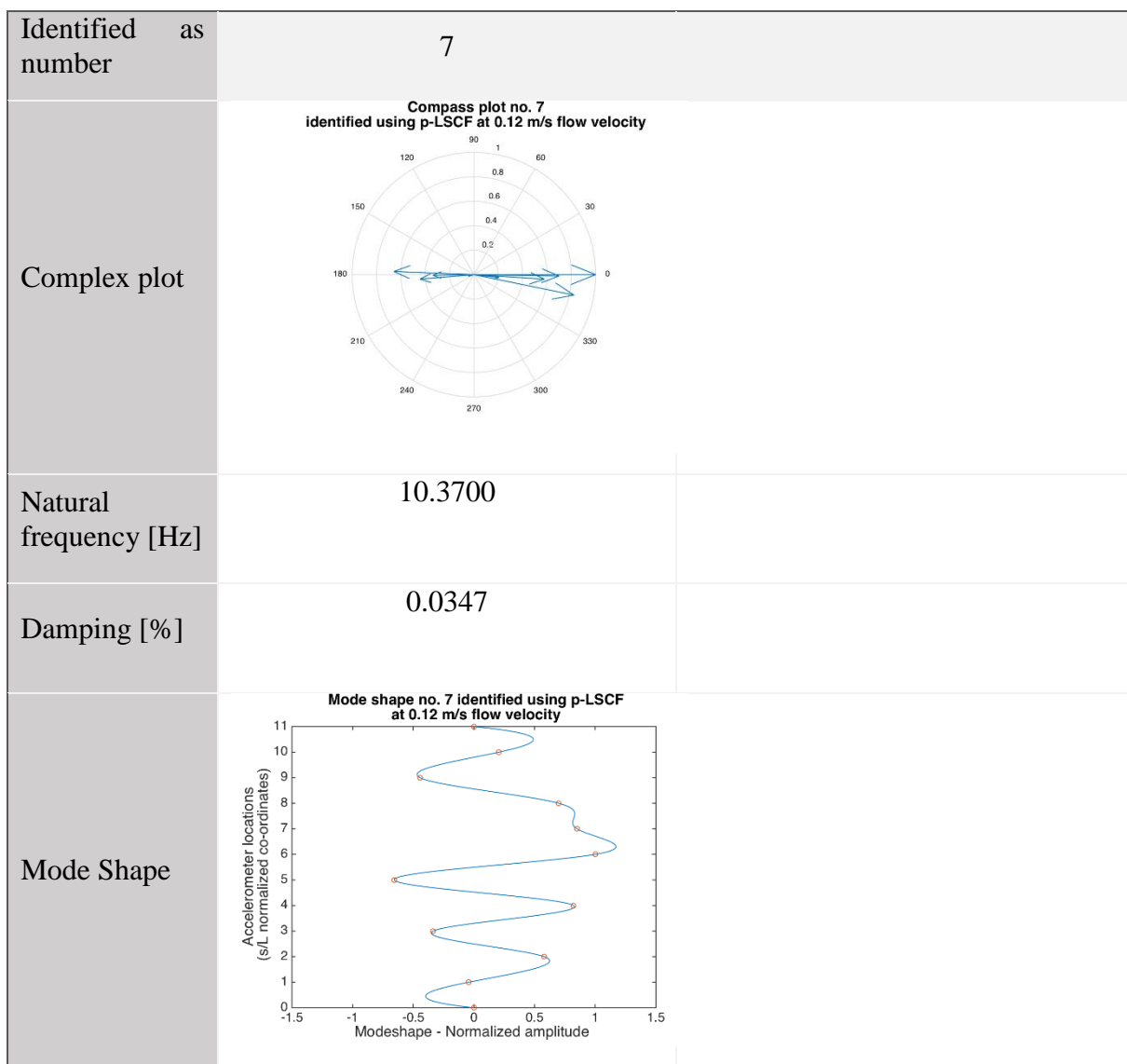
## D.3 p-LSCF

### D.3.1 0.12 m/s

Table D 7: Results from p-LSCF method, 0.12 m/s flow velocity

| Identified as number   | 1   | 2   |
|------------------------|---|---|
| Complex plot           | <p>Compass plot no. 1 identified using p-LSCF at 0.12 m/s flow velocity</p> | <p>Compass plot no. 2 identified using p-LSCF at 0.12 m/s flow velocity</p> |
| Natural frequency [Hz] | 1.2084  | 1.7484  |
| Damping [%]            | 2.0556  | 7.4206  |
| Mode Shape             | <p>Mode shape no. 1 identified using p-LSCF at 0.12 m/s flow velocity</p>   | <p>Mode shape no. 2 identified using p-LSCF at 0.12 m/s flow velocity</p>   |
| Identified as number   | 3   | 4   |
| Complex plot           | <p>Compass plot no. 3 identified using p-LSCF at 0.12 m/s flow velocity</p> | <p>Compass plot no. 4 identified using p-LSCF at 0.12 m/s flow velocity</p> |

|                        |   |   |
|------------------------|---|---|
| Natural frequency [Hz] | 3.4736  | 5.1882  |
| Damping [%]            | 0.0321  | 0.1161  |
| Mode Shape             | <p>Mode shape no. 3 identified using p-LSCF at 0.12 m/s flow velocity</p>   | <p>Mode shape no. 4 identified using p-LSCF at 0.12 m/s flow velocity</p>   |
| Identified as number   | 5   | 6   |
| Complex plot           | <p>Compass plot no. 5 identified using p-LSCF at 0.12 m/s flow velocity</p> | <p>Compass plot no. 6 identified using p-LSCF at 0.12 m/s flow velocity</p> |
| Natural frequency [Hz] | 6.6276  | 6.9341  |
| Damping [%]            | 0.0579  | 0.0205  |
| Mode Shape             | <p>Mode shape no. 5 identified using p-LSCF at 0.12 m/s flow velocity</p>   | <p>Mode shape no. 6 identified using p-LSCF at 0.12 m/s flow velocity</p>   |



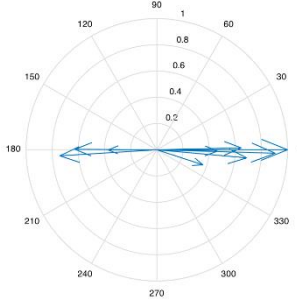
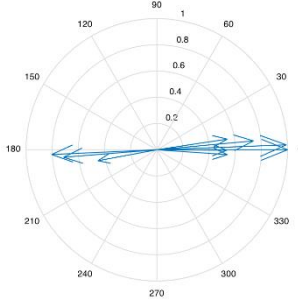
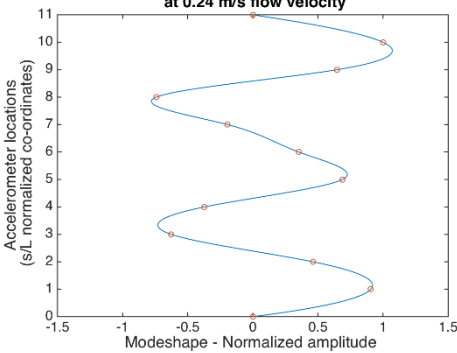
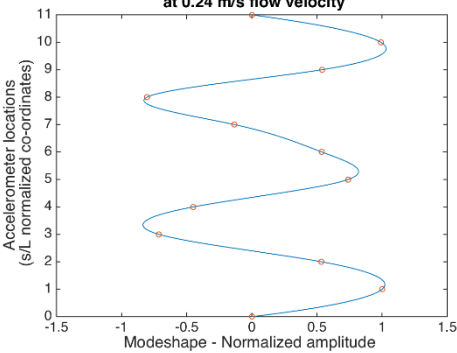
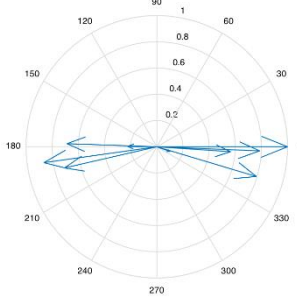
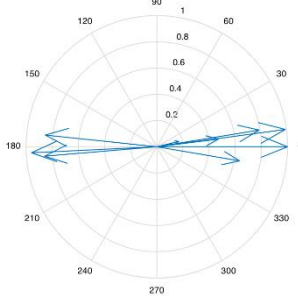
**AutoMAC matrix of the pLSCF 0.12 m/s solutions vs FEM solutions**

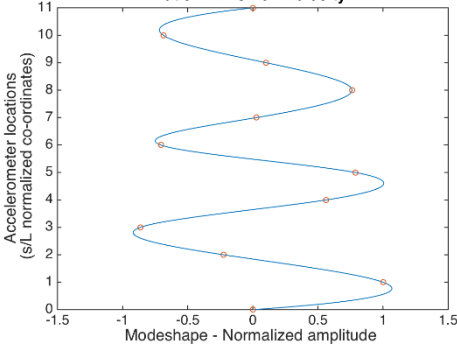
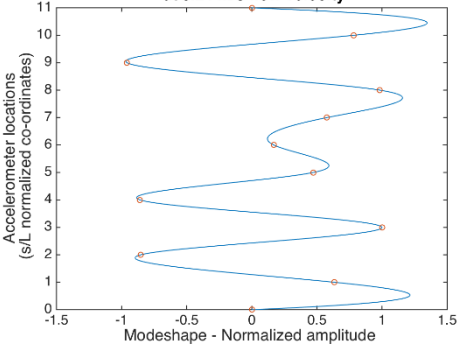
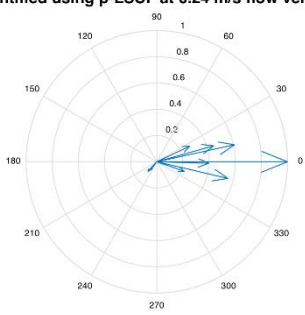
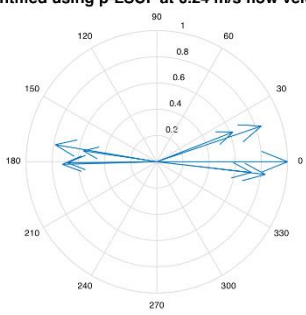
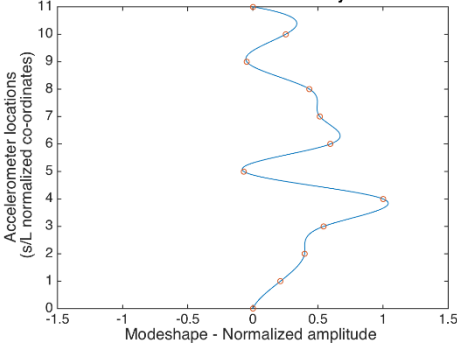
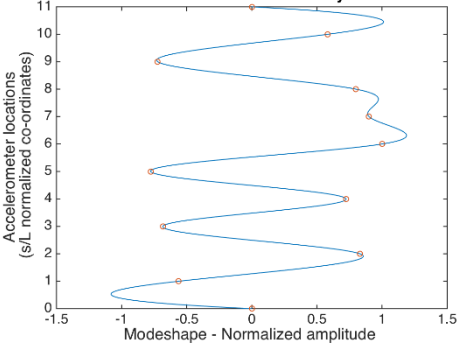


Figure D 7: MAC matrix for p-LSCF method obtained mode shapes, 0.12 m/s current velocity

D.3.2 0.24 m/s

Table D 8: Results from p-LSCF method, 0.24 m/s flow velocity

| Identified as number   | 1   | 2   |
|------------------------|---|---|
| Complex plot           | <p>Compass plot no. 1 identified using p-LSCF at 0.24 m/s flow velocity</p>    | <p>Compass plot no. 2 identified using p-LSCF at 0.24 m/s flow velocity</p>    |
| Natural frequency [Hz] | 1.1171  | 2.8941  |
| Damping [%]            | 2.9492  | 0.0632  |
| Mode Shape             | <p>Mode shape no. 1 identified using p-LSCF at 0.24 m/s flow velocity</p>    | <p>Mode shape no. 2 identified using p-LSCF at 0.24 m/s flow velocity</p>     |
| Identified as number   | 3   | 4   |
| Complex plot           | <p>Compass plot no. 3 identified using p-LSCF at 0.24 m/s flow velocity</p>  | <p>Compass plot no. 4 identified using p-LSCF at 0.24 m/s flow velocity</p>  |
| Natural frequency [Hz] | 4.0697  | 8.6850  |

|                        |  |  |
|------------------------|--|--|
| Damping [%]            | 0.0888   | 0.0060   |
| Mode Shape             | <p>Mode shape no. 3 identified using p-LSCF at 0.24 m/s flow velocity</p>     | <p>Mode shape no. 4 identified using p-LSCF at 0.24 m/s flow velocity</p>      |
| Identified as number   | 5  | 6  |
| Complex plot           | <p>Compass plot no. 5 identified using p-LSCF at 0.24 m/s flow velocity</p>  | <p>Compass plot no. 6 identified using p-LSCF at 0.24 m/s flow velocity</p>  |
| Natural frequency [Hz] | 12.6917  | 13.5157  |
| Damping [%]            | 0.0052   | 0.0267   |
| Mode Shape             | <p>Mode shape no. 5 identified using p-LSCF at 0.24 m/s flow velocity</p>   | <p>Mode shape no. 6 identified using p-LSCF at 0.24 m/s flow velocity</p>    |

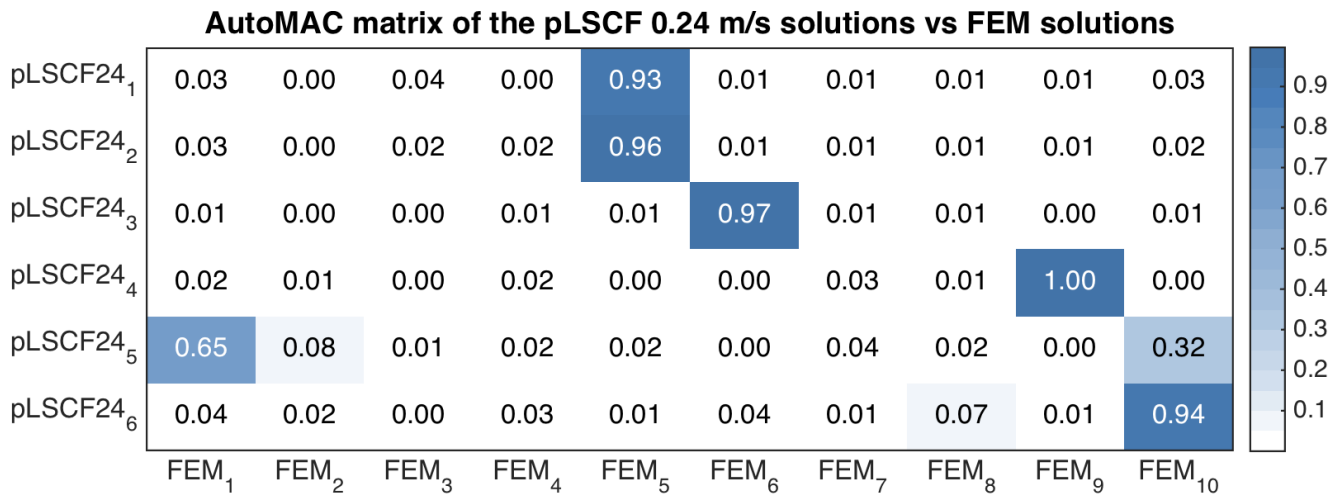


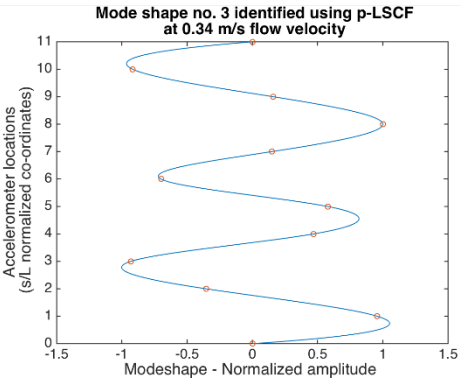
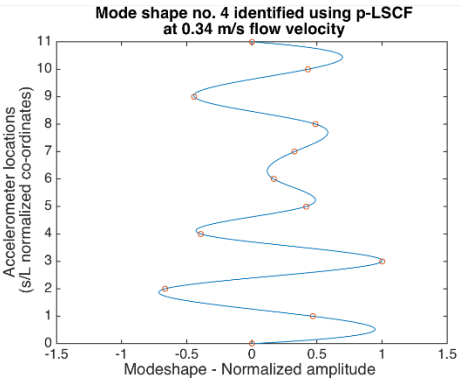
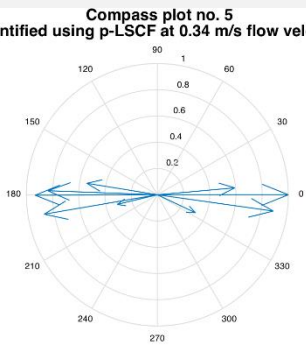
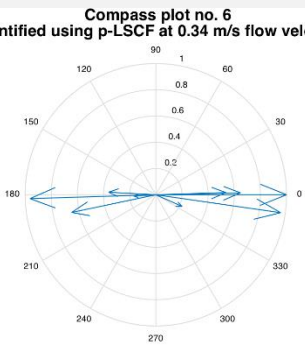
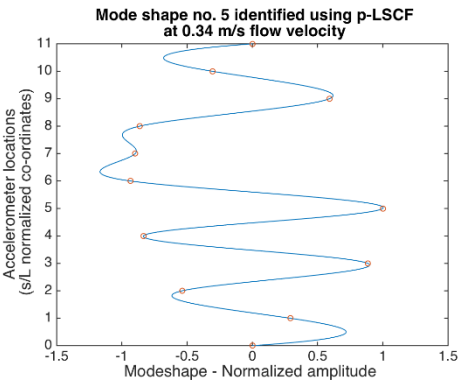
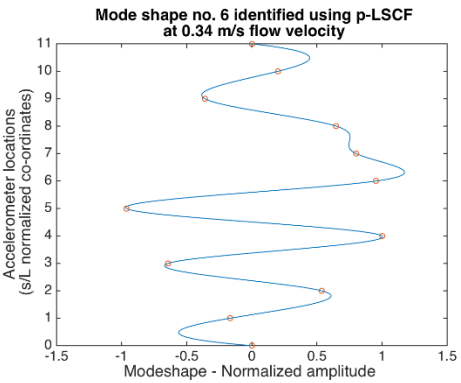
*Figure D 8: MAC matrix for p-LSCF method obtained mode shapes, 0.24 m/s current velocity*

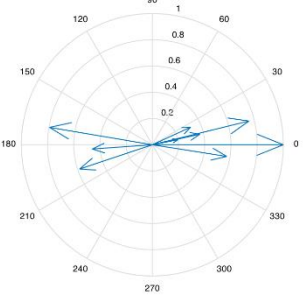
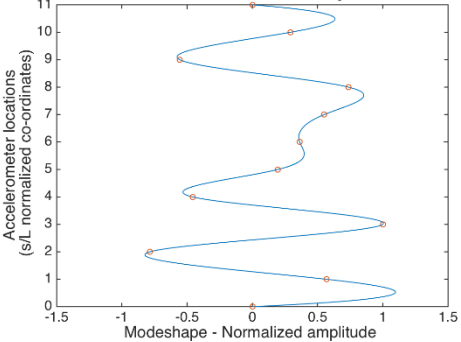
### D.3.3 0.34 m/s

Table D 9: Results from p-LSCF method, 0.34m/s flow velocity

| Identified as number   | 1   | 2   |
|------------------------|---|---|
| Complex plot           | <p>Compass plot no. 1 identified using p-LSCF at 0.34 m/s flow velocity</p> | <p>Compass plot no. 2 identified using p-LSCF at 0.34 m/s flow velocity</p> |
| Natural frequency [Hz] | 1.8320  | 3.1513  |
| Damping [%]            | 0.2701  | 1.3963  |
| Mode Shape             | <p>Mode shape no. 1 identified using p-LSCF at 0.34 m/s flow velocity</p>   | <p>Mode shape no. 2 identified using p-LSCF at 0.34 m/s flow velocity</p>   |
| Identified as number   | 3   | 4   |
| Complex plot           | <p>Compass plot no. 3 identified using p-LSCF at 0.34 m/s flow velocity</p> | <p>Compass plot no. 4 identified using p-LSCF at 0.34 m/s flow velocity</p> |
| Natural frequency [Hz] | 4.2759  | 8.9200  |



|                        |  |  |
|------------------------|--|--|
| Damping [%]            | 2.3362   | 0.1812   |
| Mode Shape             | <p>Mode shape no. 3 identified using p-LSCF at 0.34 m/s flow velocity</p>     | <p>Mode shape no. 4 identified using p-LSCF at 0.34 m/s flow velocity</p>      |
| Identified as number   | 5  | 6  |
| Complex plot           | <p>Compass plot no. 5 identified using p-LSCF at 0.34 m/s flow velocity</p>  | <p>Compass plot no. 6 identified using p-LSCF at 0.34 m/s flow velocity</p>  |
| Natural frequency [Hz] | 10.6715  | 15.1649  |
| Damping [%]            | 0.1668   | 0.2441   |
| Mode Shape             | <p>Mode shape no. 5 identified using p-LSCF at 0.34 m/s flow velocity</p>   | <p>Mode shape no. 6 identified using p-LSCF at 0.34 m/s flow velocity</p>    |

|                        |  |  |
|------------------------|--|--|
| Identified as number   | 7  |  |
| Complex plot           | <p style="text-align: center;"><b>Compass plot no. 7</b><br/>identified using p-LSCF at 0.34 m/s flow velocity</p>  |  |
| Natural frequency [Hz] | 17.4058  |  |
| Damping [%]            | 0.0777   |  |
| Mode Shape             | <p style="text-align: center;"><b>Mode shape no. 7 identified using p-LSCF</b><br/>at 0.34 m/s flow velocity</p>   |  |

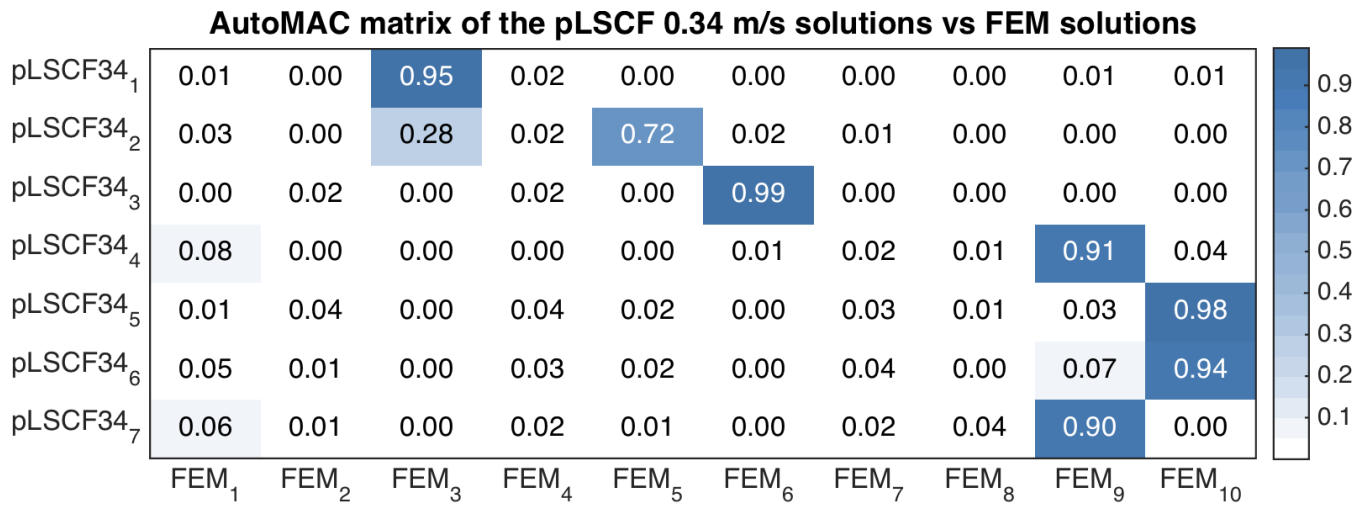


Figure D 9: MAC matrix for p-LSCF method obtained mode shapes, 0.34 m/s current velocity



---

# Appendix E

## List of Matlab Scripts

The following codes are included in the zip-folder submitted with this thesis.

For TDD analysis:

- TDD\_method.m: The program used for identifying modes, plotting mode shapes and calculating MAC matrices.
- MAC\_func.m: Calculates the MAC value of two vectors of same length.
- MZerocross.m: Calculates the damped period of the participation time series.
- TDD\_fnat\_damp.m: Calculates the natural frequencies and mode shapes.

For importing and viewing static configuration obtained from RIFLEX:

- Static\_Analysis\_Beam\_Mass.m: Imports RIFLEX files and gives an output .mat file containing static analysis results used for modal analysis.
- get\_matrix.m: Transforms mpf file data to matrices.

For numerical investigations of the accelerometer effects on the solution of the eigenvalue problem:

- SCR\_Eigenvalues.m: Used to select mass case to be investigated, number of modes to calculate and which mode shape to plot. Gives a .mat file containing identified natural frequencies and mode shapes at the accelerometer locations as output. Output is used for calculation of MAC values and frequency deviations.
- SCR\_Beam\_FEM\_Fun.m: Creates global mass and stiffness matrices, calculates natural frequencies and mode shapes, sorts the calculated modes and outputs the requested number of modes and modeshapes.
- feaplycs.m: Applies boundary conditions to the global mass and stiffness matrices.
- feasmb11.m: Assembles local element mass and stiffness matrices into global mass and stiffness matrices according to indexing.
- feeldof1.m: Creates indexes for the DOFs associated with each local element mass and stiffness matrix for use when assembling global matrices.

- 
- `feframe2.m`: Creates local element mass and stiffness matrices for elements without accelerometer masses.
  - `feframe3.m`: Creates local element mass and stiffness matrices for elements with lumped mass at the second node.
  - `feframe4.m`: Creates local element mass and stiffness matrices for elements with lumped mass at the first node.